UNIVERSIDAD NACIONAL AUTÓNOMA DE MÉXICO
PROGRAMA DE MAESTRÍA Y DOCTORADO EN INGENIERÍA
INGENIERÍA MECÁNICA – TERMOFLUIDOS

ANALYSIS OF MOMENTUM TRANSFER AND MASS IN AN AERATED STIRRED
TANK THROUGH A FLUID MECHANICS STUDY

TESIS
QUE PARA OPTAR POR EL GRADO DE:
DOCTOR EN INGENIERÍA

PRESENTA:
DAVID ISRAEL POSADAS NAVARRO

TUTOR PRINCIPAL
DR. GABRIEL ASCANIO GASCA
INSTITUTO DE CIENCIAS APLICADAS Y TECNOLOGÍA-UNAM

COTUTOR
DR. MARTÍN SALINAS VÁZQUEZ
INSTITUTO DE INGENIERÍA-UNAM

COMITÉ TUTOR
DR. FEDERICO MÉNDEZ LAVIELLE
FACULTAD DE INGENIERÍA-UNAM

CIUDAD UNIVERSITARIA, CD. MX., JULIO 2022

JURADO ASIGNADO:

Presidente: Dr. Méndez Lavielle Federico, Facultad de Ingeniería

Secretario: Dr. Solorio Ordaz Francisco Javier, Facultad de Ingeniería

1er. Vocal: Dr. Ascanio Gasca Gabriel, ICAT

2do. Vocal: Dr. Salinas Vázquez Martín, Instituto de Ingeniería

3er. Vocal: Dr. Trujillo Roldán Mauricio Alberto, Instituto de Invest. Biomédicas
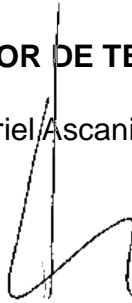
Lugares donde se realizó la tesis:

Instituto de Ciencias Aplicadas y Tecnología, UNAM

Instituto de Ingeniería, UNAM

Instituto de Investigaciones Biomédicas, UNAM

TUTOR DE TESIS:

Dr. Gabriel Ascanio Gasca

FIRMA

COTUTOR DE TESIS:

Dr. Martín Salinas Vázquez

FIRMA

Contents

List of Figures

List of Tables

Nomenclature

Symbols used

C_1: distance between the sparger and the lower impeller (m)

C_2: distance between the lower impeller and the mid impeller (m)

C_3: distance between the mid impeller and the upper impeller (m)

C_4: distance between upper impeller and the free surface (m)

C_l: oxygen concentration as a function of time $(\%)$

C^*: saturation oxygen concentration in the liquid phase $(\%)$

D_I: impeller diameter (m)

d_p: tracer particle diameter (m)

Fl_g: gas flow number $(-)$

H: liquid height (m)

H_g: liquid height after aeration (m)

H_0: liquid height before aeration (m)

h_s: position of the sparger from the tank bottom (m)

J: baffle width (m)

K_p: power constant $(-)$

$k_L a$: volumetric mass transfer coefficient $(1/h)$

M_e: effective torque $(N \cdot m)$

M_d: torque with fluid $(N \cdot m)$

M_f: torque with the empty tank $(N \cdot m)$

N: rotational speed $(1/s)$

N_{pg}: gassed power number $(-)$

N_q: pumping number $(-)$

P: ungassed power (W)

P_g: gassed power (W)

$\dot{Q}$: volumetric gas flow rate (l/m)

Q_T: total pumping (m^3/s)

Q_x: horizontal pumping (m^3/s)

Q_y: vertical pumping (m^3/s)

RS: Reynolds stress (m^2/s^2)

R_e: Reynolds number $(-)$

$|\bar{S}|$: modulus strain rate tensor $(1/s)$

t: time (s)

T: tank diameter (s)

u: horizontal velocity (m/s)

$u^{'}$: fluid velocity fluctuation in the horizontal direction (m/s)

v: vertical velocity (m/s)

$v^{'}$: fluid velocity fluctuation in the vertical direction (m/s)

V_o: operating volume (m^3)

v_p: tracer particle velocity (m/s)

V_{tip}: impeller tip velocity (m/s)

V_T: total volume (m^3)

$|V^*|$: velocity magnitude normalized $(-)$

X^*: dimensionless horizontal position $(-)$

Y^*: dimensionless vertical position $(-)$

Greek Letters

ε_g: gas hold-up $(-)$

μ: dynamic viscosity $(mPa \cdot s)$

ρ: fluid density (kg/m^3)

ρ_p: tracer particle density (kg/m^3)

τ: response time of tracer particles $(1/s)$

ω_z: vorticity $(1/s)$

Acronyms

ARI: axial-radial impeller

$ARIs$: axial-radial impeller sets

ERT: electrical resistance tomography

PBT: pitched blade turbine

$PBTs$: pitched blade turbine sets

PIV: particle image velocimetry

RT: Rushton turbine

RTs: Rushton turbine sets

TI: turbulent intensity $(-)$

vvm: volume of gas per volume of liquid per minute $(1/min)$

Abstract

This work deals with an experimental study on stirred vessel equipped with multiple impellers providing different discharge flows, namely: radial, axial, and mixed, under ungassed and gassed conditions. A fluid mechanics study has been performed to obtain the local parameters in terms of the flow patterns, velocity magnitude, vorticity, vertical velocity, turbulent intensity, strain rates, and Reynolds stresses. For that purpose, the flow inside the vessel was visualized by means of the 2-D Particle Image Velocimetry Technique (2-D PIV). Local parameters were linked to the common global parameters reported for stirred tanks such as power consumption, mass transfer, and the overall gas hold-up.

Impellers providing radial flow exhibited the mass transfer characteristics at the lowest power drawn when gassing at high flow rates. However, at low gassing flow rates, the best performance was obtained with mixed-flow impellers (hybrid impellers). The combination of tilted and straight blades led to a better distribution of the flow throughout the tank. Moreover, the performance of such impellers should be even better as the fluid viscosity increases, contrary to the radial discharge flow impellers, which tend to create isolated regions.

In particular, the design of hybrid impellers could be improved by modifying its geometry varying the number of blades, their dimensions, etc. Such modifications could lead to better mass transfer characteristics and gas hold-up without consuming more energy.

Chapter 1

Introduction

1.1 Mixing

Mixing in an unit operation aimed to reduce the inhomogeneity of a material to achieve a desired result. Such an inhomogeneity can be expressed mainly in terms of concentration, phase or temperature. On the other hand, secondary effects, such as mass transfer, reaction, and product properties are usually the critical objectives. The mixing is carried out in many industries such as pharmaceutical, petrochemical, mineral processing, chemical, polymer processing, food, etc. The mixing processes are generally divided into six basic operations:

- Mixing of miscible liquids

- Mixed solid-liquid

- Mixed gas-liquid

- Mixing of immiscible liquids

- Mixed with chemical reactions

- Mixed solid-solid

At industrial level, some of the most common equipment for mixing are mechanically stirred tanks. Due to the different processes and objectives required for each of the mentioned industries, a wide variety of designs of these types of equipment have been developed. Mechanically stirred tanks are the most widely used due to their great flexibility and robustness. For this reason, there is a large number of works reported in the literature in which the mixing process is carried out through these devices. Due to the

above, it is important to generate the necessary tools to be able to obtain local and global parameters that help to increase the quality of the mixed product and reduce operating costs in this type of equipment.

1.2   Mechanically stirred tank

Although, nowadays there are many devices to perform a mixing process one of the most used devices in the last years (Fitschen et al. (2021), Forte et al. (2021b), Maluta et al. (2020), Zhu et al. (2021)) are the mechanically stirred tanks. The mixing with mechanical mixers occurs under either laminar or turbulent flow conditions, depending on the impeller Reynolds number ($Re = \rho N D_I^2/\mu$). In general, for Reynolds numbers below about 100 (Lamberto et al. (1999)), the process is laminar, also called creeping flow. Fully turbulent conditions are achieved at Reynolds numbers higher than about 10^4 (Placek and Tavlarides (1985)), and the flow is considered transitional between these two regimes.

The mixing in mechanically stirred tanks has a variety of objectives, including homogenizing single or multiple phases in terms of concentration of components, physical properties, temperature, and biological properties. Over 50% of the world's chemical production involves these stirred tanks for manufacturing high-added-value products. These tanks are commonly used for:

- Blending of homogeneous liquids such as lube oils, gasoline additives, dilution, and a variety of chemicals

- Dispersing gas in liquid for absorption, stripping, oxidation, hydrogenation, ozonation, chlorination, fermentation, etc.

- Homogenizing viscous complex liquids for polymer blending, paints, solution polymerization, food products, etc.

- Blending and emulsification of liquids for hydrolysis/neutralization reactions, extraction, suspension polymerization, cosmetics, food products, etc.

The basic design of a stirred tank is shown in figure 1.1. In this types of equipments, an agitator or impeller is mounted on a shaft, which is driven by means of a motor coupled to a gearbox with the aim of increasing the output torque. The above is placed inside a tank where the components are poured to be mixed. Commonly, the tank consists of a vertical cylindrical with a circular cross-section, which has an ellipsoidal or torispherical

bottom in order to make a more efficient mixing process. The rotation movement produces the pumping of the fluid throughout the tank, so it is sought to increase its mechanical energy to accelerate the processes of mass, momentum, and energy transfer. When the ratio between the height of liquid (H) and the internal diameter of the tank (T) is taller than 1.2 ($H/T > 1.2$) additional impellers are required for that the quality of the product not to be affected. Although the type and number of impellers must be selected according to the mixing process that is carried out.

The stirred tanks are commonly used when it is necessary to maintain a constant composition (Paul et al. (2003)). For that purpose, having a fully turbulent flow inside of the tank is recommended due to that the velocity fluctuations are so intense that inertial forces overwhelm viscous forces, which provokes major homogenous (Bałdyga and Bourne (1999)). Figure 1.1 shows a standard stirred tank used for carrying out mixing in a turbulent regime. In this type of configuration, the impellers have a size (D_I) much smaller than the diameter of the tank (T). On the other hand, is common the use of flow deflecting (baffles), which are placed on the periphery. These devices are relevant to prevent the liquid surface from deforming (Ramírez-Cruz et al. (2020)) and besides the baffles help to promote turbulence inside the tank.
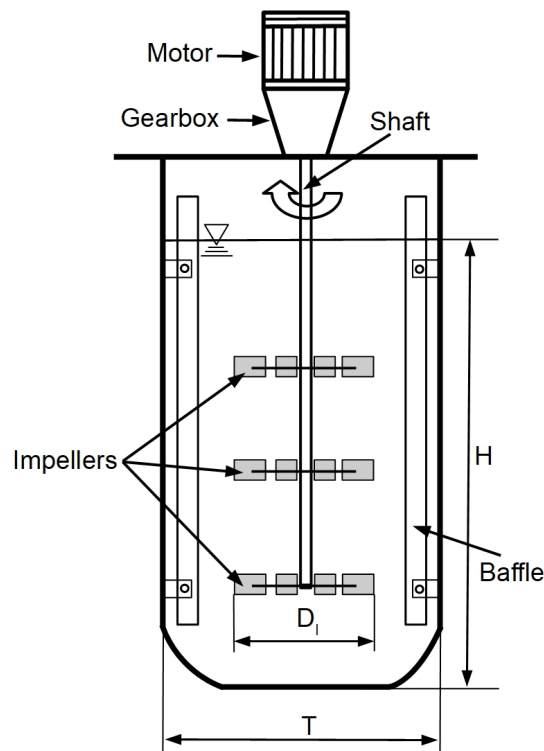
Figure 1.1. Standard stirred tank.

1.3   Impeller types

A large number of impeller designs exists at the industrial and laboratory level (Paul et al. (2003)). A classification of the impellers is based on the viscosity of the fluid to be mixed. If the fluid has a medium to low viscosity, the main classification of impellers is due to the dominant flow pattern, so we have impellers in either the axial or radial type. Flow patterns generated by a radial flow and axial flow impeller is depicted in figure 1.2. In radial type impellers (figure 1.2 (a)), the flow is discharged from the shaft towards the tank walls; this type of impeller is characterized by the formation of a recirculation above the impeller and another below. Most of the mixing usually takes place between these two recirculations, because the impeller discharge zone provides a high level of turbulence and shear in the fluid. This makes them effective in gas-liquid dispersion processes.

Figure 1.2 (b) shows a typical axial flow impeller. These impellers create a flow parallel to the axis of the impeller, forming a single recirculation throughout the entire tank. The impellers push the liquid from the top to the bottom of the tank or viceversa, being effect known as pumping. Thrust can increase or decrease depending on the geometry of the impeller, for example by changing the angle of the blades, the more common is 45°. These impellers are often used in heat transfer processes and for suspension or the addition of solids.
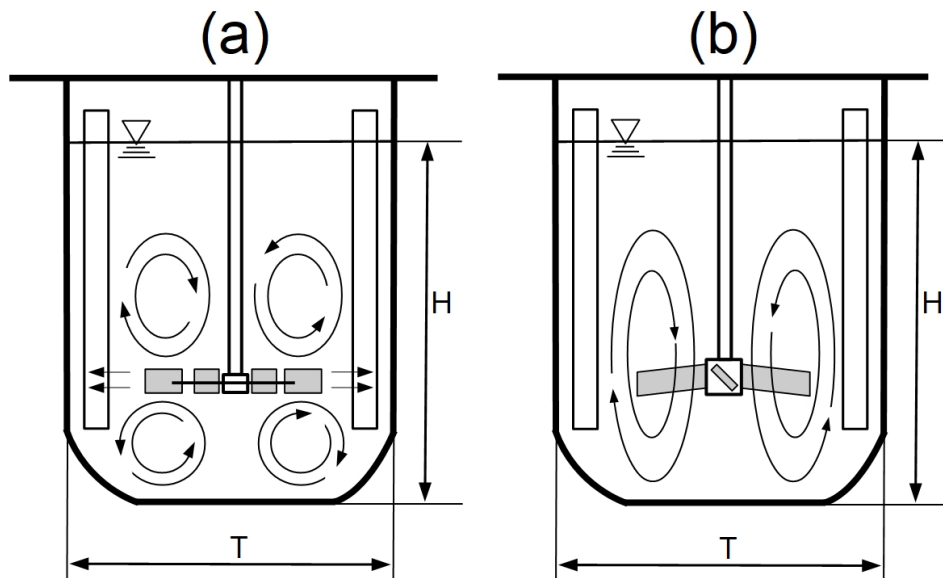
Figure 1.2. Flow patterns created by two types of impellers: (a) radial flow pattern; (b) axial flow pattern.

The impellers used to carry out the mixing under turbulent flow have a much smaller diameter than the tank and are known as open-clearance impellers. When using open-clearance impellers, the more common relationships that can be found going from $D_I/T = 1/3$ to $D_I/T = 1/4$ (Paul et al. (2003), Afshar Ghotli et al. (2020)). The relations smaller ones are used at high rotational speeds and in gas dispersion operations. For liquids with high viscosities, mixing throughout the tank is carried out by means of large-size impellers (their diameter is usually very close to that of the tank) and are known as close-clearance impellers. These types of impellers work at relatively low rotational speeds, however, they provide high power per unit volume. Some examples of these impellers are anchors, helical ribbons, and planetary mixers. Figure 1.3 shows some of the impellers more used at the industry level and table 1.1 summarizes their classification.
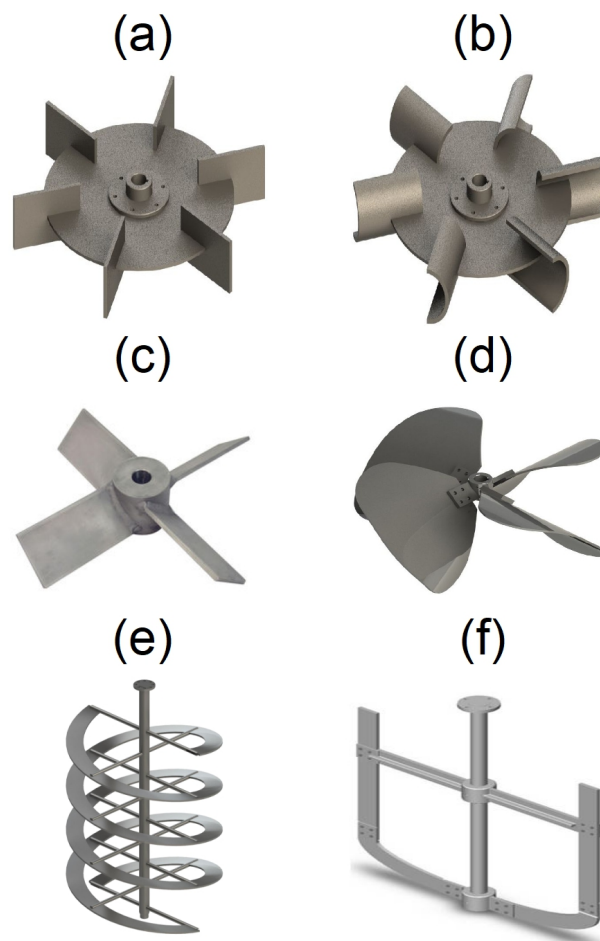
Figure 1.3. Impellers used at the industry level: (a) Rushton turbine; (b) scaba impeller; (c) pitched blade turbine; (d) maxflo impeller; (e) helical ribbon impeller; (f) anchor impeller.

1.4 Gas dispersion in stirred tanks

The dispersion of gas inside stirred tanks has its greatest application in biological applications, such as cultures of bacteria (fermentation process) and the mechanically stirred tanks are one of the most frequently used reactors in such processes.

In fermentation processes, the supply and dispersion of oxygen are key factors. Because oxygen has very low solubility in the biological model (cultive broth), it must be continuously supplied and dispersed as uniformly as possible within the stirred tank. In most cases, oxygen (usually air is used instead) is supplied through a sparger placed below the impeller. On the other hand, in the case of multiple impellers, the sparger is located below the lowest one as is depicted in figure 1.4. Nowadays, there are many configurations of spargers, but in recent years the ring sparger configuration has been the most used for the air supply in gas-liquid applications (Ganguly et al. (2021), Karthikeyan et al. (2022), Li and Chen (2022)) regardless of the type of prevailing flow pattern. The standard ring sparger has small holes on its periphery where the air is supplied to the tank. While the bubbles ascend towards the free surface by the liquid phase due to flotation these are fractionated into small bubbles due to contact of them with impellers' blades. The small bubbles are trapped in the flow pattern created by the impeller with the purpose that these stay as long as possible in the liquid phase and so increase the mass transfer of the process. To provide the maximum gas contact time, it is recommended that the diameter of the ring sparger be ($D_s = 0.8D_I$) 0.8 times the diameter of the impeller.

Finally, when aerated stirred tanks are used three main flow patterns can be distinguished as is depicted in figure 1.5. For an impeller angular velocity N lower than a critical value, (usually labeled as N_f), the gas phase flows up the middle whereas the liquid phase flows up the walls. If the stirred tank operates under such conditions, the impeller is flooded (figure 1.5 (a)). By increasing the impeller angular velocity, the gas phase flows over the entire cross-section above the impeller, and the impeller is loaded (figure 1.5 (b)). If the impeller angular velocity is increased still further, a two-phase dispersion is present above and below the impeller (figure 1.5 (c)). To have better performance in processes involving gas-liquid systems, always the complete dispersion of the bubbles must be reached through the tank.

Table 1.1. Classification of impellers according to the working viscosity fluid.

Turbulent regime (low and mid viscosity)		Laminar regime (high viscosity)
Radial flow	Axial flow	
Rushton turbine	Pitched blade turbine	Helical ribbon impeller
Scaba impeller	Maxflo impeller	Anchor impeller
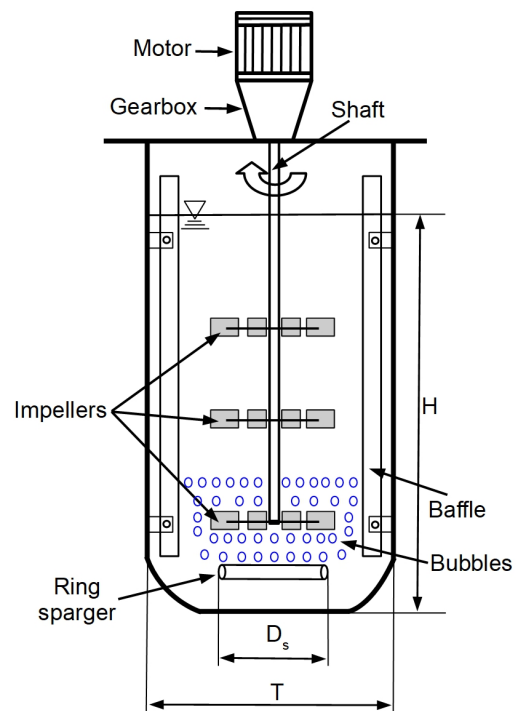
Figure 1.4. Configuration of an aerated stirred tank.
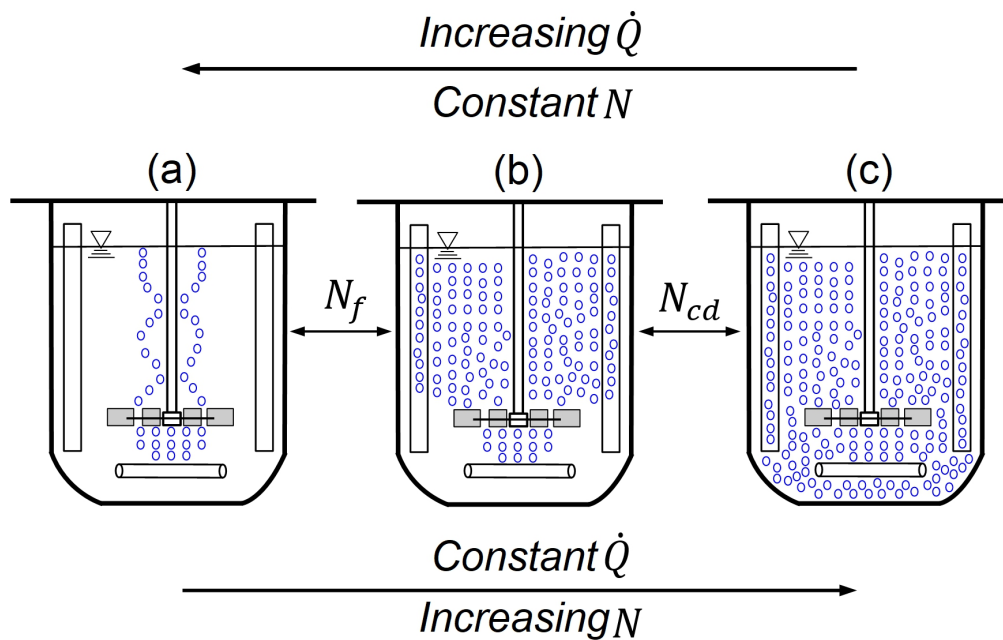
Figure 1.5. Conditions of flow in aerated stirred tanks: (a) flooded; (b) loaded; (c) completely dispersed.

1.5 Characteristic curves

Power consumption can be interpreted as the capacity of the impellers to transfer energy toward fluid. The impellers used in stirred tanks under ungassed conditions are characterized by a classic graph known as the power curve as is depicted in figure 1.6. In this curve, the Reynolds number (Re) against power number ($N_p = P/\rho N^3 D_I^5$) are graphed. The power number is a measurement of dimensionless energy consumption. Although, the Reynolds number can provide the regime in which a process is taking place, it is recommended to obtain the power curve. In this sense, the power curve provides a regime exactly. Due to the above, in this curve, three different behaviors or flow regimes can be observed, which are a function of the Reynolds number. When an impeller is operating under laminar flow conditions, the power number is inversely proportional to the Reynolds number ($N_p \propto R_e^{-1}$). Therefore, in the laminar region, the product of the Reynolds number and the power number is equal to a constant $N_p R_e = K_p$. The parameter K_p is known as the setting constant or power constant, and will be different depending on the type of impeller used. As mentioned early, the laminar regime is in the range of $0 < R_e \leq 100$. However, for some impellers, this behavior may prevail up to $R_e = 100$. After this region, the transition to the turbulent regime is observed between values of $101 < R_e < 104$. Finally, in a standard tank that uses baffles, the turbulent regime will be easily observed because at that moment the power number remains constant irrespective of the Reynolds number. In the case of stirred tanks designs without baffles, the power number will decrease as Reynolds number increases even when working under the turbulent regime.
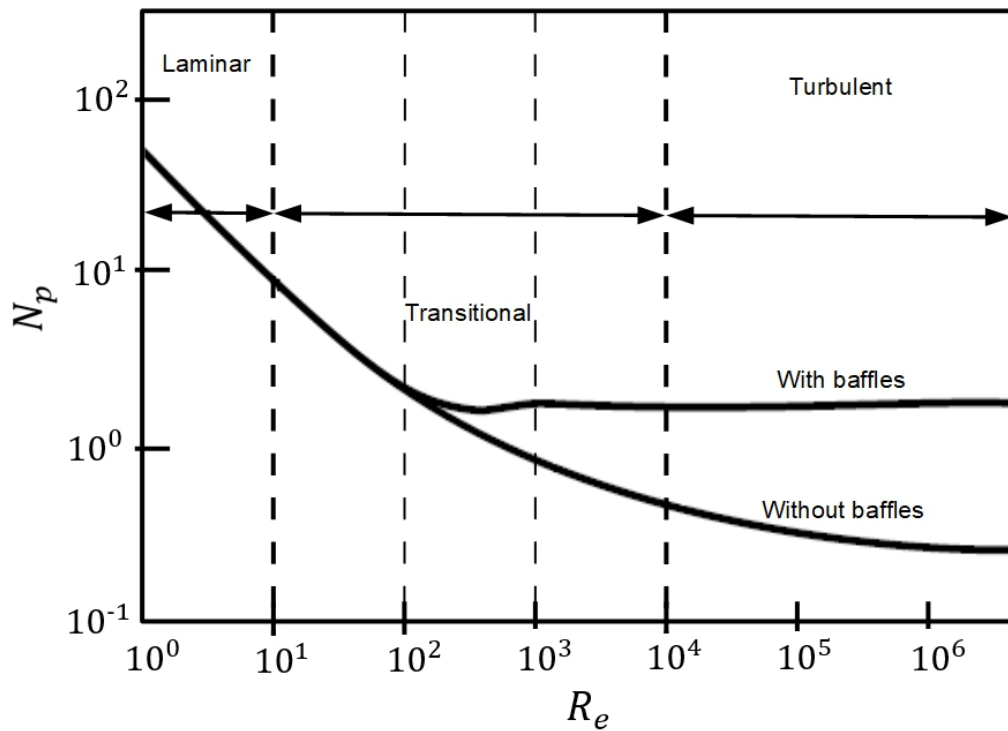
Figure 1.6. Power curve (Brauer (1979)).

On the other hand, figure 1.7 shows another power curve that can be useful. This consists of the ratio of gassed to ungassed power (P_g/P) for a constant value of Reynolds number, as a function of the aeration number $\left(Fl_g = \dot{Q}/ND_I^3\right)$. In this curve, the power ratio decreases with increasing superficial gas velocity (v_g) keeping constant the rotational speed. For very high gas loads the periphery of the impeller becomes flooded with gas, the power input becomes very low, and the gas rises by buoyancy along the shaft without much dispersion. In this region, the gas-liquid mass transfer is very low. For a very small gas load, P_g/P approaches to 1 and the gas is fully dispersed, both above the mixer and below the sparger. Here the gas-liquid mass transfer is good. For a fixed gas load we can move from the right to the left on figure 1.7 by increasing the rotational speed of the impellers, which avoid the flooding of them.
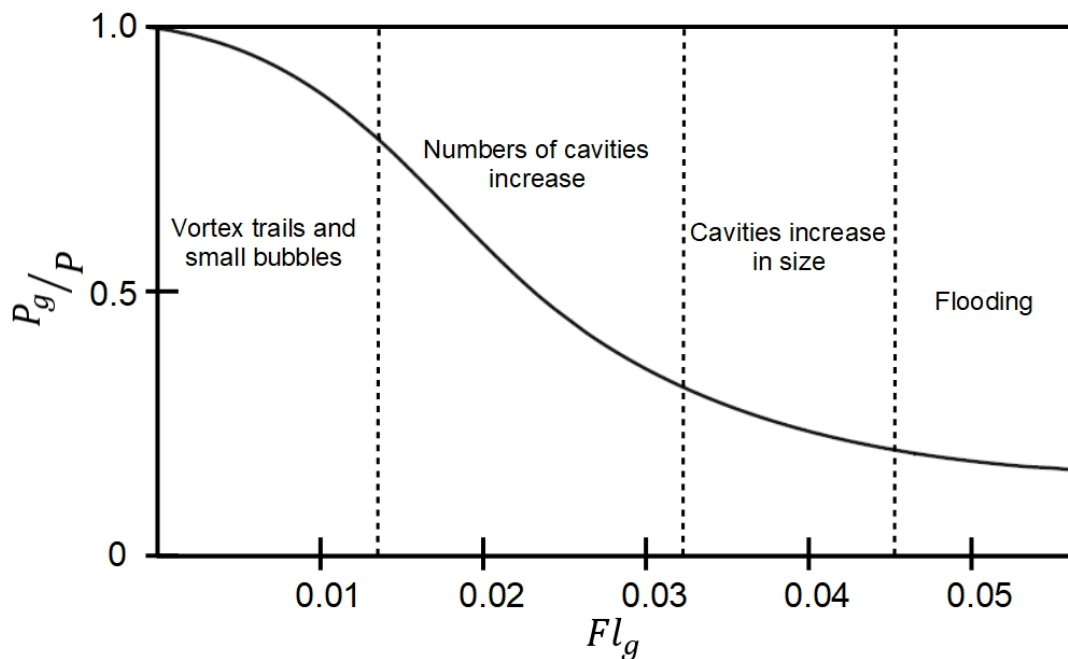
Figure 1.7. Power ratio as a function of the gas flow number.

1.6   Flow visualization in stirred tanks

The efficiency of a mixing system is highly influenced by the flow fields generated by the impellers within the tank (Chhabra and Richardson (1999)). These fields are affected by some parameters to reach an optimal mixing of biological models such as the velocity magnitude, turbulent intensity, and strain rates, among others. For instance, velocity fluctuations (turbulent intensity) help to improve the mixing process (Ottino and Ottino (1989)). Some authors have found that there is a close interaction between the morphology, the broth rheology, and the turbulent intensity of submerged fungal fermentation in stirred tank reactors (Ayazi Shamlou et al. (1994), Cui et al. (1998b), Nienow (2021b)). On the other hand, the turbulent intensity can be linked to the strain rates. As impellers rotate, biological models are subjected to deformation gradients, which eventually can lead to sub-lethal damage or even to cell death or alterations in the metabolic process of the cell (Prokop and Bajpai (1992b), Sánchez Pérez et al. (2006)). The damage levels depend on the intensity of the shear stress and the particular cellular species (Rodríguez-Monroy and Galindo (1999)). Due to the above, it is important to determine the distribution of strain rates throughout the tank, which allows for establishing whether a certain biological model will be subjected to forces that result in an adverse effect. In this sense, the visu-

alization of flow fields is of utmost importance when characterizing the hydrodynamics of a stirred tank.

Particle Image Velocimetry (PIV)

One of the techniques most commonly used to visualize flow fields in stirred tanks is the particle image velocimetry technique (Ayala et al. (2022), Besbes et al. (2015), Cortada-Garcia et al. (2018), Delnoij et al. (1999), Murgan et al. (2017)). When using the particle image velocimetry technique under conditions of a fully turbulent regime we can make measurements in 2D, which is sufficient for doing a good estimation of local quantities inside the tank. This technique is described below.

Figure 1.8 shows a typical PIV setup. The particle image velocimetry technique is an indirect measurement technique which allows determining the flow fields. The area of interest is seeded with tracer particles. After by means of a thin sheet of light the area is illuminated and with a high-speed camera a couple of images are taken at a time interval known. Then the velocity vectors are calculated by dividing the images into small interrogation areas in which a cross-correlation is applied to determine the displacement of the particles, since the time between the images is known, the calculation of the velocity of each particle is carried out through the equation 1.1

$$v_p = \frac{d(t_1) - d(t_2)}{\Delta t} \tag{1.1}$$

where $d(t_1)$ and $d(t_2)$ are the positions of the particle at time 1 and time 2, respectively.

All PIV systems consist basically of a light source, camera, tracer particles, and a processor. It does not exist a standard for these devices and their implementation depends on the type of study that carried out. A brief description of the devices that integrate the PIV is presented below.

Light source. Lasers are the light sources par excellence for PIV systems since they emit monochromatic light with a high energy density. The characteristics that the laser to be used must meet are:

- Provide enough light so that the light reflected by the particles can be detected by the camera.

- The duration of the pulse must be short enough so that the displacement of the particles, during exposure to the light pulse, is not significant.

- The time between the light pulses must be such that the displacement of the flux is not significant.
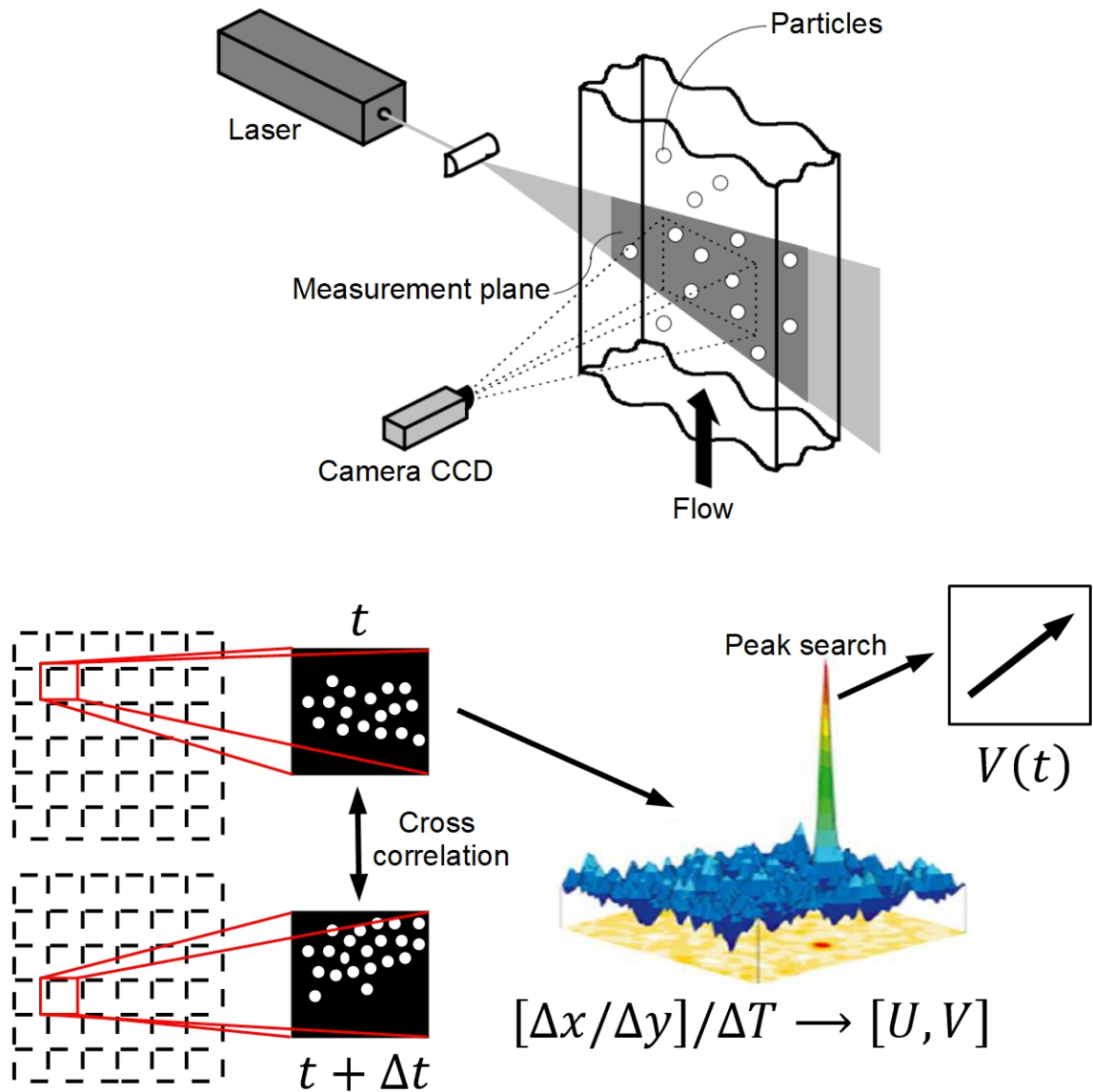
Figure 1.8. Standard configuration of a PIV acquisition system.

The lasers most commonly used are the Q-switched double-cavity Nd: YAG lasers because the pulses they generate are of short duration, having two cavities has a wide time range and the energy level of the pulses does not vary between them.

Cameras. The camera receives the light reflected by the tracer particles and therefore the position of these in the flow, the particles appear as light points on a dark background. The most used cameras in PIV systems are CCD and CMOS cameras; these are made up of sensor arrays called pixels that transform the light that falls on them into an electrical charge. When the information from the CCD is displayed on a monitor, the electrical

charge is converted to voltage so if a pixel received light reflected from a particle it will have a high output voltage, a white dot will be seen on the image; if it only received light from the background (noise) it will have a low output voltage, it will be a dark spot in the image.

Processor. The main piece of every PIV system is a computer built in a modular way, in which the correlation units are installed (responsible for calculating the vector maps), the input buffer (reads and saves the information coming from the camera and sends it to the correlation unit) and the synchronization unit (provides the connection ports between the processor and the other elements of the PIV system such as the laser and the camera). This is connected to a computer that serves as an interface with the user.

Tracers. As mentioned in the previous paragraphs, what is actually measured is the displacement of the tracer particles, so the accuracy with which the flow velocity is measured will depend on the correct selection of these. There are several factors to be considered when selecting a tracer, such as size, shape, and relative density with respect to the fluid and particle concentration. In general, the particles must be small enough to follow the flow and large enough to reflect enough light to be detected by cameras.

A useful criterion when selecting tracer particles is to calculate the response time of the particles, τ, which provides information on how quickly a particle can react to changes in flow velocity. For a spherical particle, it is defined as

$$\tau = \frac{d_p^2 \, \rho_p}{18\mu} \tag{1.2}$$

where ρ_p and d_p are the density and diameter of the particle, and μ is the viscosity of the fluid. To ensure that the particles follow the movement of the fluid, the response time must be less than the time between image acquisition.

Electrical Resistance Tomography (ERT)

When non transparent fluids or highly gassed fluids must be mixed the particle image velocimetry technique is ineffective. In this sense, the electrical resistance tomography technique is the most suitable for obtaining the flow fields under the conditions mentioned above.

The structure of a typical electrical resistance tomography system is composed of three main parts: sensors, data acquisition system, and image reconstruction system/host computer. Figure 1.9 shows electrical resistance tomography systems and their comprising units made by one of the main commercial manufacturers of process tomography units,

Industrial Tomography Systems (ITS).

Figure 1.9. ERT system and its comprising units manufactured by ITS (Sharifi and Young (2013)).

The operating principle of the electrical resistance tomography technique is based on measuring the resistance distribution in the area of concern. This is obtained by applying currents (or voltages) and measuring voltages (or currents) via electrodes mounted on the periphery of the domain (Pinheiro et al. (1999), Scott and McCann (2018)). Normally, the electrodes, located around the boundary of the tank, make electrical contact with the fluid inside the vessels and are connected to the data acquisition system (DAS) by co-axial cables to reduce electromagnetic noise and interference In electrical resistance tomography system, there is not constraint on the material of the tank wall. The only constraint would be that the sensors would be able to mount on the tank wall. As far as there is a difference between the conductivity of different phases induced, we can successfully use electrical resistance tomography to detect the changes. Below is a brief description of the components that integrate an electrical resistance tomography system.

The sensors consist of multiple electrodes arranged equispacially around the region of interest usually in the form of one or more electrode rings. The most common configuration is a circular pipe or vessel with 16 invasive but non-intrusive electrodes (Sardeshpande et al. (2017)). The sensors are usually manufactured from gold, platinum, stainless steel, brass, or silver, and they must-have characteristics such as low cost, ease of installation, good conductivity, and resistance. Multiple planes sensors provide the ability to acquire a description of the process in three dimensions (Mann et al. (1997)). In other words, 3D

scanning of the interior of any process vessel is made possible with electrical resistance tomography technique, giving spatial information with discrimination of the order of 10^3 with the fast acquisition.

The data acquisition system is the component which injects current and collects the quantitative information describing the conductivity distribution inside the vessel. It consists of signal sources, an electrode multiplexer array, voltmeters, signal demodulators, and a system controller. The data acquisition system is connected to the electrodes and the PC containing the image reconstruction algorithms. Depending on distinguishability and sensitivity to conductivity changes, there are various data collection strategies to choose from, including adjacent strategy, opposite strategy, diagonal strategy, and conducting boundary strategy. In the adjacent strategy, which is the most common strategy in conventional electrical resistance tomography due to minimal hardware requirements and fast image reconstruction, alternating current is injected from the data acquisition system to the electrodes using a pair of neighboring electrodes, and the resulting voltage is measured through all other neighboring electrodes. The alternating current drive current then rotates to the next electrode pair and the process of injecting current to neighboring electrodes is repeated until all independent pairs have been covered. For more exhaustive information on the systems that make up the electrical resistance tomography, you can consult the work made by Dickin and Wang (1996).

Finally, it is worth mentioning that the techniques described allows determining the velocities in a plane. However, there are other techniques that allow measuring velocities punctually (velocity in a single point) such as Hot-Wire Anemometry, and Laser-Doppler Velocimetry, which has some advantages about the techniques that measuring full-field velocity measurements. For more information on these techniques, can consult the work reported by Mavros (2001).

1.7   Literature review

As mentioned before mixing has been widely recognized as a key unit operation encountered in many industrial processes such as in food, metallurgical, chemical and pharmaceutical, among others. Stirred tanks are commonly used in such industries with the aim of obtaining a complete homogenization of products from single o several phases. Particularly, the gas-liquid systems have been the subject of numerous studies in recent years (Liu et al. (2021), Forte et al. (2021a), Yang et al. (2020), Guan et al. (2020)). These systems are characterized for having high mass and heat transfer coefficients, good liquid and gas-mixing capacities, a wide range of liquid residence time possibilities, as well as the

possibility of handling a wide range of superficial gas velocities. On the other hand, the advantages of using multiple-impeller systems over single-impeller systems in bioprocesses have been reported elsewhere (Armenante et al. (1992), Armenante and Chang (1998), Xinhong et al. (2008), Li et al. (2009)). Particularly, systems having two or three coaxial impellers have been the most investigated configurations in the last years. However, systems having more than three coaxial impellers draw more energy and do not necessarily enhance the mixing process (Davis (2009)). On the other hand, some authors have compared the performance in terms of power consumption, gas hold-up, mass transfer, mixing time, and the shear rates of various triple and double impeller configurations mounted on a shaft. These combinations include axial and radial flow impellers, small-diameter (Rushton turbine), and large-diameter (ellipse gate impeller) impellers among others. In general, the results of these combinations showed that putting different flow pattern impellers on the shaft has a better performance than putting impellers with the same flow pattern. (Buffo et al. (2016), Wan et al. (2016), Xie et al. (2014a), Xie et al. (2014b)). Some studies reporting the advantages of using double and triple impellers are mentioned below.

According to Yi et al. (2006), mixing time can be reduced 50% and 75% in stirred tanks equipped with two or three coaxial impellers, respectively. Gas hold-up is another parameter to be considered when working with two-phase flows. According to Arjunwadkar et al. (1998) and Gogate and Pandit (1999) the gas hold-up can be enhanced up to 60% when using multiple-impellers systems compared to single systems. Regarding the power demand, the power consumption per impeller decreases with an increase in the number of impellers Nienow and Lilly (1979). On the other hand, the volumetric mass transfer coefficient, $K_L a$, can be also enhanced with multiple-impeller systems; for instance, when adding an impeller to single-impeller systems, an improvement of about 34% and 120% can be obtained by adding a second and third impeller to the agitation shaft, respectively Puthli et al. (2005a). Although these systems have many advantages, they are not efficient for the gas dispersion in highly viscous fluids. The use of coaxial mixers appears to be a promising solution for this problem and numerous studies on the performance of these mixers have been carried out in recent years (Hashemi et al. (2016b), Hashemi et al. (2016a), Hashemi et al. (2018), Liu et al. (2018), Jamshidzadeh et al. (2020b), Jegatheeswaran and Ein-Mozaffari (2020), Jamshidzadeh et al. (2020a), Jamshidzadeh et al. (2020b)).

Nowadays, several types of impellers are available to be used for different applications, either in single-impeller systems or multiple-impellers ones. Some studies demonstrate that the traditional Rushton turbine impeller has some advantages over other impellers for

the gas-liquid mixing operations (Nienow (1996)). Although, Rushton turbines draw less power when operating in the turbulent regime, the flow is prone to dead zones, as a result of its poor pumping capacity. To overcome such a drawback, axial-flow impellers have been designed and tested. However, the use of such impellers leads to torque instabilities and higher power demand when operated under the down-pumping mode (McFarlane and Nienow (1995)). Axial-flow impellers operating under the up-pumping mode have shown some advantages over the down-pumping mode, such as less power consumption, fewer torque instabilities when operated in aerated media systems (Hari-Prajitno et al. (1998), Aubin et al. (2001)).

To overcome the deficiencies exhibited by the aforementioned impellers, a mixed-flow impeller (ARI) was proposed by Ascanio et al. (2003) consisting of a combination pitched blades and straight blades for generating both axial and radial flow, respectively. Pakzad et al. (2013c) and Pakzad et al. (2013a) evaluated that impeller with an anchor placed coaxially with shear-thinning fluids and fluids possessing yield-stress. Its hydrodynamic performance was compared with a Rushton turbine and A200 impeller as central impellers by means of Electrical Resistance Tomography (ERT) and Computational Fluid Dynamics (CFD). The authors found that the mixed-flow impeller had an improved performance when operated a higher speed ratio with respect to the anchor impeller.

The power consumption, mass transfer capacity, mixing time, and gas hold-up are global parameters that are strongly affected by the flow patterns inside the tank. These flow patterns depend on the impeller type, the number of impellers, the number, and geometry of blades, the fluid properties, and the agitation speed (García-Ochoa and Gómez (1998), Arjunwadkar et al. (1998), Bouaifi and Roustan (2001), Chapple et al. (2002), Moucha et al. (2003), Sardeing et al. (2004), Kumaresan and Joshi (2006)). The efficiency of a mixing system is highly influenced by the local parameters generated by the impellers (Chhabra and Richardson (1999)), which can be obtained through the flow patterns. For example, reaching an optimal mixing of biological models is a function of some local parameters such as the velocity magnitude, turbulent intensity, and strain rates. For instance, velocity fluctuations (turbulent intensity) help to improve the mixing process (Ottino and Ottino (1989)). Some authors have found a close interaction between the morphology, the broth rheology, and the turbulent intensity of submerged fungal fermentation in stirred tank reactors (Cui et al. (1998a), Shamlou et al. (1994), Nienow (2021a)). On the other hand, the turbulent intensity can be linked to the strain rates. As impellers rotate, biological models are subjected to deformation gradients, which eventually can lead to sublethal damage or even to cell death or alterations in the metabolic process of the cell (Prokop and Bajpai (1992a), Pérez et al. (2006)). The damage levels depend on

the intensity of the shear stress and the particular cellular species. Due to the above, it is essential to determine the distribution of strain rates throughout the tank, which allows for establishing whether a certain biological model will be subjected to forces that result in an adverse effect. In this sense, the visualization of flow patterns is of utmost importance when characterizing the hydrodynamics of a stirred tank.

Most of the studies reported in the literature have been focused on evaluating the global parameters (Moucha et al. (2003), Bouaifi and Roustan (2001), Issa (2016)), or the local parameters (Hidalgo-Millán et al. (2012), Aubin et al. (2004), Li et al. (2011)) of stirred tanks in an independent way. However, few works analyzing both global and local parameters in stirred tanks have been reported (Xie et al. (2014b), Mancilla et al. (2016)).

Objective

The aim of the present work is to perform a comprehensive assessment of an aerated stirred tank equipped with multiple-impellers by analyzing both their local and global parameters.

Particular objectives

■ Assess and compare the hydrodynamic performance of three types of open-clearance impellers.

■ Analyze the flow fields by means of fluid mechanics through a flow visualization technique.

■ Investigate the hydrodynamic performance of a new hybrid impeller both locally and globally and compare it with standard impellers.

■ Analyze the existing relationship between the local parameters with global parameters in stirred tanks.

Chapter 2

Methods and materials

2.1   Stirred tank

The first stage of this work consisted of the design and fabrication of a stirred tank for carrying out both hydrodynamics and thermal tests. The general design of a stirred tank is in the function of the internal diameter of the vessel. Once this parameter is known the rest of the design such as impellers, baffles, and the sparger can be carried out. The following briefly describes the design of each other of the devices aforementioned.

Tank

As mentioned early, a stirred tank conventional mixing system consists of a vertical cylindrical vessel with a circular cross-section together with an ellipsoidal or torispherical bottom in order to avoid stagnation zones. Figure 2.1 shows the tank used in this work. The tank is a vessel cylindrical made of glass with an inner diameter T of 190 mm and a total high H_T of 420 mm, which provide a total volume V_T of 0.011 m^3 and an operation volume V_o of 0.008 m^3 ($V_o = 0.75 \ V_T$). In this particular case, unlike conventional tanks, the tank used in this work had six ports that were placed on the tank wall with the aim of carrying out temperature measurements through their vertical position. Table 2.1 summarizes the meaning of each one of the parameters that integrate the tank.
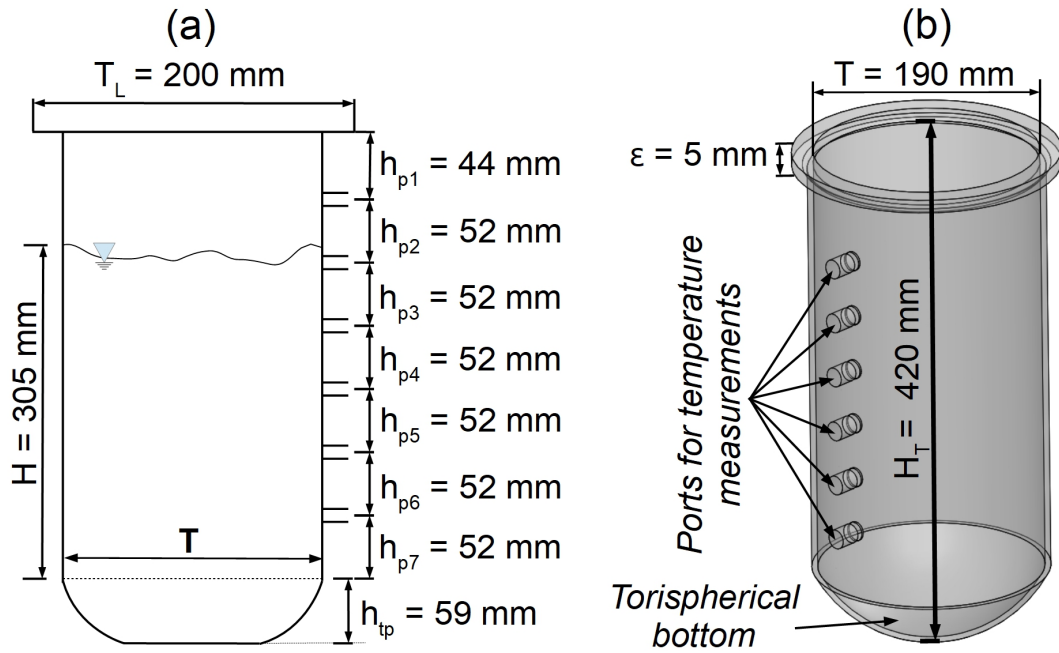
Figure 2.1. Cylindrical tank used in this work: (a) 2D view of the tank with the distribution of ports to measure temperature; (b) 3D view of the tank.

Table 2.1. Parameters of the tank used in this work.

Parameter	Meaning
H	Liquid height
H_T	Total height
h_{p1}	Lip to top port distance
h_{p2}	Distance from top port to second port
h_{p3}	Distance from second port to third port
h_{p4}	Distance from third port to fourth port
h_{p5}	Distance from fourth port to fifth port
h_{p6}	Distance from fifth port to sixth port
h_{p7}	Distance from the sixth port to the straight part of the tank
h_{tp}	Distance from the straight part of the tank to the bottom of the tank
T	Internal diameter of the tank
T_L	Diameter with tank lip
ε	Glass thickness

Impellers

In the present work, open-clearance impellers were used, which are used for the mixing fluids low to medium viscosity. Three types of impellers were built, which were based on

three dominant flow patterns. Three impellers with a diameter of $D_I = T/3$ were used, namely: axial-radial impeller (ARI), pitched blade turbine (PBT), and Rushton turbine (RT) .

Figure 2.2 shows the impellers used in this work. The three impellers were designed and constructed following the standard relative dimensions reported by Paul et al. (2003). For the radial flow pattern, a traditional Rushton turbine was constructed. The axial flow pattern was created by means of a pitched blade turbine; both impellers had six blades. On the other hand, for creating a mixed flow pattern a hybrid impeller (Ascanio et al. (2003)) that consisted of a combination of a tilted blade and a straight blade called axial-radial impeller was used.
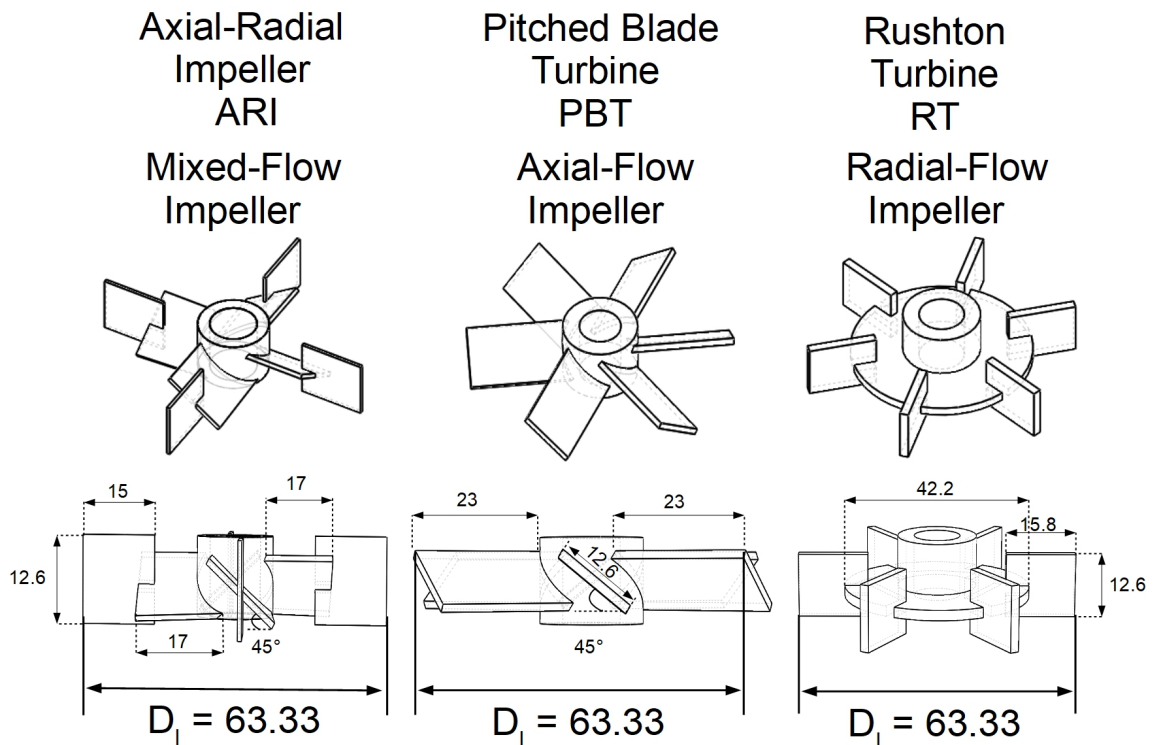
Figure 2.2. Impellers used in this study. Dimensions in millimeters.

Wall baffles and sparger

As aforementioned, baffles usually are used to get better the mixing quality. These devices typically consist of solid surfaces positioned in the path of tangential flows generated by the impellers. In the present work, standard baffles configurations were used (Paul et al. (2003)), which consisted of four vertical planes having a width equal to one-twelfth of

the tank diameter. Four baffles were manufactured with a width J of 15.8 mm ($T/12$) placed 45° and with a small spacing between baffles (gap) and the tank wall of 2.58 mm (0.015 T), in order to eliminate dead zones.

As mentioned before, in gas-liquid systems, a sparger is used when a gas is supplied to the liquid for efficient gas-liquid contacting for mass transfer and reaction. Nowadays, many configurations of spargers are available. However, numerical studies have been shown that the ring sparger shows a more homogenous dispersion and low dead zones (Amer et al. (2019)). This configuration has small holes that, when connected to pressure air, are distributed as fine bubbles in the stirred tank to allow effective aeration. Although there are no procedures standards for its design and manufacture, it is recommended that the inlet and outlet areas of a ring sparger should be equal, which helps of minimizing the air pressure drop while providing a uniform distribution of the same (Kulkarni et al. (2007)). In the present work, a ring sparger was positioned below the impeller at a distance h_s of 59 mm measured from the bottom of the tank. The sparger diameter was approximately 0.8 times the impeller diameter ($D_s = 50$ mm) having 16 holes of 1.5 mm equally distributed around the ring. The sparger was designed with the standard dimensions reported by Paul et al. (2003).

Experimental setup

Finally, for performing the hydrodynamic and thermal tests an unique configuration was adopted based on the geometrical parameters of the stirred tank designed. As mentioned above the operation volume of the stirred tank was 0.008 m^3, which gave us a height of the liquid H of 305 mm. The aspect ratio H/T, in this case, was 1.6, hence more of one impeller is necessary (Paul et al. (2003)) to have a more homogeneous mixing. Due to this, equation 2.1 was used to determine the rank of impellers that could be used.

$$\frac{H - D_I}{D_I} > N_i > \frac{H - 2D_I}{2D_I} \tag{2.1}$$

where H is the height of the liquid in the tank and N_i is the number of impellers (Nauman (2008)). Equation 2.1 throws us that we can use from three to four impellers for the stirred of our system. However, according to You et al. (2014) having more than three impellers on the shaft results in a noticeable increase in power consumption, and the mixing process is not necessarily improved. Therefore, sets of three impellers were used in the present work namely: axial-radial impellers (ARIs), pitched blade turbines (PBTs), and Rushton turbines (RTs), which provide a mixed, axial, and radial flow pattern, respectively. Both ARIs and PBTs operate in the down-pumping mode. On the other hand, the spacing

between impellers used in this work was $(1D_I)$, which is a spacing standard, and besides, according to report by Hudcova et al. (1989) this configuration reduces the demand for power by the impellers.

Figure 2.3 shows the configuration used in this work for carrying out both hydrodynamic and thermal tests. The lower impeller was mounted on the shaft at a distance of 31.6 mm (C_1) measured from the sparger. The mid impeller was placed at a distance of 63.3 mm (C_2) measured from the lower impeller and the upper one was placed at a distance of 63.3 mm (C_3) from the mid impeller. With the aim of minimizing air intake to the working liquid, the distance between the upper impeller and the free surface was set to 92 mm (C_4). Impellers were driven by a P100 motor of Applikon Biotechnology and the rotation velocity was carefully controlled by a stirred controller P100 ADI 1032 of the same brand. On the other hand, table 2.2 summarizes the experimental conditions used for this work.
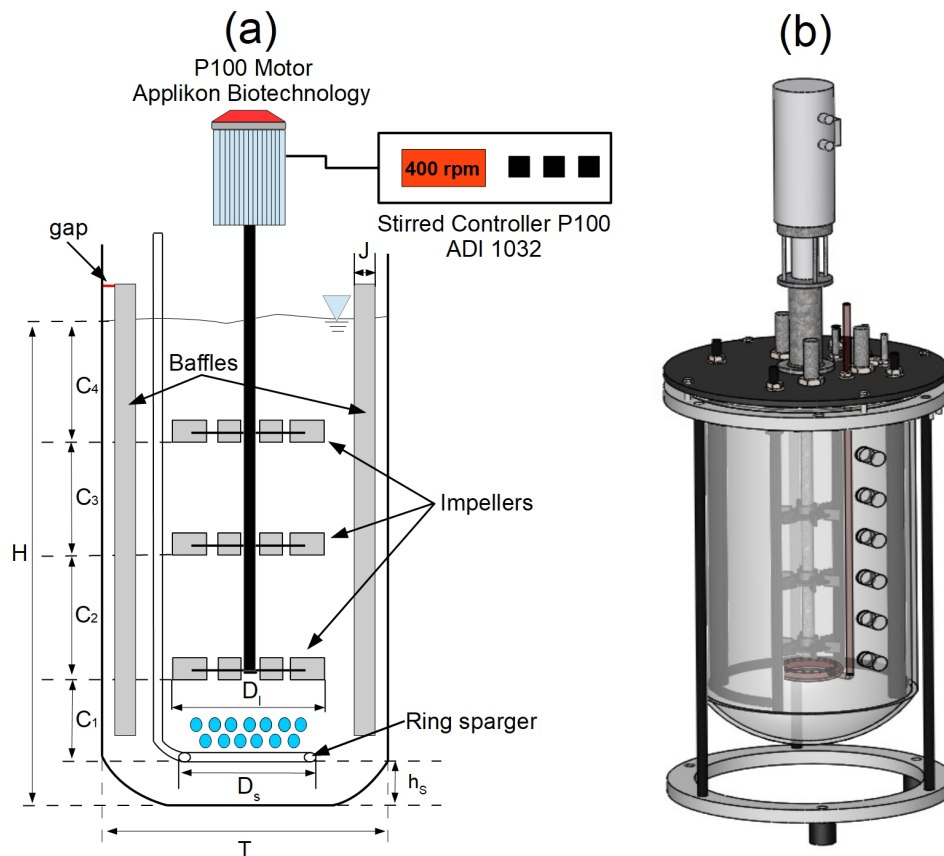
Figure 2.3. Distribution of impellers, baffles, and the ring sparger in the tank: (a) 2D view; (b) 3D view.

Table 2.2. Dimensional parameters.

Parameter	Dimension
C_1	31.6 mm
C_2	63.3 mm
C_3	63.3 mm
C_4	92 mm
D_I	63.3 mm
D_s	50 mm
gap	2.58 mm
H	305 mm
h_s	59 mm
J	15.8 mm
T	190 mm
V_o	0.008 m^3

2.2 Flow visualization

Figure 2.4 shows the experimental setup used to obtain the flow fields under unaerated and aerated conditions with the sets of impellers investigated. The Particle Image Velocimetry (PIV) was used to obtain the two-dimension flow fields. For that purpose, a Nd: YAG double-pulsed laser (532 nm-green light, 30 mJ and 100 Hz) and a high-speed Phantom camera (SpeedSense 9040, 1632 x 1200 pixels resolution) coupled to a Nikon lens of 50 mm f/2.8D were used. The laser was coupled to an optical array to generate a light sheet of about 3 mm thickness.

The camera was placed perpendicularly with respect to the laser light sheet. The flow was seeded with tracer particles. For the ungassed tests, silver-coated hollow spheres of 10 µm diameter were used as particle tracers. On the other hand, for gassed tests polyamide microspheres (50 µm mean diameter) coated with rhodamine 6G were added. A 300 nm optical filter coupled to the camera lens was used to only obtain the light reflected by the particles; in that way, it was possible to minimize the light reflected by the bubbles and other surfaces. For synchronization purposes, the laser and the camera were connected to a PCI-6601 card (Timerbox). The agitation shaft, baffles, sparger and the impellers were all painted black to avoid light reflection. The tank was placed into a rectangular jacket filled with glycerol for minimizing the optical distortion due to the tank curvature and also to reduce significant changes of the refraction index.

Finally, for a better visibility of the flow, the measurements were made at an angle of 0° just in front of one of the baffles. With the aim of obtaining statistically robust results,

400 individual images with the phase/locking technique were obtained and processed. For that purpose, an electronic shutter was placed in the agitation shaft and connected to the visualization system in such a way that the position of the impellers with respect to the camera and the baffles was always the same. A cross-correlation algorithm was used to obtain the velocity vectors using an interrogation area of 32 x 32 pixels with 50% overlap and a time between pulses of 1500 μs, obtaining a spatial resolution of 2.7 mm x 2.7 mm (cell size). Flow patterns obtained from the experiments are reported in terms of the local parameters such as:

1. Flow fields and velocity magnitude

2. Vorticity

3. Vertical velocity

4. Turbulent intensity

5. Strain rates

6. Reynolds stresses
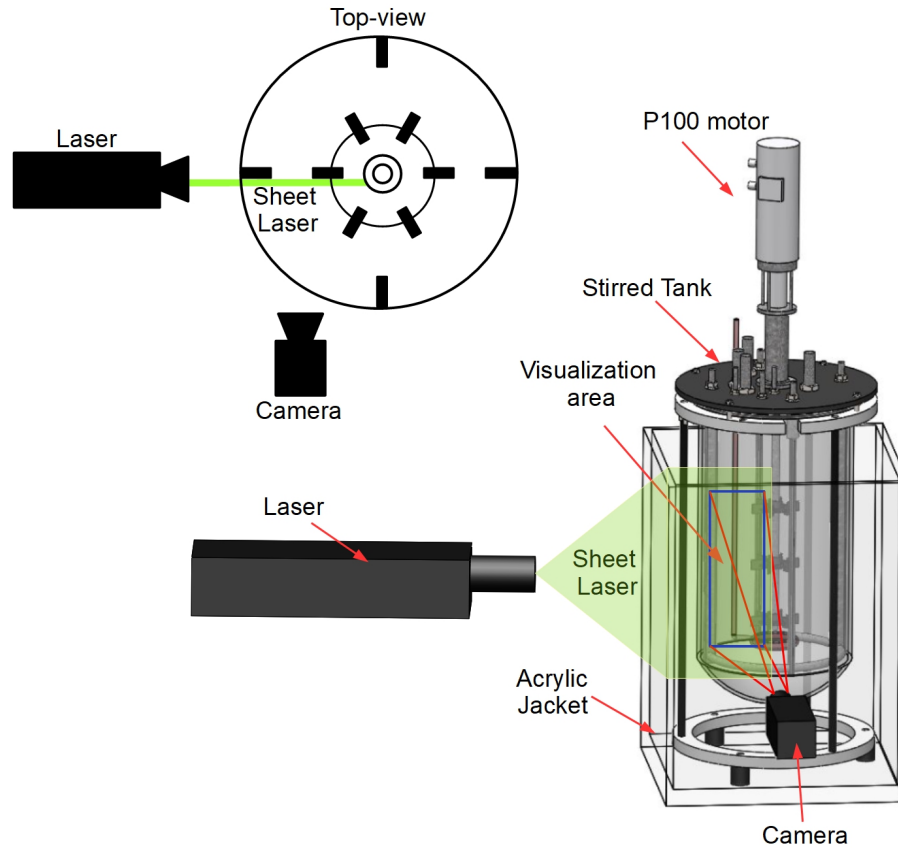
Figure 2.4. Particle image velocimetry setup used in the present work.

2.3   Evaluation of power consumption

The power drawn by the impellers was determined by measuring the torque as described elsewhere (Ascanio et al. (2013)). For that purpose, a rotary torque sensor (Futek TRS300) was coupled between the motor and the shaft (see figure 2.5). This torquemeter had two couplings KTR ROTEX (GS28), which help to reduce the vibrations of the shaft, allowing the continuous measurement of the torque as a function of the rotation speed. With the aim of measuring the effective torque M_e, the residual torque due to friction M_f was first measured with the empty tank. Then, the torque with the working fluid M_d contained in the tank was measured. The effective torque was obtained by means of the following expression:

$$M_e = M_d - M_f \tag{2.2}$$

and the power drawn by the impellers under gassed conditions was calculated as:

$$P_g = 2\pi M_e \tag{2.3}$$

For scaling purposes, the mixing system should be characterized in terms of dimensionless numbers. In the present work, the power characteristics are reported with the gassed power number N_{pg} as a function of the flow number Fl_g under gassed conditions as follows, respectively:

$$N_{pg} = \frac{P_g}{\rho N^3 D_I^5} \tag{2.4}$$

$$Fl_g = \frac{\dot{Q}}{N D_I^3} \tag{2.5}$$

where $\dot{Q}$ is the volumetric gas flow rate, which was measured with a rotameter.

2.4 Evaluation of mass transfer capacity

The mass transfer capacity of the air supplied to the working fluid was analyzed in terms of the volumetric mass transfer coefficient using the dynamic method reported by Garcia-Ochoa and Gomez (2009). In brief, the method consists of dexoyginating the working fluid by sparging nitrogen until reaching the oxygen saturation in the tank was equal to zero. Then, the air is again supplied to the tank through the sparger, and the oxygen saturation was monitored employing a polarographic dissolved oxygen electrode (InPro 6800) over time until reaching ninety percent of oxygen saturation (see figure 2.5). The mathematical model describing such a process is:

$$C_l = \left(1 - e^{-K_L a.t}\right).C^* \tag{2.6}$$

where C_l is the oxygen concentration in percentage of saturation, which increases over time t, C^* is the saturation oxygen concentration in the liquid phase, which is expressed as percentage of saturation and, $k_L a$ is the volumetric mass transfer coefficient. This equation describes the oxygen concentration over time from restarting aeration, therefore $k_L a$ is determined from the slope of the plot $In\left[1 - \frac{C_l}{C^*}\right] vs\ t$, as is depicted in figure 2.6.
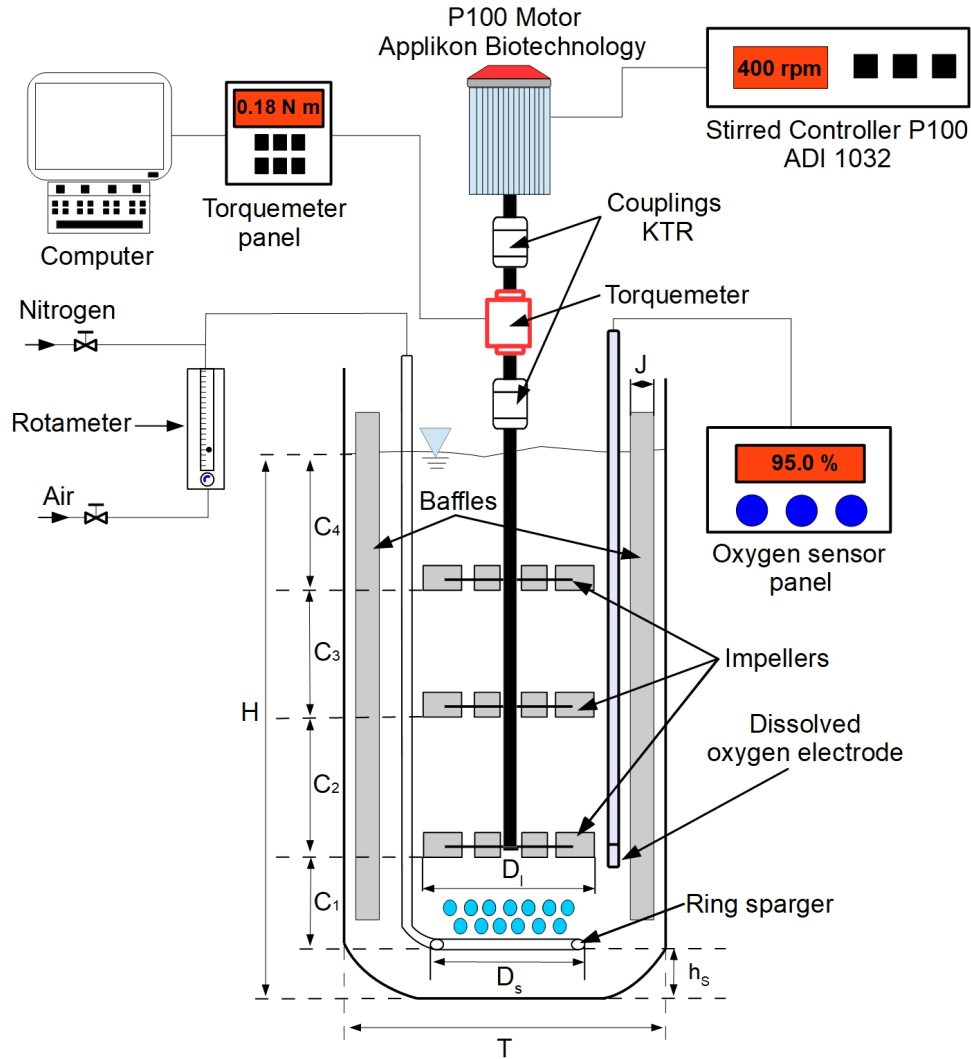
Figure 2.5. Experimental setup for evaluating the power consumption and mass transfer capacity.

2.5   Evaluation of overall gas hold-up

In this work, the overall gas hold-up was calculated by measuring the liquid level difference. A ruler with a resolution of 1 mm was fixed on the outer wall of the stirred tank for the measurement of the liquid level before and after aerating. The ratio of the difference to the original liquid level H_0 and the liquid level with gas H_g was defined as the overall gas hold-up. Mathematically the overall gas hold-up was calculated as:

$$\varepsilon_g = \frac{H_g - H_0}{H_0} \qquad (2.7)$$
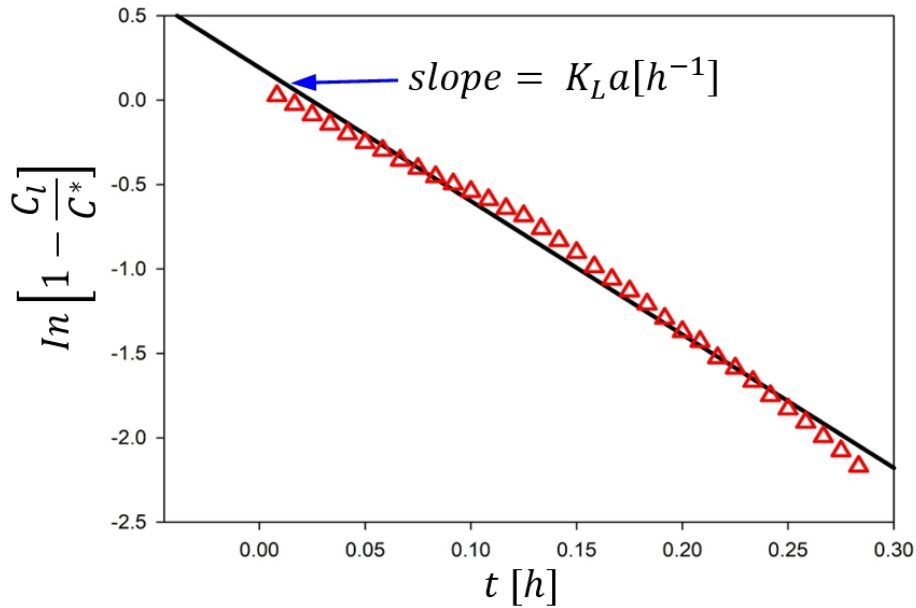
Figure 2.6. Schematic description of the indirect measurement of the volumetric mass transfer coefficient by the classical dynamic technique.

2.6   Evaluation of pumping capacity

Finally, an important parameter that should be quantified is the amount of fluid pumped by each one of the sets of impellers. An important parameter to characterize the above is the pumping capacity. This parameter was inferred from the velocity fields and defined as follows:

$$Q_x = \int_0^y \overline{u}\left(y\right) dxdz \tag{2.8}$$

$$Q_y = \int_0^x \overline{v}\left(x\right) dydz \tag{2.9}$$

The total amount of fluid pumped by the sets of impellers is quantified as:

$$Q_T = \sum Q_x + \sum Q_y \tag{2.10}$$

The pumping capacity of the sets of impellers in the present work is reported in terms of the pumping number $\left(N_q\right)$, which was calculated as:

$$N_q = \frac{Q_T}{ND_I^3} \tag{2.11}$$

2.7   Working fluid

The tank was filled with the working fluid, which was made up of sodium alginate dissolved in distilled water at a concentration of 1 g/L. The main rheological properties such as dynamic viscosity and density were measured with a stress-controlled rheometer using the concentric cylinders configuration, and a simple densimeter, respectively. The dynamic viscosity and the density was $\mu = 5 \ mPa \cdot s$, and $\rho = 997 \ kg/m^3$, respectively. On the other hand, figure 2.7 shows that the mixture behaves as a Newtonian fluid.
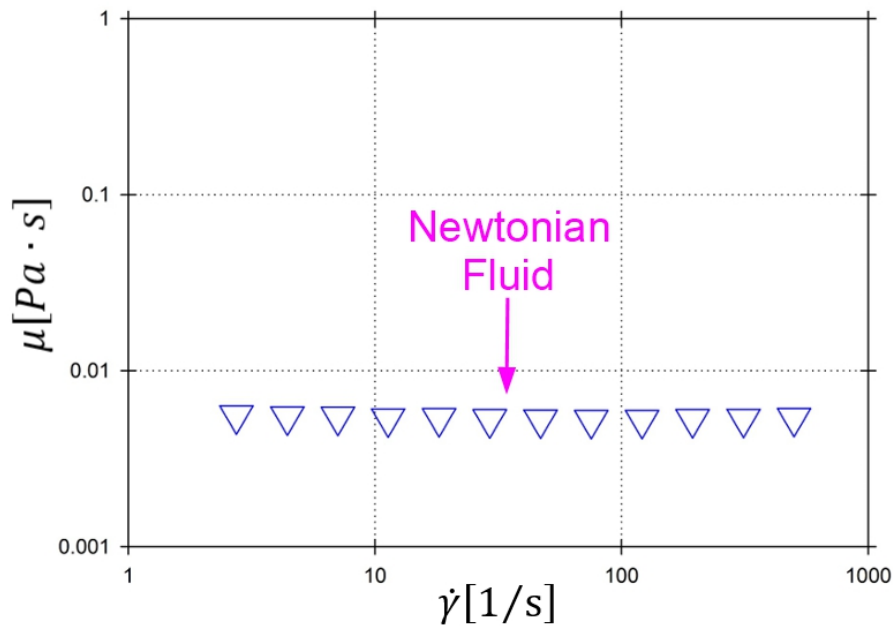
Figure 2.7. Flow curves for sodium alginate with a concentration of 1 g/l.

Finally, for carrying out the analysis of the local parameters, the rotational speed N was fixed at 6.666 rps (400rpm), and for the gassed-phase, the airflow rate $\dot{Q}$ was fixed to 2 l/min, equivalent to 0.25 vvm. Such conditions were based on the experimental works reported elsewhere for applications in fermentation processes (Abdella et al. (2020), Czinkóczky and Németh (2020), Shu et al. (2019), Valdez et al. (2021)). On the other hand, according to the power characteristic curve shown in figure 2.8 and the Reynolds

number obtained under the conditions aforementioned (5.2×10^3), the flow inside the tank was in the turbulent regime (Xie et al. (2014a)), therefore a reasonable estimation of the local quantities can be obtained from 2-D measurements.
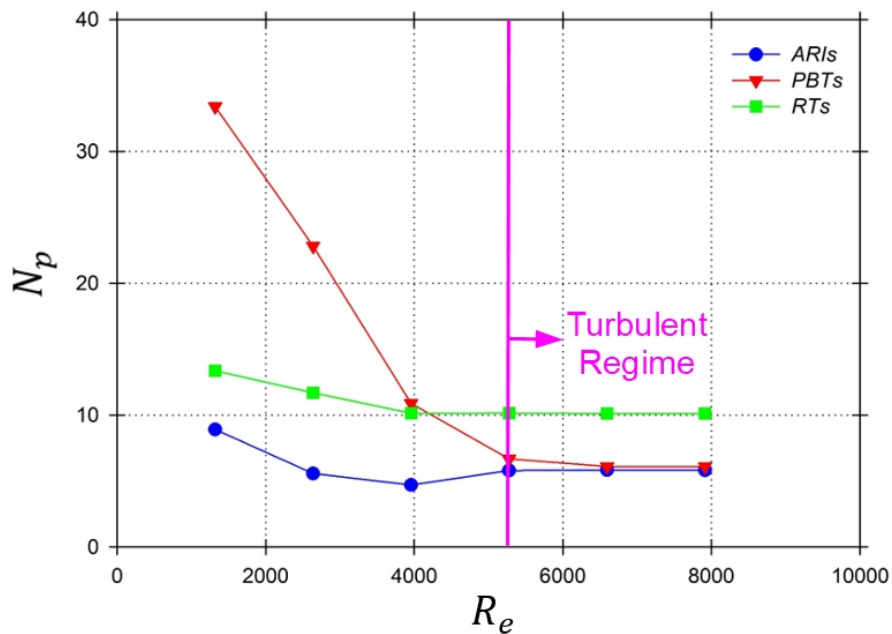
Figure 2.8. Power characteristic curve for the three sets of impellers investigated in the present work.

Chapter 3

Results and discussion

The first part of the results shows the local parameters of the three sets of impellers analyzed by means of the particle image velocimetry technique.

The local parameters were reported in terms of flow fields, velocity magnitude, vorticity, vertical velocity, turbulent intensity, strain rates, and Reynolds stresses. On the other hand, the results are shown with the horizontal and vertical dimensions, X and Y, respectively, normalized with the radius of the tank $(T/2)$, and the impellers' contours are illustrated with solid lines.

3.1   Flow fields and velocity magnitude

Figure 3.1 shows the averaged flow fields obtained in the X-Y plane for the axial-radial impellers (left column), the pitched blade turbines (middle column), and the Rushton turbines (right column) for single-phase (first row) and gassed (second row) conditions, respectively. The color scale shows the velocity magnitude normalized by the impeller tip velocity $(V_{tip} = \pi N D)$, which was calculated as:

$$|V^*| = \frac{\sqrt{u^2 + v^2}}{V_{tip}} \tag{3.1}$$

Figure 3.1 (a) shows the flow patterns generated by the axial-radial impellers under ungassed conditions. In this case, the upper impeller discharges the flow downwards close to the shaft and also, a weak vortex structure is generated near to the impeller tip. Another weak vortex is generated between the lower impeller and the tank wall. Finally, the mid impeller discharges the flow in both directions (radial and axial). Under gassed conditions, a similar trend is observed (figure 3.1 (d)); however, the average velocity is

slightly increased when supplying gas. Such a flow distribution is indeed a result of the interaction of the flow discharged by these impellers. These findings are in good agreement with the results reported elsewhere (Pakzad et al. (2013b)).

Figure 3.1 (b) shows the flow patterns of the pitched blade turbines under ungassed conditions. As expected, the pitched blade turbines create mainly an axial flow pattern; i.e., an axial down pumping flow for this case: an upward flow near the wall tank and a downward flow near the impeller's shaft. A vortex structure is generated at the bottom of the tank. On the other hand, under gassed condition (figure 3.1 (e)) no significant differences in the flow pattern are observed compared to the single-phase case. When operating the pitched blade turbines in the down-pumping mode, the average velocity is about 15% higher under gassed conditions than ungassed one.

For the Rushton turbines, single-phase condition (figure 3.1 (c)), four vortex structures are observed close to the impellers; a pair-vortex are observed between the mid and upper impellers while a second pair is observed in the vicinity of the lower impeller. There are also weak flow regions (quasi-static and dead zones) near the impeller's shaft. On the other hand, figure 3.1 (f) shows the flow patterns for the Rushton turbines with gas flow (0.25 vvm). Clearly, the flow behavior is similar to the previous one just with a remarkable increase in the velocity magnitude, likely due to the supplied gas. It is worth noting that the flow pattern created by the lower-impeller and mid-impeller agree with the findings reported by Rutherford et al. (1996), which is known as the merging flow created by two vortices with opposite directions of rotation. On the other hand, the upper-impeller poorly interacts with the mid one, very likely by the short distance from the free surface to the upper-impeller.

When comparing the sets of impellers, larger high-velocity regions are created by the Rushton turbines. However, quasi stagnant regions exhibiting poor interaction with the rest of the tank are also observed. This phenomenon could be even more noticeable with higher viscosity fluids. It is well known that radial flow impellers such as the Rushton turbines are prone to create well mixed regions (caverns) leading to unhomogenized products (Hirata et al. (1994)), which result from a poor interaction with the rest of the vessel. Under these conditions, although lower velocity magnitude levels were obtained with mixed flow impellers, a better flow distribution throughout the tank is observed. This leads to think that the axial-radial impellers could be an attractive alternative for two-phase flows with more viscous liquid phases.

Figure 3.1. Flow fields in the X–Y plane at $N = 400$ *rpm* for: axial-radial impellers: (a) single-phase, (d) 0.25 *vvm*; pitched blade turbines: (b) single-phase, (e) 0.25 *vvm*; Rushton turbines: (c) single-phase, (f) 0.25 *vvm*.

3.2 Vorticity

The vorticity indicates the rate of fluid rotation. This parameter provides information about the gas hold-up capacity of the impellers. In general, vortical structures are associated with high vorticity. Figure 3.2 shows the azimuthal component of the vorticity field, ω_z, in the X-Y plane for the axial-radial impellers (left column), the pitched blade

turbines (middle column), and the Rushton turbines (right column) for single-phase (first row) and gassed (second row) conditions, respectively. The vorticity was obtained by calculating the curl of the X-Y vector field as:

$$\omega_z = \frac{\partial u}{\partial y} - \frac{\partial v}{\partial x} \tag{3.2}$$

The color scale shows the vorticity normalized by $2V_{tip}/T$

Figure 3.2 (a) shows the ungassed vorticity field for the axial-radial impellers. In this case, three mid-vorticity regions are generated; one at the top of the tank, another one between the mid and the lower impeller, and a third one at the bottom of the tank. On the other hand, under gassed conditions (figure 3.2 (d)), no big difference is noticed with respect to the single-phase case. Two counterclockwise vortical structures are observed on the upper side and one more clockwise structure on the lower side of the tank. The vorticity of the axial-radial impellers is consistent with their low velocity magnitude (figure 3.1 (a) and 3.1 (d)).

For the pitched blade turbines in a single-phase, mid-vorticity regions are formed close to the shaft (figure 3.2 (b)); however, near the wall of the tank, there is an important vertical current resulting in strong velocity gradients, so that no vortices are generated. On the other hand, as figure 3.2 (e) shows, quite similar behavior is observed under gassed conditions with slightly larger vorticity regions close to the impellers' blades.

Figure 3.2 (c) shows the vorticity fields generated by Rushton turbines under ungassed conditions. Two vorticity structures are observed close to the upper impeller. Another slightly larger vorticity region is noticed near the mid impeller tip and one larger region is formed by the lower impeller. On the other hand, figure 3.2 (f) shows the vorticity when the gas is supplied. In this case, although there is a trend similar to the previous case the structures are more uniform.

As can be seen, the vortex structures for the three sets of impellers depend on their velocity and evidently the capacity to create vortexes through the tank. These structures increase their size as the air is supplied. On the other hand, according to what is shown by the vorticity maps the Rushton turbines will have better gas hold-up compared with the other two sets of impellers due to their vortex structures are larger and with better distribution through the tank.

Figure 3.2. Vorticity maps in the X–Y plane at $N = 400$ *rpm* for: axial-radial impellers: (a) single-phase, (d) 0.25 *vvm*; pitched blade turbines: (b) single-phase, (e) 0.25 *vvm*; Rushton turbines: (c) single-phase, (f) 0.25 *vvm*.

3.3   Vertical currents

One parameter that can be extracted from the flow fields shown in the previous section is the vertical currents induced in the tank. These currents will transport the fluid from the bottom to the top of the tank and viceversa. The ideal case is presented when high velocity downdrafts and updrafts are uniformly distributed throughout the tank to guarantee an

efficient mixing.

Figure 3.3 shows the averaged vertical velocity maps generated by the sets of impellers in the X-Y plane for the axial-radial impellers (left column), the pitched blade turbines (middle column), and the Rushton turbines (right column) for single-phase (first row) and gassed (second row) conditions, respectively. The color scale shows the vertical velocity normalized by impeller tip velocity.

In general, as figure 3.3 (a) and 3.3 (c) shown, both the axial-radial impellers and Rushton turbines, respectively, are capable of inducing high downdrafts and updrafts, unlike the pitched blade turbines that just create high downdrafts. Besides, as can be seen in figures 3.3 (d), 3.3 (e), and 3.3 (f) this behavior intensifies when air is supplied. The high updrafts formed by the axial-radial impellers and Rushton turbines can be due to the radial jets that both sets of impellers produce. On the other hand, the vertical currents induced by the axial-radial impellers are larger in magnitude and extent than those created by the Rushton turbines, which leads to considering a more uniform flow distribution when using mixed-flow impellers.

Regarding the pitched blade turbines (figures 3.3 (b) and 3.3 (e)), because they are operated in the down-pumping mode, weak updrafts are observed as well as quasi stagnant regions close to the tank walls. Under these conditions, the potential use of these impellers in gas-liquid processes will be indeed a drawback because of the poor interaction of the flow discharged by these impellers with the rest of the tank.

To further analyze this behavior, figure 3.4 shows the vertical velocity profiles as a function of the radial distance at several vertical positions under ungassed and gassed conditions. These positions correspond to the location where the impellers have an immediate interaction with the surrounding fluid.

As shown in figures 3.4 (a), and 3.4 (d) the axial-radial impellers generate both updrafts and downdrafts. These currents are conveniently distributed in the horizontal direction, which would lead to obtaining a shorter mixing time. In the case of the pitched blade turbines (figure 3.4 (b), and figure 3.4 (e)), weak updrafts are noticed, which could increase the mixing time. On the other hand, as figure 3.4 (c), and figure 3.4 (f) shown, the Rushton turbines create quasi stagnant regions are formed between the vessel bottom and the lower turbine, which is a consequence mainly of the radial flow discharged by such impellers.

In general, the profiles present a tendency similar both in ungassed and gassed conditions, just the Rushton turbines have a important decrease in some positions.
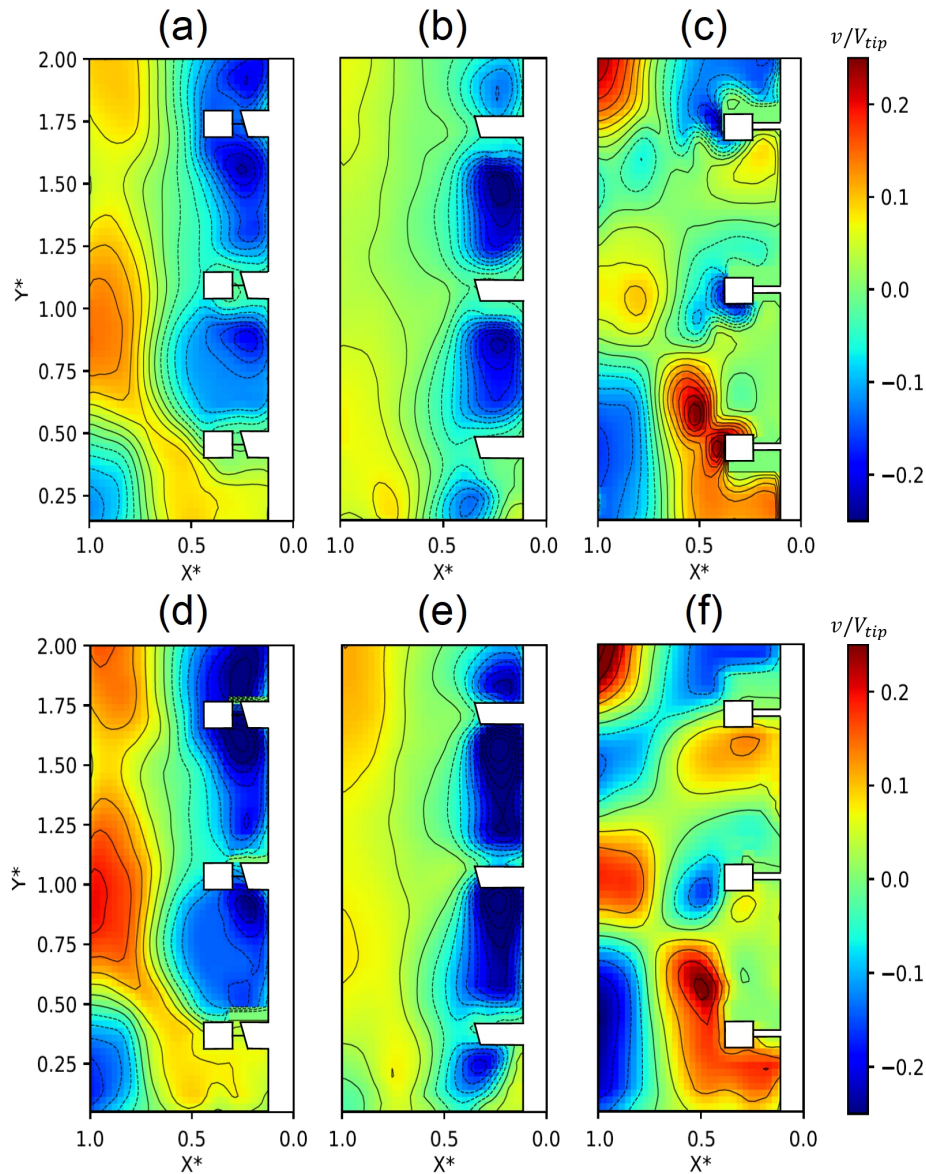
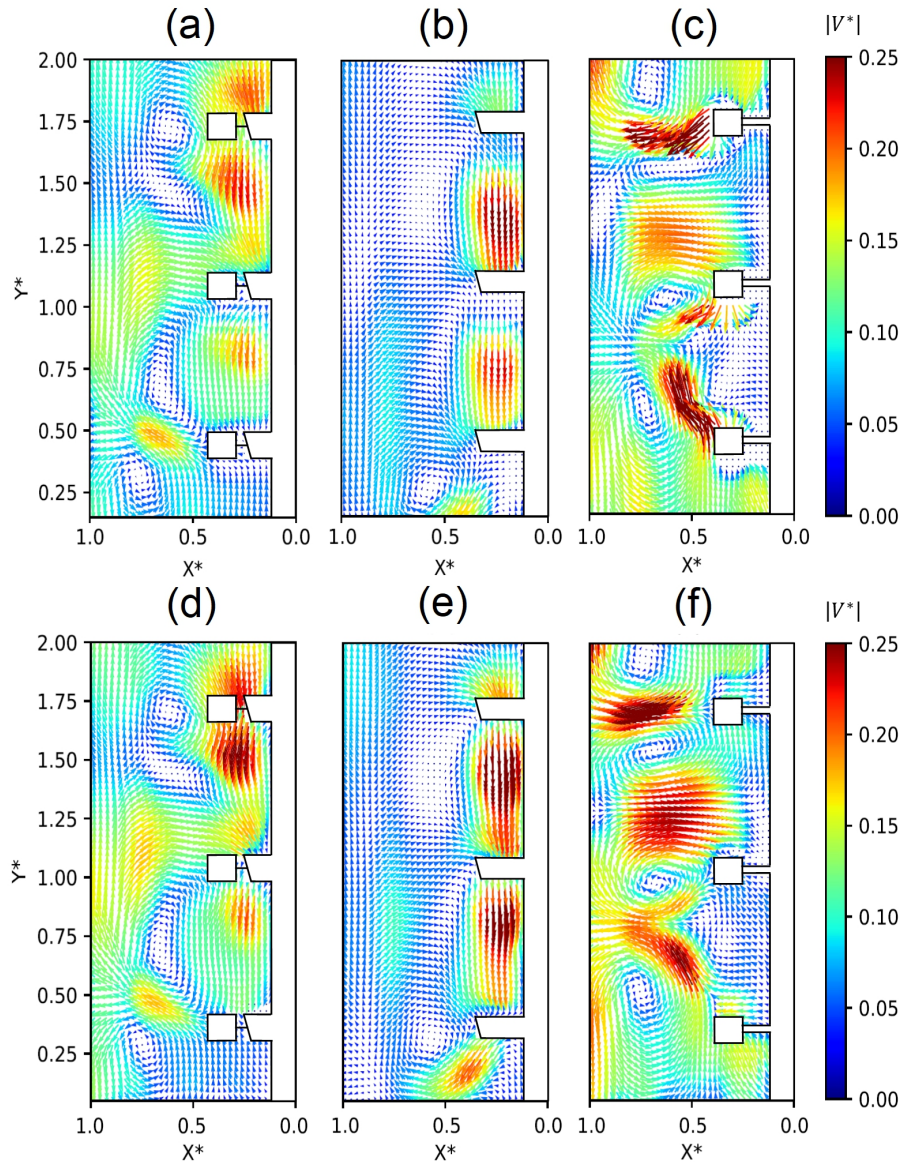Figure 3.3. Vertical velocity maps in the X–Y plane at $N = 400$ rpm for: axial-radial impellers: (a) single-phase, (d) 0.25 vvm; pitched blade turbines: (b) single-phase, (e) 0.25 vvm; Rushton turbines: (c) single-phase, (f) 0.25 vvm.

Both the vertical currents fields and profiles can give us information on mixing performance of the three sets of impellers investigated. It is clear, that due to better vertical currents distribution through the tank the axial-radial impellers will have a shorter mixing time followed by the Rushton turbines, and by last the pitched blade turbines. Although according to Ascanio et al. (2003) this tendency can change when it is used a non-Newtonian fluid.
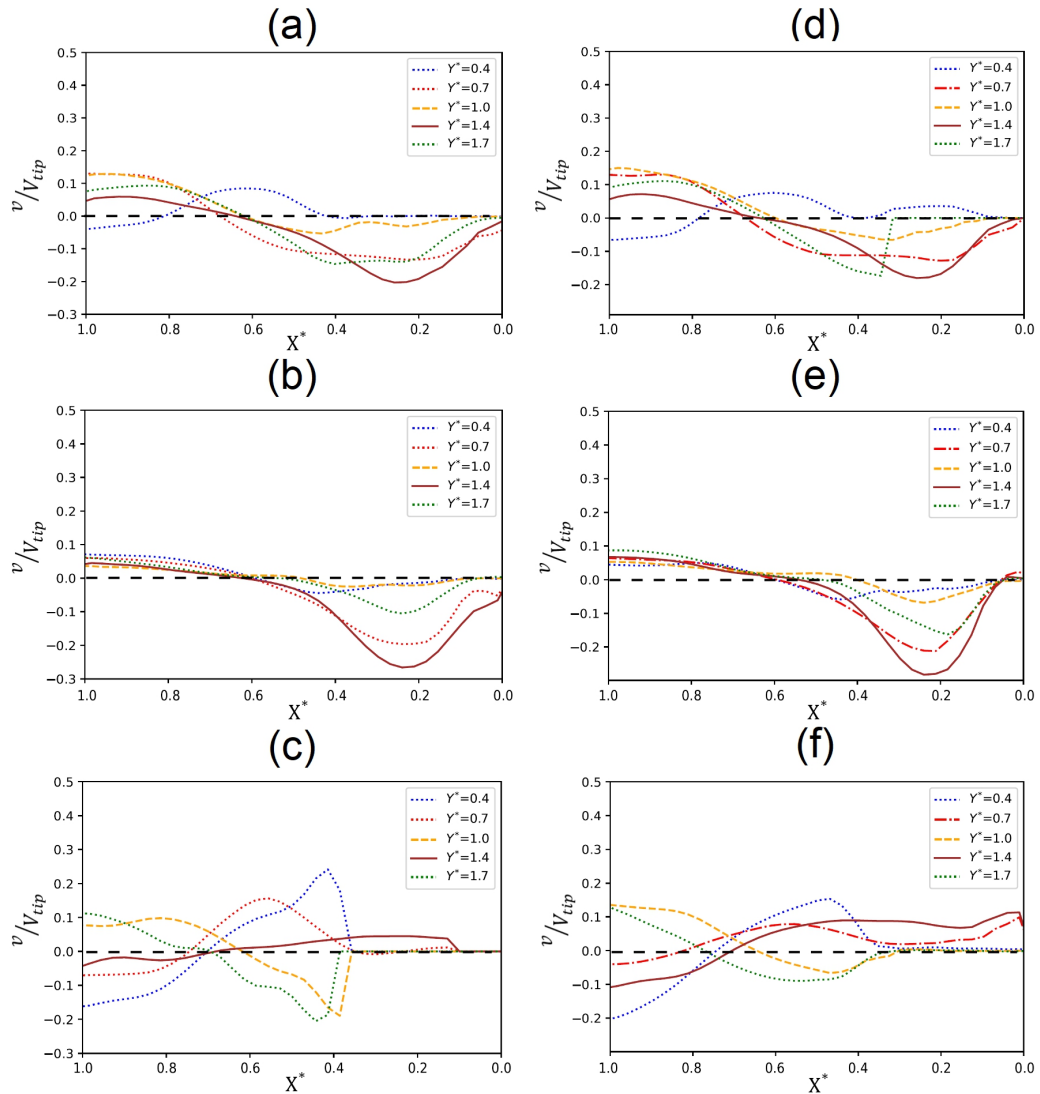
Figure 3.4. Vertical velocity profiles in the X–Y plane at $N = 400$ *rpm* for: axial-radial impellers: (a) single-phase, (d) 0.25 *vvm*; pitched blade turbines: (b) single-phase, (e) 0.25 *vvm*; Rushton turbines: (c) single-phase, (f) 0.25 *vvm*.

3.4   Turbulent intensity

Characterize the degree of agitation in mixing processes by means of the turbulent intensity is of great importance due to that this parameter is linked with the morphology of some biological models as mentioned earlier. In addition, this parameter to provides of qualitative manner the power consumption. Figure 3.5 shows the averaged turbulent intensity maps in the X-Y plane for the axial-radial impellers (left column), the pitched blade turbines (middle column), and the Rushton turbines (right column) for single-phase

(first row) and gassed (second row) conditions, respectively. The turbulent intensity is defined as the ratio of the average velocity fluctuations to a reference velocity. The turbulent intensity in the X-Y plane is calculated as follows:

$$TI = \frac{\sqrt{u'^2 + v'^2}}{V_{tip}} \tag{3.3}$$

where u'^2 and v'^2 are the fluid velocity fluctuations in the horizontal and vertical directions at each (X, Y) position, respectively, and V_{tip} is the impeller tip velocity. The color scale shows the turbulent intensity.

As figure 3.5 shows, as impellers rotate the fluid is accelerated when exiting the blades so that the highest velocity fluctuations are observed near the impellers' tip. When comparing the sets of impellers investigated under ungassed conditions (figures 3.5 (a), 3.5 (b), and 3.5 (c)), the highest values were obtained with the Rushton turbines followed by the pitched blade turbines and the axial-radial impellers, which coincides with the power characteristic curve (see figure 2.8). On the other hand, under gassed conditions, the tendency changed. The turbulent intensity maps are better distributed for the axial-radial impellers and the pitched blade turbines (figures 3.5 (d), 3.5 (e), respectively) when compared to the turbulent intensity maps of the Rushton turbines (figure 3.5 (f)). This occurred because both the axial-radial impellers and the pitched blade turbines were operated in the down-pumping mode, which causes a strong intersection of currents of both phases leading to large velocity gradients, which in turn cause an increase in the velocity fluctuations through the tank. On the other hand, the reduction of the turbulent intensity by part the Rushton turbines is due to have a better disperses of the bubbles.

Moreover, an important piece of information that the turbulent intensity maps provide is the capacity of the impellers to transfer energy to the fluid. In this sense, it would be reasonable to think that under gassed conditions more energy could be transferred to the fluid when using the axial-radial impellers, resulting in a more homogenous mixing compared with the other two sets of impellers. However, it is worth noting that such better energy transfer capacity will result in higher power demand when using mixed-flow impellers.

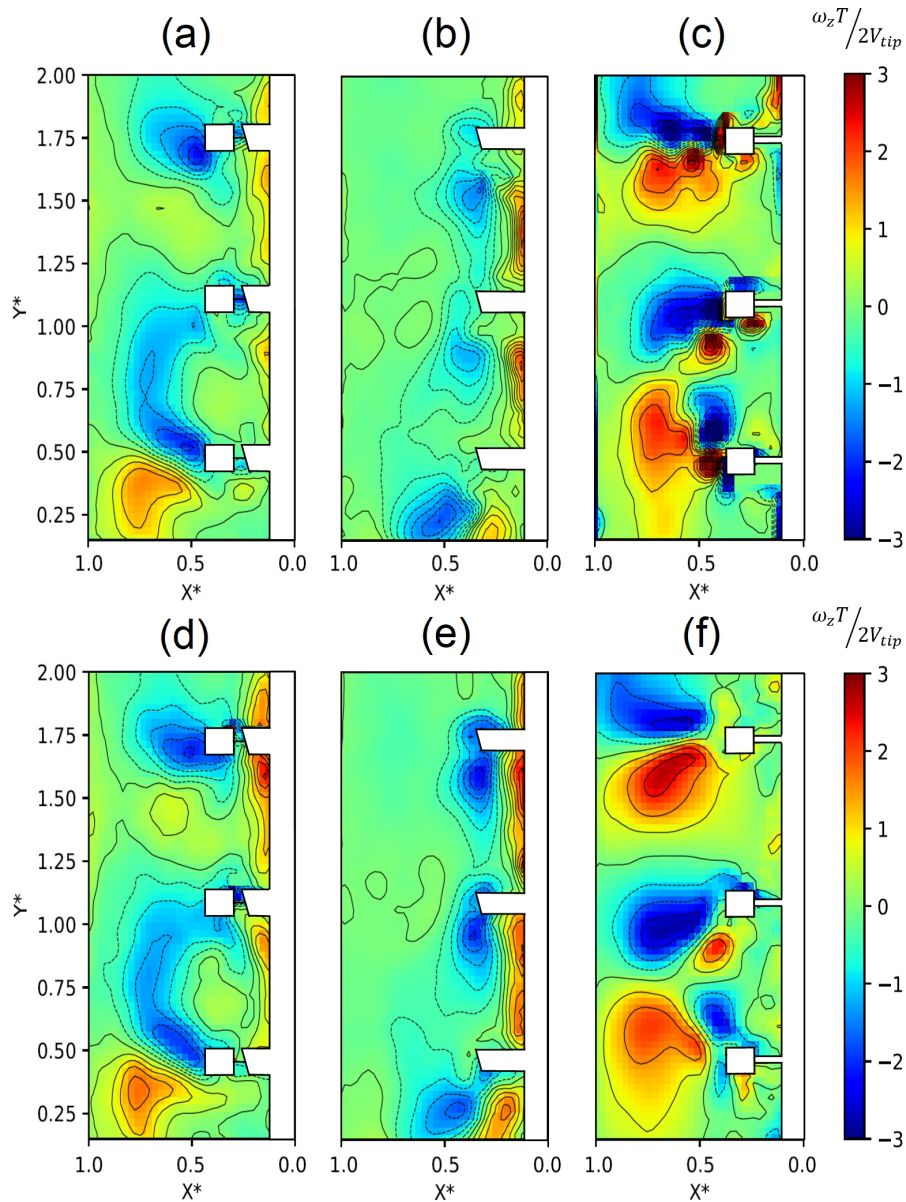Figure 3.5. Turbulent intensity maps in the X–Y plane at $N = 400$ rpm for: axial-radial impellers: (a) single-phase, (d) 0.25 vvm; pitched blade turbines: (b) single-phase, (e) 0.25 vvm; Rushton turbines: (c) single-phase, (f) 0.25 vvm.

3.5　Strain rates

Fluid dynamics play an important role in aerated stirred tanks processes. As impellers rotate, working fluids are subjected to strain rates, which become more relevant under the turbulent regime. The distribution of strain rates in the whole tank allows establishing whether the working fluid will be subjected to high shear forces.

Figure 3.6 shows the strain rates obtained in the X-Y plane for the axial-radial impellers (left column), the pitched blade turbines (middle column), and the Rushton turbines (right column) for single-phase (first row) and gassed (second row) conditions, respectively. The deformation rates in the X-Y plane was calculated as:

$$|\bar{S}| = \left[2 \left(\frac{\partial u}{\partial x} \right)^2 + 2 \left(\frac{\partial v}{\partial y} \right)^2 + \left(\frac{\partial u}{\partial y} + \frac{\partial v}{\partial x} \right)^2 \right]^{1/2} \tag{3.4}$$

where $|\bar{S}|$ is the modulus of strain rate tensor. The color scale shows the strain rates normalized by $2V_{tip}/T$.

As expected, the highest strain rates for all the impellers investigated were generated around the blades in both ungassed and gassed conditions. Moreover, both under ungassed and gassed conditions the highest values correspond to Rushton turbines followed by the axial-radial impellers, and the pitched blade turbines, which are strongly related to the velocity gradients created by each one of the sets of impellers as well the velocity magnitude of their vortexes. On the other hand, it is well known that bubbles are readily broken when subjected to high strain rates (Min et al. (2008), Kracht and Finch (2009)), which in this case will be reached easier when agitating with the Rushton turbines. As bubbles are broken, their size is reduced so that the contact surface of the bulk gas increases resulting in an improved mass transfer capacity.

On the other hand, the strain rates can be considered as a key parameter when selecting impellers for a particular biological model. Impellers generating high strain rates could be a drawback when working with shear-sensitive biological models (Nienow (2010), Verma et al. (2019)). Nevertheless, impellers that generate low shear rates can lead to insufficient cell division. In this sense, the axial-radial impellers would be an attractive alternative since they operate mainly in strain rates medium compared with the other two sets of impellers.
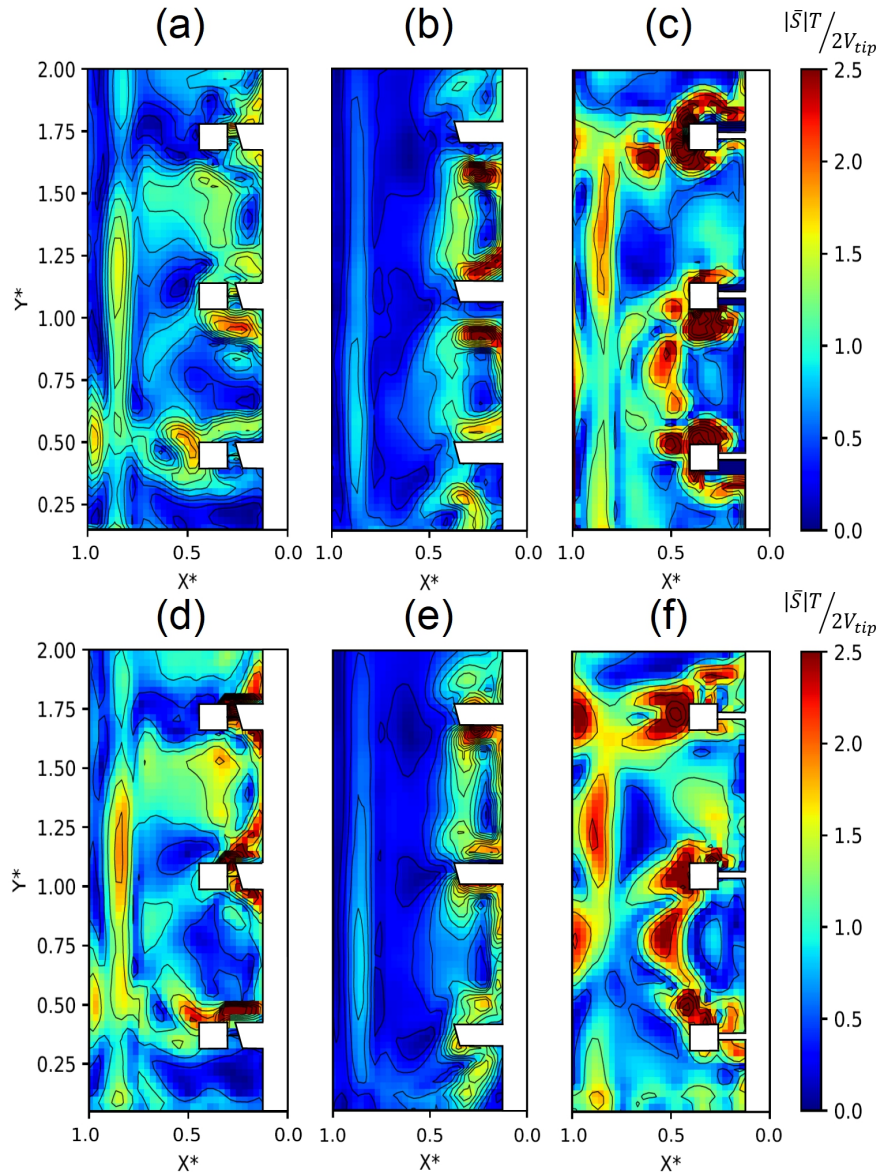
Figure 3.6. Strain rates maps in the X–Y plane at $N = 400$ rpm for: axial-radial impellers: (a) single-phase, (d) 0.25 vvm; pitched blade turbines: (b) single-phase, (e) 0.25 vvm; Rushton turbines: (c) single-phase, (f) 0.25 vvm.

3.6   Reynolds stresses

The shear Reynolds stress, $\overline{u'v'}$, are defined as the apparent stresses resulting from the turbulent velocity fluctuations. It indicates how the turbulence is transferred between two directions differently (horizontal and vertical in this case). Even, these stresses have been used for modeling numerically the turbulence in stirred tanks (Cheng et al. (2017),

Galletti et al. (2004)).

Figure 3.7 shows the shear Reynolds stresses obtained in the X-Y plane for the axial-radial impellers (left column), the pitched blade turbines (middle column), and the Rushton turbines (right column) for single-phase (first row) and gassed (second row) conditions, respectively. The shear Reynolds stresses (RS) in the X-Y plane were calculated as:

$$RS = \overline{u'v'} = \overline{uv} - \bar{u}\bar{v} \tag{3.5}$$

where, $\overline{uv}$, is the average of the product of the instantaneous velocities in the horizontal and vertical directions, while $\bar{u}$ and $\bar{v}$ are the average of the velocities in the horizontal and vertical directions, respectively. The color scale shows the shear Reynolds stresses normalized by V_{tip}^2.

Figure 3.7 (a) and 3.7 (d) shows the shear Reynolds stress maps for the axial-radial impellers under the ungassed and gassed conditions, respectively. Irrespective of the gassed conditions, the behavior is quite similar characterized by high-Reynolds stresses regions located close to the shaft and the tank wall. Shear Reynolds stresses are a little higher under gassed conditions, which is very likely a consequence of the turbulent intensity increase when supplying air. This behavior can be considered as the average of the ones obtained with radial discharge and axial flow impellers.

Regarding the pitched blade turbines, quite similar maps are observed under ungassed and gassed conditions (figure 3.7 (b) and 3.7 (e), respectively). This set of impellers creates a high-Reynolds stress region located under the lower turbine as well as low Reynolds stress regions close to all turbines. Because this type of impeller discharges the flow mainly in the axial direction, some quasi-stagnant regions appear close to the wall of the tank. Under gassed conditions, bubbles coming from the sparger are subjected to stress in regions close to the turbine blade only but the rest of them poorly interact so the behavior is identical under ungassed conditions.

Finally, figure 3.7 (c) shows the Reynolds stresses maps for the Rushton turbines under ungassed conditions. This set of impellers creates several high-Reynolds stress regions, which are concentrated mainly near to the impellers and in the corner of the tank. Similar behavior is observed when supplying air (figure 3.7 (f)); however, bigger regions having higher Reynolds stress values are generated.

In general, the Rushton turbines and axial-radial impellers create high turbulent structures, which implicates that these sets of impellers will have a better mixing performance. Regarding the pitched blade turbines, these sets of impellers create low turbulent struc-

tures which decrease their capacity to have an efficient mixing.

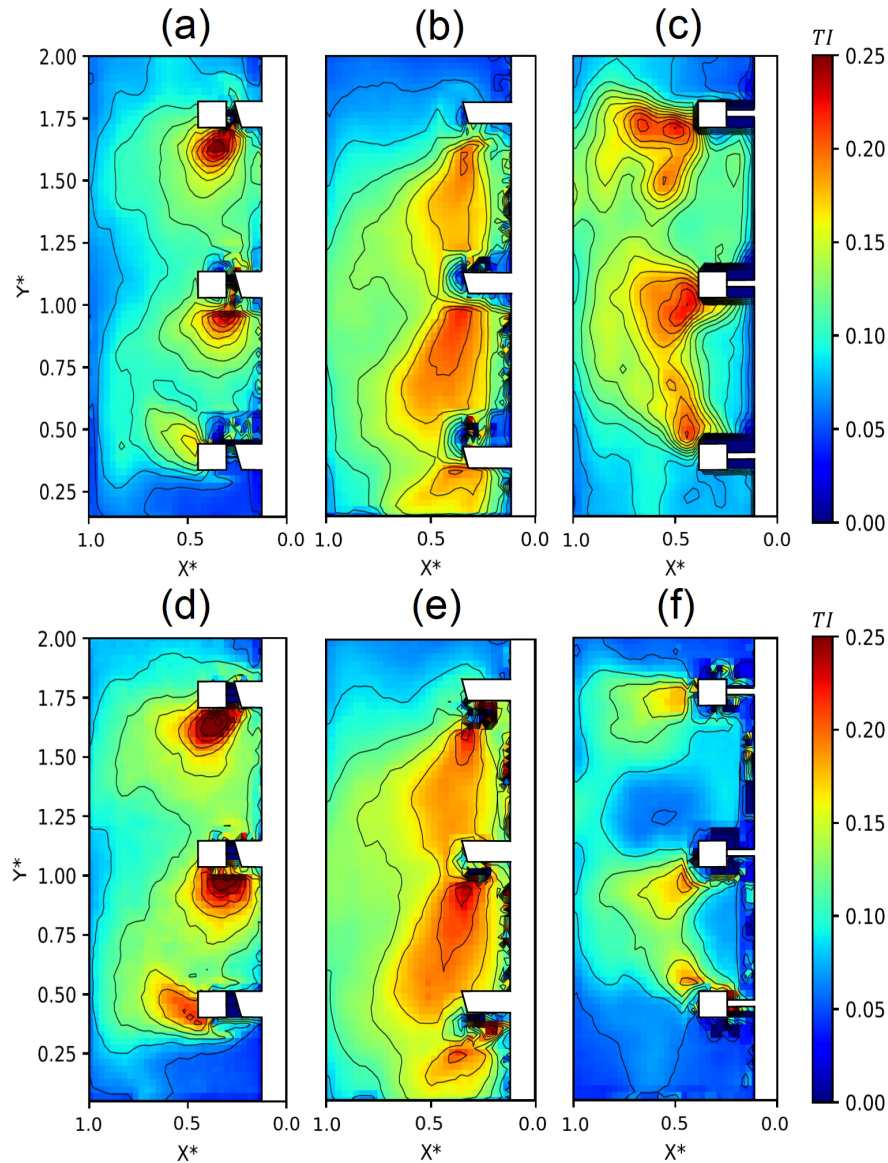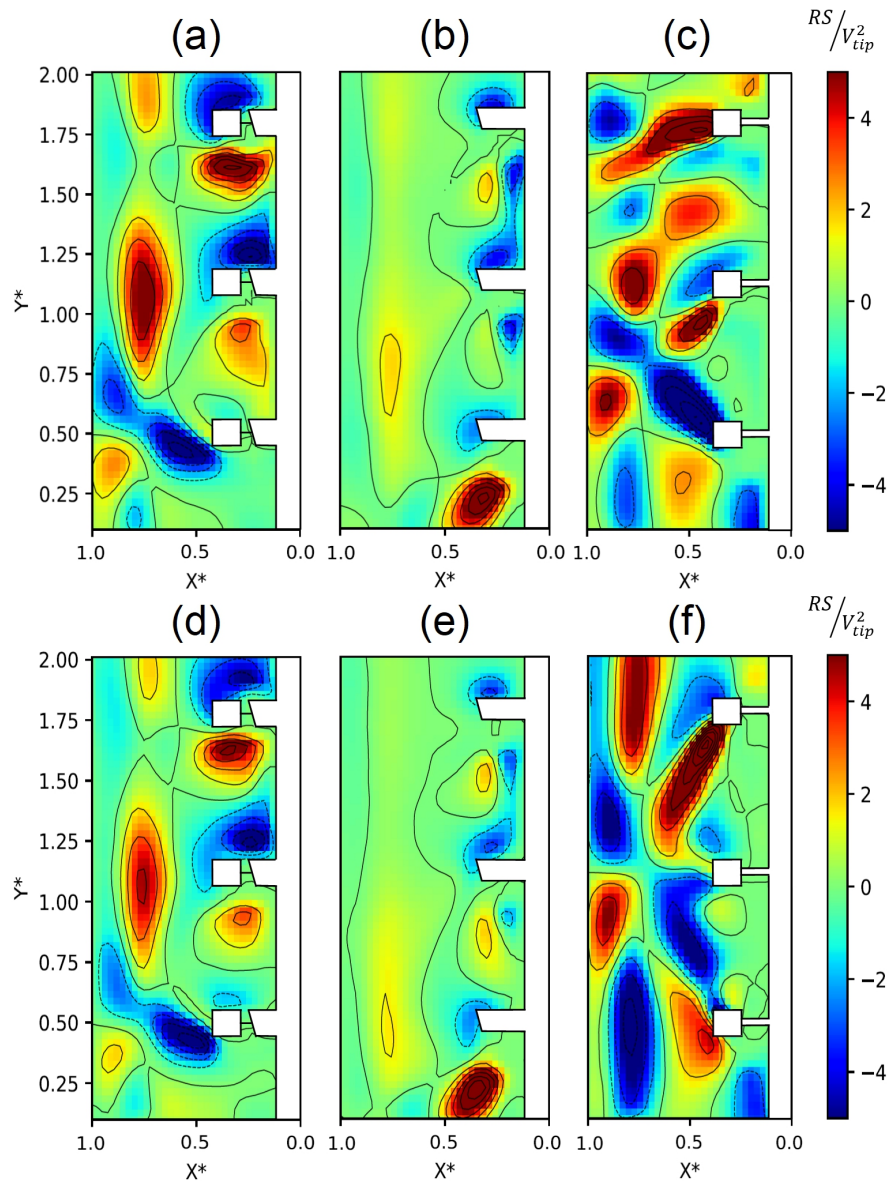Figure 3.7. Shear Reynolds stresses maps in the X–Y plane at $N = 400$ *rpm* for: axial-radial impellers: (a) single-phase, (d) 0.25 *vvm*; pitched blade turbines: (b) single-phase, (e) 0.25 *vvm*; Rushton turbines: (c) single-phase, (f) 0.25 *vvm*.

The results of the local parameters show that the mixed flow impellers achieved to eliminate the typical zones of static flow created by the impellers of axial and radial flow, which is reflected in better agitation intensity, better vertical pumping, and a good one generation of turbulent structures. Under these conditions, the axial-radial impellers will have major power consumption, minor mixing time, and a more homogenous product.

On the other hand, the Rushton turbines have high vorticity and high strain rates, which implicate a better gas hold-up and better mass transfer capacity. The results above are valid under a rotation velocity of 400 rpm and gassing rate of 0.25 vvm, but it is necessary to vary the gassing rates for analysis more complete due to the flow fields will change with the increase of airflow.

On the other hand, for performing a comprehensive assessment of the three sets of impellers used in this work, the global parameters such as power consumption, mass transfer capacity, gas hold-up, and pumping capacity were all evaluated. All these parameters were obtained as a function of the gassing rate. As mentioned in chapter 1, the particle image velocimetry technique is ineffective when working with high gassing rates due to the camera may capture the bubbles as tracer particles, which leads to an error in flow fields as is shown in figure 3.8. Then, for the analysis of local parameters at high gas flow rates, other techniques should be considered for example the electrical resistance tomography.
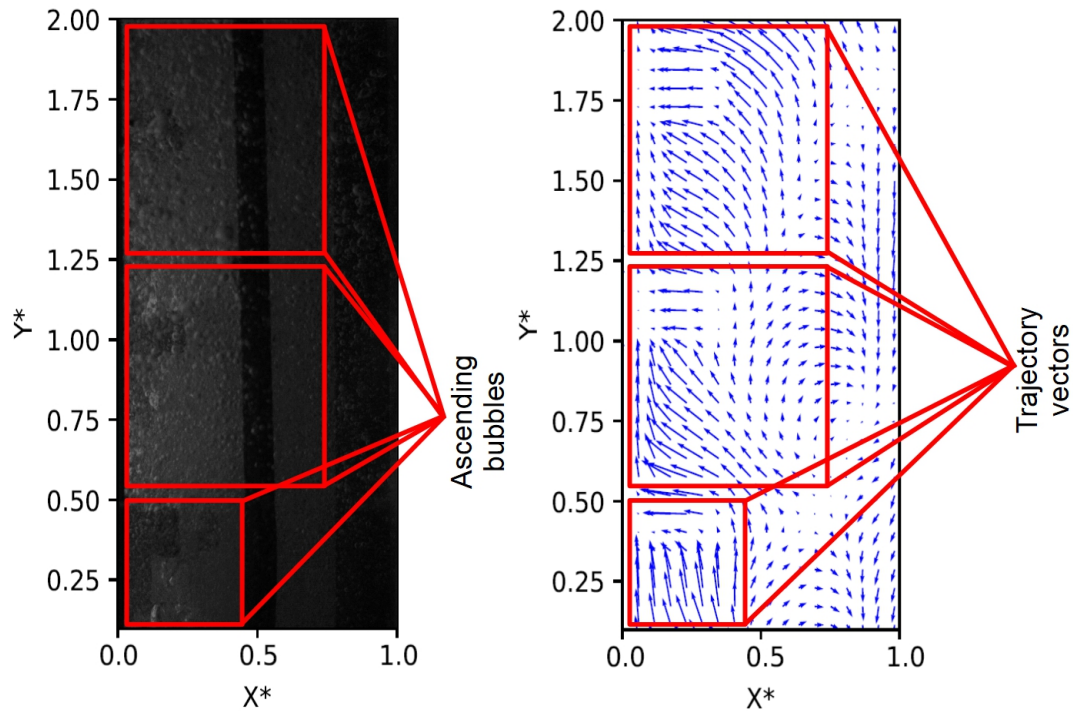
Figure 3.8. Erroneous flow fields in the X-Y plane at $N = 400$ rpm and 1 vvm for the axial-radial impellers.

The second part of the results shows the analysis of the global parameters of the three sets of impellers carried out through the evaluation of power consumption, mass transfer capacity, gas hold-up, and pumping capacity.

3.7   Power consumption

The power consumption is a key parameter in the design and scale-up of stirred tanks. This parameter indicates how the energy is transferred from the impellers to the fluid. Under ungassed and gassed conditions, the power consumption is evaluated with dimensionless numbers. Figure 3.9 shows the gassed power number (N_{pg}) as a function of gas flow number (Fl_g), which are defined by equations 2.4 and 2.5, respectively.

As expected, the power number decreases as the gas flow number increases; however, for Fl_g higher than 0.12, the power number remains practically constant, which indicates that the impellers begin flooding. In the case of the Rushton turbines, the power drops quickly as the gas flow number increases; however, once the power number remains constant, the Rushton turbines require less power compared with the other two impellers, which matches with the turbulent intensity maps for gassed phase. As reported elsewhere, this is due to the large cavities formed behind the blades and the higher frequency of bubble breakage (Derksen and Van Den Akker (1999), Kipke (1982), Ozcan-Taskin et al. (1992)). It is noticeable that the axial-radial impellers demand higher power as expected. In such impellers, straight blades are attached to pitched blades like winglets. As these impellers rotate, small cavities are formed behind the straight blades and more energy would be required for bubble breakage, which could explain the higher power demanded.

It is important to point out that experiments have been made with a low viscosity fluid. It is well known that impellers such as Rushton turbines exhibit high performance with such fluids. As air is supplied, the fluid bulk viscosity tends to decrease, and bubbles coming from the sparger will be subjected to higher shear rates. They will become smaller and better distributed in the tank, which can explain the good behavior of Rushton turbines. However, it is known that well-mixed regions or caverns can be created as the fluid viscosity increases and, under gassed conditions, flooding combined with caverns can be observed even for lower gas flow rates, so that the flow in such regions will poorly interact with the rest of tank. This leads to consider impellers capable of providing discharge flows in both directions delaying the appearance of flooding, such as hybrid impellers.

Figure 3.9. Power number as a function of gas flow number at $N = 400 \ rpm$ for: axial-radial impellers (ARIs), pitched blade turbines (PBTs), and Rushton turbines (RTs).

On the other hand, the power characteristics can be also analyzed in terms of the ratio of the gassed power to the ungassed power as depicted in figure 3.10. As this figure shows, a similar trend is observed, the power ratio decreases with increasing the gas flow number, and flooding is reached for gas flow numbers higher than 0.12. Once again, the power ratio for the Rushton turbines decreases abruptly with the flow number and, under turbulent regime conditions the power ratio is $^1/_4$ and $^1/_3$ compared to those of the axial-radial impellers and the pitched blade turbines, respectively. Rushton turbines exhibited the highest power ratio decrease followed by the axial-radial impellers and the pitched blade turbines. This is a consequence of the large cavities formed behind the blades, especially in impellers having straight blades. In general, in radial flow patterns, such as Rushton turbines, the frequency of bubble breakage is higher compared with impellers providing a different flow pattern (Khalili et al. (2017)). However, unlike figure 3.10, it is observed that hybrid impellers require less power compared to pitched blade turbines, which leads to state that the axial-radial impellers behave better under ungassed conditions.
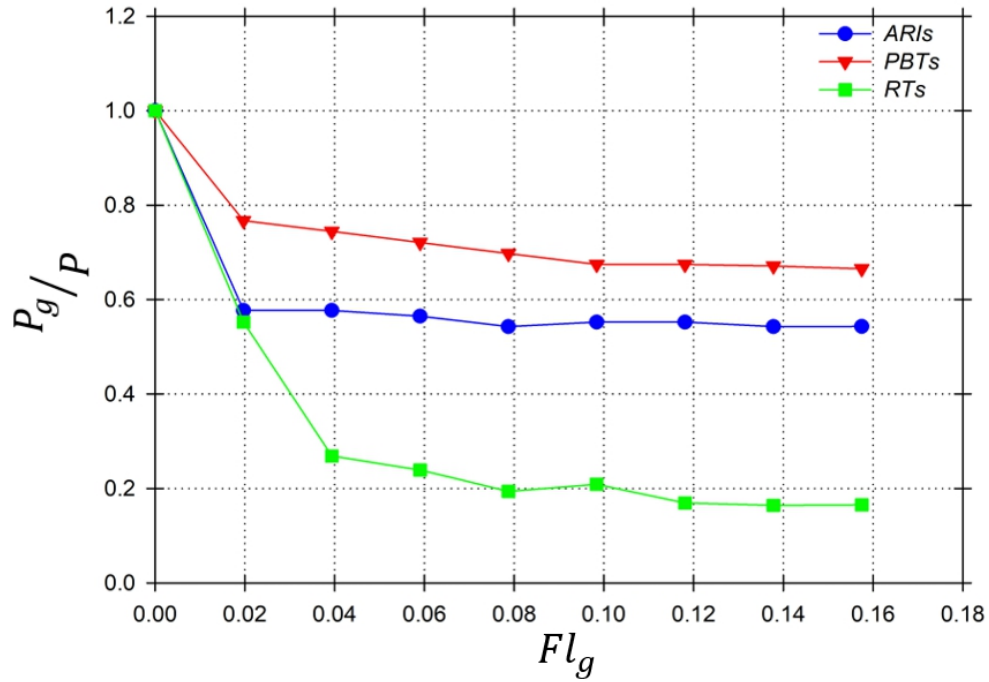
Figure 3.10. Power ratio as a function of gas flow number at $N = 400$ rpm for: axial-radial impellers (ARIs), pitched blade turbines (PBTs), and Rushton turbines (RTs).

Moreover, figure 3.11 shows a comparison of the experimental data of the power ratio obtained in this work with some correlations proposed by some authors. As it can be seen, the experimental data for pitched blade turbines and the axial-radial impellers agree with the correlations reported elsewhere (Paul et al. (2003)). In the case of Rushton turbines, the trend is quite similar; however, as observed, less power is required as increasing the gas flow rate.

On the other hand, figure 3.12 shows both the axial-radial impellers and the pitched blade turbines can decrease their power consumption when working in the upward-pumping mode; The reduction of the power consumption in this mode operating was 20 and 37 percent, respectively. Although this operation mode is not convenient especially when you are working on a gas-liquid system because the mass transfer capacity of the impellers decreases considerably.
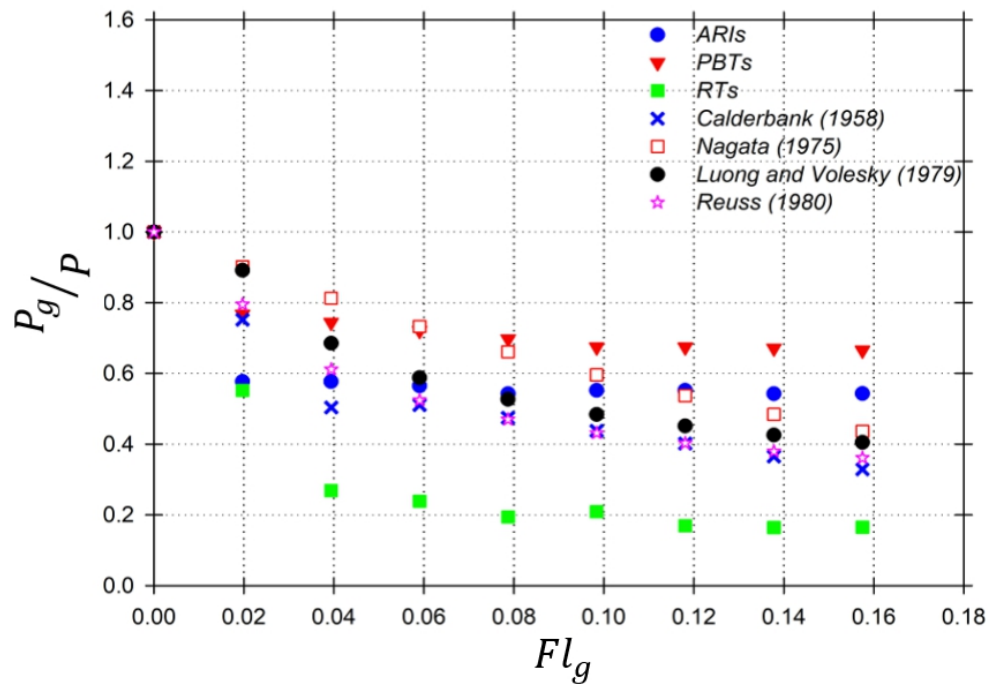
Figure 3.11. Comparison of the power ratio obtained in this work with some correlations reported in the literature.
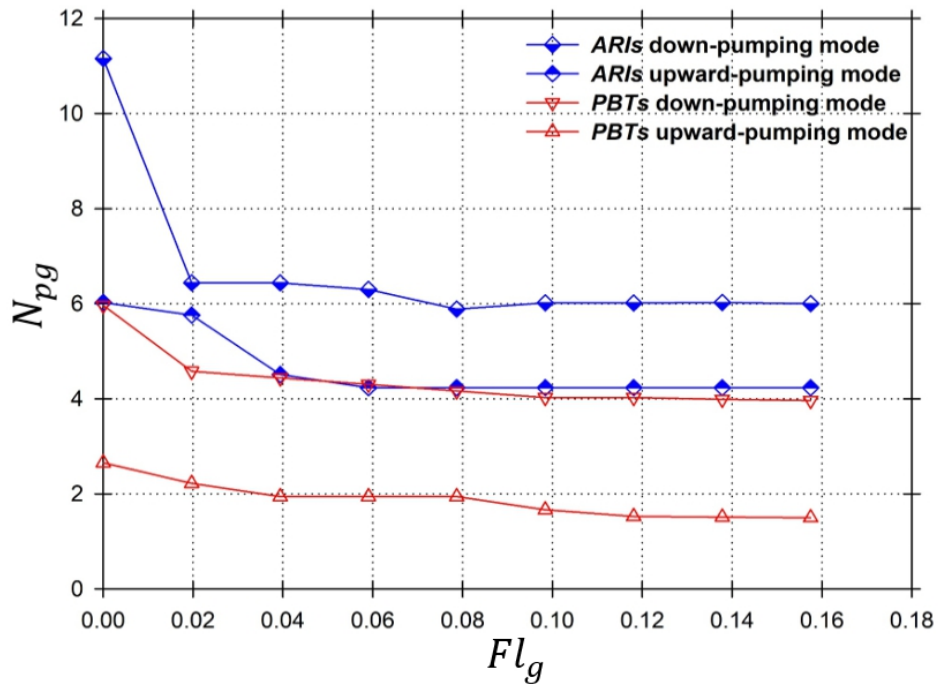
Figure 3.12. Power number as a function of gas flow number at $N = 400 \; rpm$ for: axial-radial impellers (ARIs), pitched blade turbines (PBTs) working so down and upward pumping mode.

3.8   Mass transfer capacity

As mentioned before, the mass transfer capacity of the impellers investigated was reported in terms of the volumetric mass transfer coefficient $K_L a$ as function of gas flow number (Fl_a). $K_L a$ indicates the rate of oxygen transferred to the medium, which is dependent on some parameters, namely: the impeller speed, impeller geometry, gas flow rate, number of impellers, number of blades and the fluid viscosity (Puthli et al. (2005b), Nocentini et al. (1993)).

Figure 3.13 shows the volumetric mass transfer coefficient for the impellers investigated as a function of the aeration rate in a Fl_g range from 0.02 to 0.16. As expected, $K_L a$ increases with increasing the aeration rate, although the mass transfer values are highly dependent on the impeller used.

As Figure 3.13 shows Rushton turbines exhibit the highest mass transfer capacity. As bubbles coming from the sparger are highly sheared, they reduce their size and they

are better distributed throughout the tank, which can explain due to the high strain rates generation that are created by the Rushton turbines. On the other hand, at low Fl_g numbers, the lowest coefficient is obtained with the pitched blade turbines; however, this mass transfer is improved as the gas flow rate is increased, and then the axial-radial impellers exhibit the lowest mass transfer capacity. However, it should be noted that the axial-radial impellers consist of four right-pitched blades only compared to both Rushton turbines and pitched blade turbines having six blades; this could explain the low shear stress to which bubbles are subjected when hybrid impellers are used.
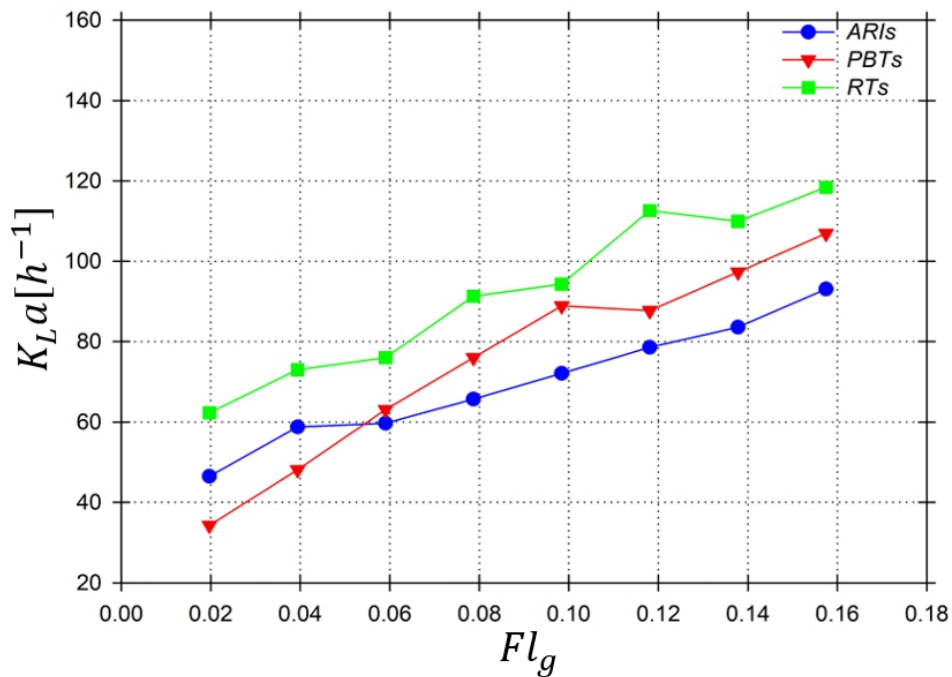
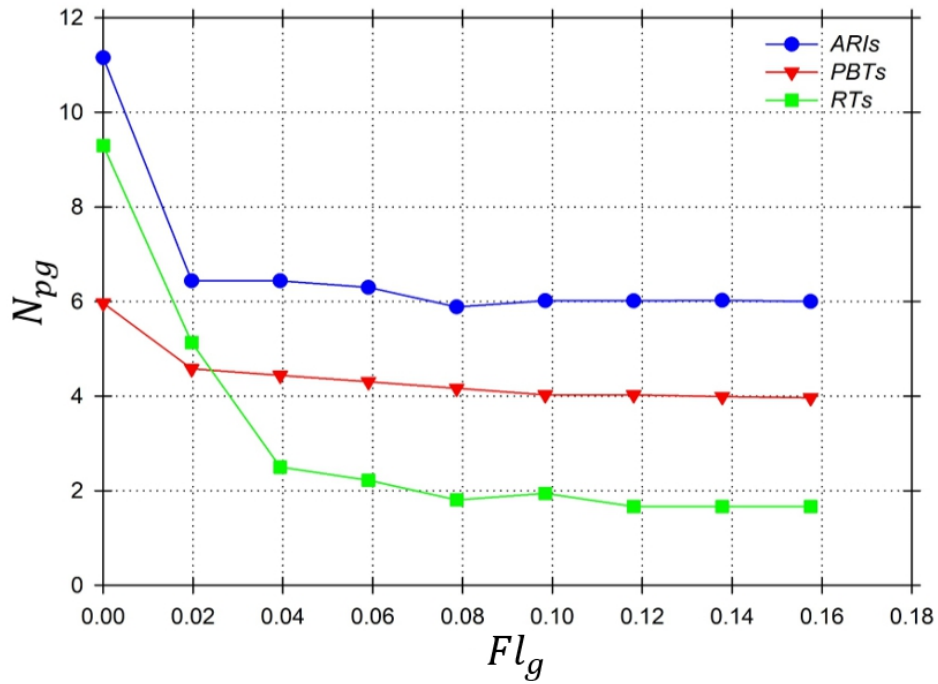Figure 3.13. Volumetric mass transfer coefficient as a function of gas flow number at $N = 400 \ rpm$ for: axial-radial impellers (ARIs), pitched blade turbines (PBTs), and Rushton turbines (RTs).

As aforementioned, an increase from 4 to 6 blades for the axial-radial impellers could improve their mass transfer capacity. On the other hand, as is depicted in figure 3.14 when the viscosity of the fluid increases, the mass transfer capacity of the three sets of impellers decreases. Particularly, the mass transfer capacity of the Rushton turbines decreases considerably. Conversely, the performance of the axial-radial impellers increases reflecting a mass transfer capacity very similar to that shown by the Rushton turbines, which indicates that the axial-radial impellers can be an attractive alternative in the

fermentation process where the viscosity of the culture broth increases with time.
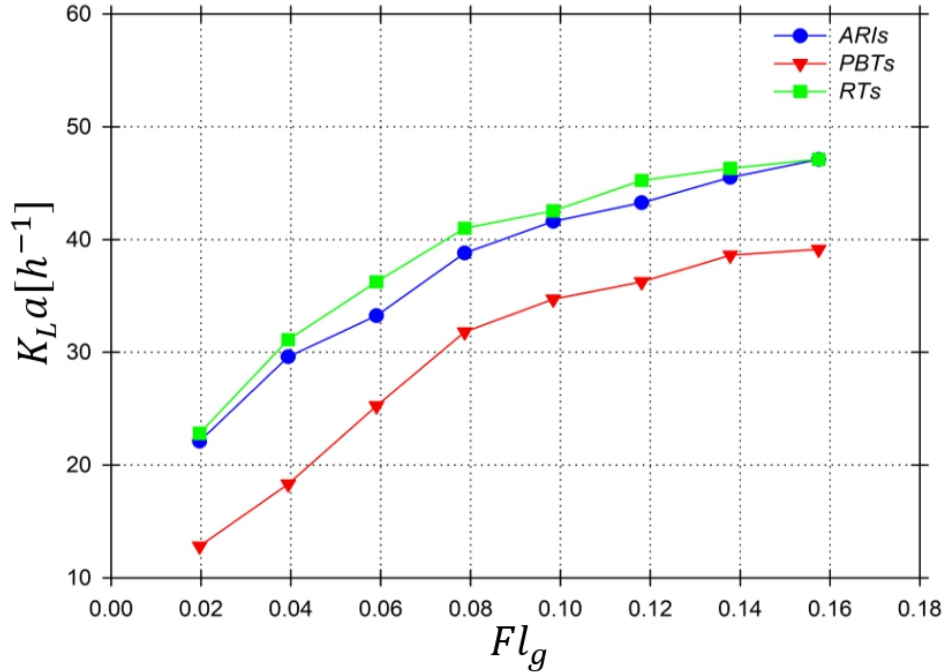
Figure 3.14. Volumetric mass transfer coefficient as a function of gas flow number at $N = 400$ rpm for a solution of sodium alginate dissolved in distilled water at a concentration of 3 g/l resulting in a dynamic viscosity of 12.5 $mPa \cdot s$ for: axial-radial impellers (ARIs), pitched blade turbines (PBTs), and Rushton turbines (RTs).

3.9   Overall gas hold-up

The overall gas hold-up indicates the residence time of the bubbles in the liquid medium so that to have high gas hold-up values is ideal for the main application of the gas-liquid system as the fermentation processes. Figure 3.15 shows the gas hold-up for the three sets of impellers investigated. As expected, the overall gas hold-up increases with the increase of gas flow number. This occurs due to a larger gas flow rate results in more bubbles. As a consequence of the above-mentioned, the increase in the number of bubbles leads to a greater possibility of bubble coalescence, which results in an increase in bubble size. The large bubbles overflow the stirred tank faster than small bubbles, which is not conducive to a further improvement of the gas hold-up. So, we can say that the rising rate of the gas hold-up decreases when increasing of gas flow number and after a certain gas flow number it will remain constant.

On the other hand, it can be seen in figure 3.15 that the gas hold-up of the three impeller sets is very close at low gas flow numbers probably due to the that the gas in the stirred tank is completely dispersed by the three impeller sets at low gas flow numbers. Clearly, we can see that for gas flow numbers higher than 0.08, the Rushton turbines have the highest gas hold-up while the pitched blade turbines and the axial-radial impellers behave quite similar for Fl_g between 0.06 and 0.14; however, the gas hold-up for the pitched blade turbines increases for Fl_g higher than 0.14. The Rushton turbines have a larger circulation flow and a more uniform dispersion of the gas because these sets of impellers create high vorticity structures. For these reasons, the overall gas hold-up of Rushton turbines is higher than that of the other two impeller sets which indicates that the Rushton turbines have a sweeping area that is larger compared to the other two sets of impellers.
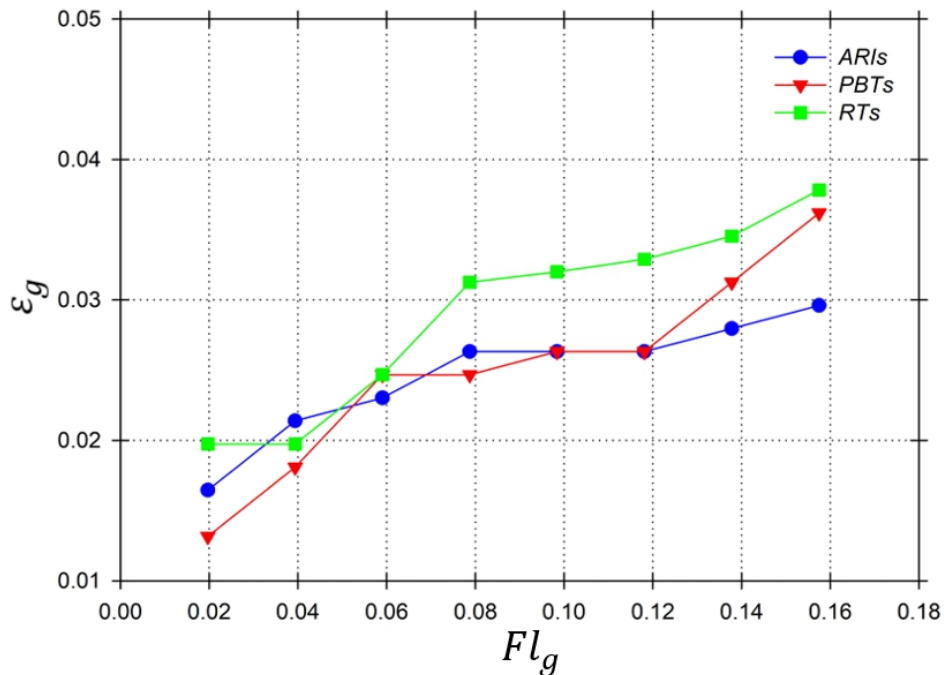
Figure 3.15. Gas hold-up as a function of gas flow number at $N = 400\ rpm$ for: axial-radial impellers (ARIs), pitched blade turbines (PBTs), and Rushton turbines (RTs).

In general terms, the best performance in terms of the gas hold-up is obtained with Rushton turbines. However, looking at figure 3.15, for Fl_g numbers ranging from 0.04 to 0.06, a small difference is observed when comparing the three sets of impeller's performance. On the other hand, although the experiments were for a maximum Fl_g of

0.16, looking at figure 3.15, one could think that better results would be obtained when increasing the gas flow rate.

3.10   Pumping capacity

Finally, to complement the global analysis, it is important to quantify the amount of fluid pumped by the three sets of impellers. The mixing will be promoted by the flow pushed by the impellers. An important parameter to characterize these currents is the pumping capacity. This parameter was quantified with equations 2.8, 2.9, and 2.10. The results were reported in dimensionless form (equation 2.11) by means of the pumping number.

Figure 3.16 shows the cross-sections in which the pumping number was determined. In this case, due to different flow patterns investigated three sections for computing the pumping capacity were selected. The choice of these sections was made with the purpose of obtaining the most representative mass transport flux sections for the three sets of impellers used in this work. The mean amount of the fluid displaced by the sets of impellers in both horizontal and vertical directions was calculated.

Table 1 summarizes the values of the horizontal and vertical pumping as well as the total pumping number under ungassed and gassed conditions. For all sets of impellers analyzed in this work, the pumping was strongly affected by the presence of bubbles. Furthermore, the measurements of the total pumping capacity under gassed conditions was mainly defined by the horizontal contribution. In contrast, for the single-phase condition, both components were quite similar. Finally, both under gassed and ungassed conditions, the axial-radial impellers achieved a better performance as a consequence of the combination of the tilted and straight paddles.

Finally, it is clear that the Rushton turbines have the least pumping number in both ungassed and gassed conditions. Their low performance is due to its high radial discharge, which provokes a strong static flow close to the shaft, and low vertical pumping as was mentioned before.
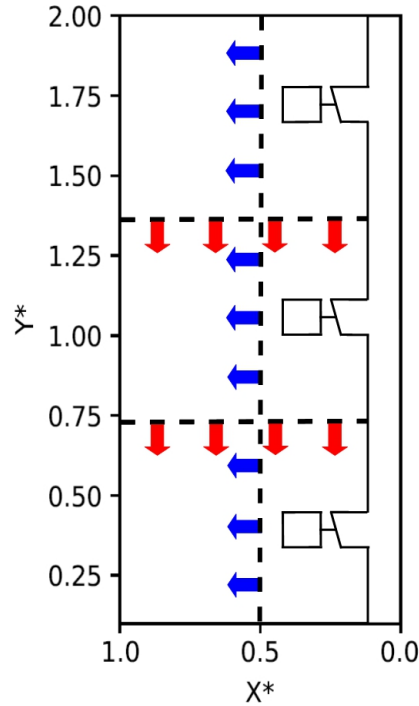
Figure 3.16. Cross-sections in which the pumping number was determined for each set of impellers used in this work.

Table 3.1. Pumping number and pumping capacities in the horizontal and vertical directions for the three sets of the impellers under ungassed and gassed conditions.

Impeller	Q_x [$\times 10^{-4}$ m^3/s]	Q_y [$\times 10^{-4}$ m^3/s]	Q_T [$\times 10^{-4}$ m^3/s]	N_q [$-$]
Ungassed				
ARIs	8.5068	5.4649	13.9717	0.83
PBTs	4.6131	8.9698	13.5819	0.81
RTs	8.9893	3.1124	12.1017	0.72
0.25 vvm				
ARIs	14.1933	2.3799	16.5732	0.99
PBTs	12.8764	2.3799	15.2563	0.95
RTs	11.8352	2.8570	14.6923	0.88

Overall, from a global standpoint, Rushton turbines were the most efficient impellers. Radial flow generated by this set of impellers creates high-velocity zones while promoting fluid rotation. This induces breakage of bubbles emerging from the sparger, which increases the contact surface, so that a higher mass transfer coefficient and a better gas hold-up is obtained as a result of a better distribution of smaller bubbles in the liquid phase at a reduced power drawn. However, these impellers will decrease their performance

as the fluid viscosity increases.

The pitched blade turbines create stagnant zones mainly above the sparger when operated in the down-pumping mode. Under such conditions, the liquid is pushed towards the bottom of the tank. During the travel, the liquid encounters the bubbles emerging from the sparger resulting in motionless regions. On the other hand, the highest velocity regions when using the pitched blade turbines are created close to the shaft. As consequence, the oxygen is poorly dispersed in the tank, so its performance in terms of the mass transfer capacity is diminished. Nonetheless, the high axial discharge causes a medium demand for power and a pumping capacity very close to the shown by the axial-radial impellers.

Regarding the axial-radial impellers, their hybrid geometry provokes then the flow created by the tilted paddles to push the liquid towards the bottom of the tank. Although the straight paddles discharge the flow in the radial direction, poor interaction between the currents created by the tilted and straight paddles results in limited mass transfer capacity and the highest power consumption. The power drawn can be reduced when rotating the impellers counter-clockwise, so that the air bubbles will be accelerated towards the free surface. However, very likely, a lower mass transfer coefficient will be obtained under such conditions. The axial-radial impellers will have a better mass transfer capacity and better gas hold-up in fluid with high viscosity. On the other hand, an increase from 4 to 6 hybrid blades will cause an improvement in their mass transfer capacity, gas hold-up, and their pumping capacity.

Conclusions

In the present work, an experimental study has been conducted with the aim of assessing an aerated stirred tank equipped with multiple impellers under ungassed and gassed conditions. For that purpose, impellers providing different flow discharges, namely; radial, axial, and mixed flow impellers were investigated. Results are presented in terms of local parameters and global parameters.

Results local parameters showed that the mixed flow impellers under the conditions investigated exhibit a better performance compared with the other two sets of impellers. The combination of tilted and straight blades of the mixed-flow promotes the removal of classic quasi-static flow zones created by the radial and axial flow impellers, shorter better vertical pumping, and better agitation intensity, which involves a shorter mixing time and products more homogenous. On the other hand, the global parameters at high gassing rates showed that impellers discharging mainly in the radial direction exhibited the best global performance in terms of the mass transfer capacity at low power consumption and better gas hold-up. Although, when the three sets of impellers working with low gassing rates have performance very similar. Moreover, the results can be inferred the mixed flow impellers can increase their performance by increasing their blades number or when the viscosity of work fluid increase.

Finally, the results obtained show the relations between the local and global parameters. The vorticity, turbulent intensity, strain rates, and vertical currents can be linked with the global parameters such as gas hold-up, power consumption, mass transfer capacity, and mixing times, respectively.

Appendix A
Articles in Conferences

Dear David Israel Posadas Navarro,

The program committee of the 16th European Conference on Mixing (Mixing 16) is pleased to announce you that your abstract here below has been accepted.

CONTRIBUTION DETAILS

ID: 172
Title: Flow Patterns in a Double Planetary Mixer with the Technique of PIV

The scientific committee is now evaluating your abstract in order to make a selection of oral presentations. You will be informed of the presentation type (oral or poster presentation) of your abstract at the beginning of June.

In the meantime, we invite you to register for the conference on the website www.mixing16.eu Early-bird registration is until 9th July. Note that both poster and oral presentations will only appear in the scientific program if at least one author is registered to attend the conference.

Thank you for your contribution and we look forward to seeing you in Toulouse in September.

Best regards

For the scientific committee

Flow Fields Generated in a Double Planetary Mixer

D. Posadas-Navarro[1], G. Ascanio[2], M. Salinas-Vazquez[3], J. Ramirez-Cruz[4],
C. Palacios-Morales[5]

[1] Instituo de Ingeniería, Universidad Nacional Autónoma de México, Circuito Escolar, Ciudad Universitaria, 04510, Ciudad de México, México, dposadasn@iingen.unam.mx
[2] Instituto de Ciencias Aplicadas y Tecnología, Universidad Nacional Autónoma de México, Circuito Escolar, Ciudad Universitaria, 04510, Ciudad de México, México, gabriel.ascanio@ccadet.unam.mx
[3] Instituo de Ingeniería, Universidad Nacional Autónoma de México, Circuito Escolar, Ciudad Universitaria, 04510, Ciudad de México, México, msalinasv@iingen.unam.mx
[4] Instituo de Ingeniería, Universidad Nacional Autónoma de México, Circuito Escolar, Ciudad Universitaria, 04510, Ciudad de México, México, jramirezcr@iingen.unam.mx
[5] Facultad de Ingeniería, Universidad Nacional Autónoma de México, Circuito Escolar, Ciudad Universitaria, 04510, Ciudad de México, México, cpalacios@unam.mx

Abstract: Planetary mixers are frequently used for the mixing of high viscous and viscoelastic media in some industries. In the present work, an experimental study of the flow patterns generated by the impellers through the PIV technique in a double planetary mixer with glycerin as working fluid was carried out. Results allow visualizing the velocity fields, which in turn allow to calculate other important properties to improve the mixing, namely: vorticity, shear stress, etc. These studies are not frequently reported in the literature for planetary mixers, so they are very useful for the validation of CFD studies.
Keywords: Planetary Mixer, Flow Patterns, PIV, Vorticity Fields, Velocity Fields.

Introduction

Mixing is one of the unit operations of chemical engineering more difficult to submit to a scientific analysis. The aim of this operation is become a fluid more uniform, eliminating gradients of concentration, temperature and other properties. Therefore we can mention the following about mixing:

- The main objective of mixing is to achieve a homogeneous fluid with respect to one or several variables of interest.
- The variables of interest are determined by the process performed as well as the requirements of it. Some of these variables are temperature, concentration, density, time, among others.
- The mixing can be carried out with different states of matter, having mixtures in miscible phases (liquid-liquid, gas-gas, or solid-solid) or non-miscible phase (solid-liquid, liquid-gas, solid-gas, etc.)

Mixing of highly viscous fluids is a common operation in the chemical, pharmaceutical, biochemical, and food industries. Twin-blade planetary mixer, which provides a suitable bulk circulation and good homogenization for highly viscous materials and pastes is an important equipment for the industry today. In recent years, different mixing systems have been developed for agitation of non-Newtonian or Newtonian fluids, but the efficient mixing remains a difficult task, as does the design and scale-up of reactors for processing of highly viscous fluids.

The hydrodynamics of planetary mixers has been investigated in recent years, being the numerical simulations the most used approach. Tanguy et al. [1] performed a simulation of a double planetary mixer using a cross-linking reaction; such simulations despised shear stresses, resulting in low accurate flow fields predictions.

Experimentally, Zhou et al [2] reported power drawn of a planetary mixer with non-Newtonian and viscoelastic fluids, which were rheologically characterized. Also Clifford et al [3] reported the effect of the Reynolds number on the hydrodynamics of a simple planetary mixer with Newtonian fluids.

Delaplace et al [4] conducted a dimensionless analysis, which was used to verify that the power and Reynolds numbers are excellent for comparing the power drawn of a planetary mixer with a conventional mixer. Delaplace et al [5] introduced concept of mixing time as a comparison parameter to determine the mixing efficiency of a planetary mixer with respect to a conventional one. Andre et al

[6] proposed to generalize some dimensionless numbers, which substitute already known numbers such as mixing time and power used for the description of conventional mixers.

Jian et al [7] investigated numerically the effects of power consumption as a function of the geometric parameters (blade- blade clearance and helical angle) and two different rotating modes (counter-rotating mode and co-rotating mode). Results indicated that decreasing the blade-blade clearance or increasing the helical angle increases, the power drawn by a twin-blade planetary mixer tends to decrease. When the Newtonian fluids are placed inside the mixer, the power consumption or the proportionality constant seems to have no difference under the counter-rotating and co-rotating modes. Finally, as the blade-blade clearance decrease or increase, the helical angle increases the value of proportionality constant.

Methodology
Description of the Double Planetary Mixer
Figure 1 shows the mixer used in this work, which consists mainly of a gearmotor of 1/4 hp at 42 rpm, 90 VDC, connected to a torque sensor (Futek model TRS300 type FRH01987) having a maximum capacity of 10 N·m, maximum axial force of 150 N, maximum radial force of 20 N and a weight of 0.5 kg. Two identical anchors impellers of 177.8 mm by 55.8 mm, having a ratio of speeds between the gearmotor and the impellers of 5/3 were used for fluid mixing. The stirred vessel is a cylinder made of glass 190 mm inside diameter and a height of 240 mm made of glass. The vessel is placed inside a square jacket made of acrylic of 32 cm x 32 cm and 30 cm, width, length and height, respectively. Both the and the jacket are supported by a structure, which allow the height to be varied for visualization experiments.
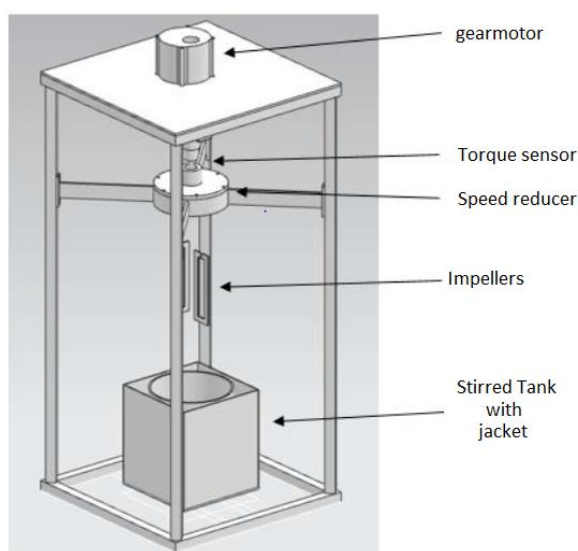
Figure 2 Composition of the planetary mixer

Working Fluid
Tests were made with aqueous solutions of glycerin at different concentrations. Table 1 shows the viscosity and density values of glycerin at different concentrations.

Table 1 Viscosity and density of the Glycerin with different concentrations

Concentration % w/w	μ [Pa·s]	ρ [kg/m³]
100	0.777	1259.46
95	0.323	1250.60
90	0.162	1240.73
85	0.084	1225.26
80	0.049	1206.80

The Technique PIV

Figure 2 shows the experimental setup used for visualization experiments by using the Particle image velocimetry (PIV), which is an indirect measurement technique that allows measuring the velocity field of a fluid. It consists of illuminating the area of interest seeded with tracer particles, by means of a thin light sheet and taking a couple of images at a known time interval. The velocity vectors are calculated by dividing the images into small interrogation areas in which a cross-correlation is applied to determine the displacement of the particles, as the time between the images is known, Δt, the calculation of the velocity of each particle it is done by means of the equation,

$$v_p = \frac{d(t_1) - d(t_2)}{\Delta t}$$

where $d(t_1), d(t_2)$ are the positions of the particle at times one and two, respectively.
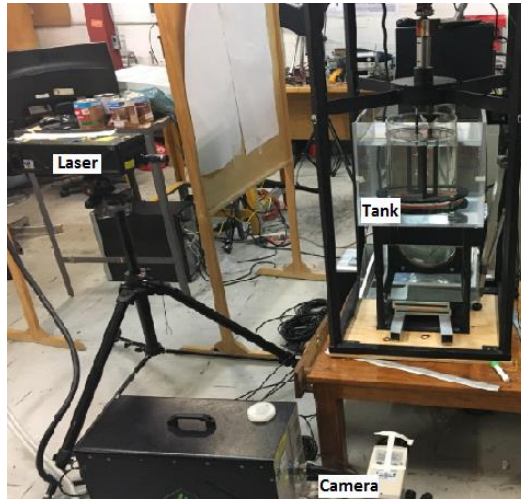
Figure 3 Experimental setup for visualization experiments.

The 2-dimensional PIV system consists of a HiSense Mkll high-speed camera, an EverGreen laser of the Quantel brand and glass spheres coated with silver as tracer particles.

Results

Figure 3 shows the vorticity fields obtained at anchor velocities of 10, 20 and 30 rpm. They were obtained at two different planes at distances of 36 mm and 92 mm measured from the vessel bottom. Here, the azimuthal component of the vorticity field can be obtained calculating the curl of the r-z vector field:

$$\omega_\theta = \frac{\partial V_r}{\partial z} - \frac{\partial V_z}{\partial r}$$

The vorticity indicates the rate of fluid rotation and large vortices show the regions in which the vortexing is important. Positive or negative signs indicate only the fluid rotation, clockwise or counterclockwise, respectively.

For comparison purposes, vorticity fields were obtained with the anchors at the same angular position for the rotational speeds investigated. Al low speed, large vorticity regions are observed in the lower plane; however, as the anchor speed in increased vortexing in more noticeable in the upper plane. This leads to think that pumping in the planetary mixer is improved when increasing the rotational speed.
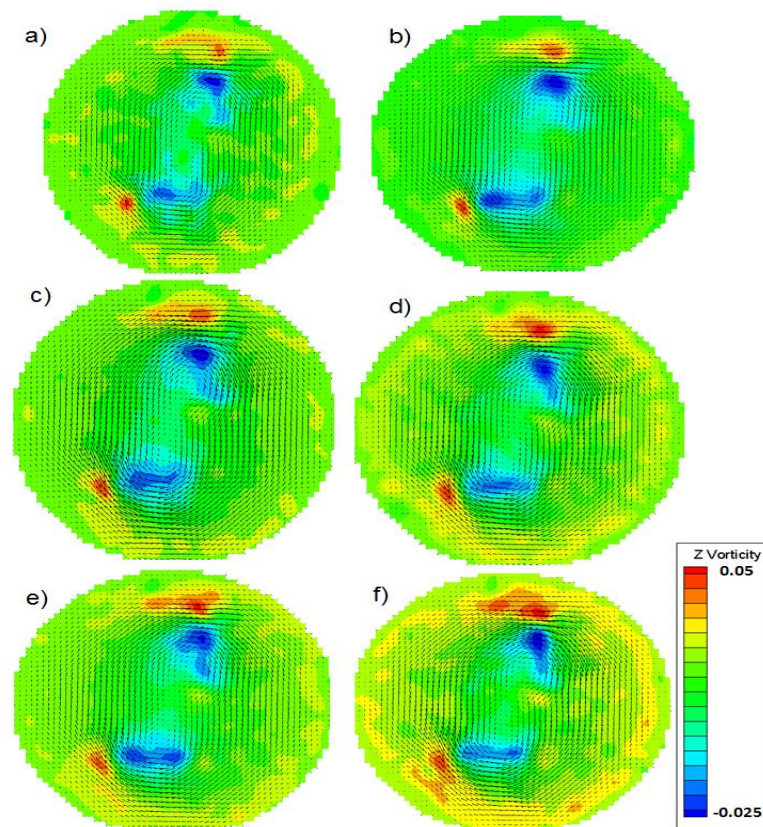
Figure 3 Axial vorticity in two different planes: a) 10 rpm lower plane; b) 10 rpm upper plane; c) 20 rpm lower plane; d) 20rpm upper plane; e) 30rpm lower plane; f) 30 rpm upper plane

Conclusions

An experimental study has been conducted for analyzing the flow fields of a planetary mixer. For that purpose, the flow was visualized by means of the PIV technique. Although, several parameters can be obtained when using this visualization technique, vorticity fields were here reported. They were useful for observing large vorticity regions, which allow identifying rich mixing regions. Results from this study could be later used for validating some findings obtained from numerical studies.

References

[1] Tanguy, P.A., Thibault, F., Dubois, C. y Ait-Kadi, A., (1999), Trans IChemE, Vol. 77, Part A: 318 - 324.

[2] Zhou, G., Tanguy, P.A. y Dubois, C., (2000), Trans IChemE, Vol. 78, Part A: 445 - 453.

[3] Cliffort, M.J., Cox, S.M. y Finn, M.D., (2004), Chem. Eng. J., 59, Part A: 3371 - 3379.

[4] Delaplace, G., Guérin, R., y Leuliet, J.C., (2005), AIChE Journal, Vol. 51, No 12: 3094 - 3100.

[5] Delaplace, G., Thakur, R.K., Bouvier, L., André, C. y Torrez, C., (2007), Chem. Eng. J., 62, 1442 - 1447.

[6] André, C., Demeyre, J.F., Gatumel, C., Bethiaux, H. y Deplace, G., (2012), Chem. Eng. J., 198-199, 371 - 378.

[7] Jian, L., Xiaboin, Z., Yili, Y., Xiwen, L., y Tielin S., (2016), AIME, Vol. 8: 1-12.

INP Toulouse 6 allée Emile Monso, 31029 Toulouse cedex 4, France

David Israel Posadas Navarro
UNAM
Street Tlaloc Mz 19 Lt22 Arenal firts section
15600 Mexico City
Mexico

Toulouse, 04/Sep/2018

To Whom It May Concern

Dear Madam or Sir,

We confirm that **David Israel Posadas Navarro** participated at 16th European Conference on Mixing.

David Israel Posadas Navarro is author/co-author of the following accepted contribution(s):

Flow Fields Generated in a Double Planetary Mixer
Author(s): Posadas Navarro, David Israel
Presenting Author: Posadas Navarro, David Israel
Submission Type / Conference Track: Extended abstract (4 pages)

Numerical Analysis of Viscous Heating in a Double Planetary Mixer
Author(s): Ramírez-Cruz, Jorge; Salinas-Vázquez, Martín; Ascanio-Gasca, Gabriel; Palacios-Morales, Carlos; Posadas-Navarro, David Israel
Presenting Author: Ramírez-Cruz, Jorge
Submission Type / Conference Track: Extended abstract (4 pages)

With best regards,

INSTITUT NATIONAL POLYTECHNIQUE
Service d'Activités Industrielles et Commerciales
6 allée Emile Monso - B.P. 34038
F-31029 TOULOUSE CEDEX 4
Téléphone 05 34 32 31 24

Organisateurs MIXING16
mixing16@inp-toulouse.fr

Dear David Israel Posadas Navarro,

Congratulations! Your abstract, *A Comprehensive Hydrodynamic Assessment of an Agitated Fermenter*, has been accepted for presentation at the 2020 AIChE Annual Meeting.

We are excited to have you in our program this fall. However, we understand that there is uncertainty regarding travel this fall due to the coronavirus pandemic. Please know that these concerns and the health and safety of all meeting participants, attendees, speakers, and staff is of the utmost concern and importance to us.

Keeping this in mind, we are in the process of finalizing **virtual participation options** so that all may participate regardless of their ability to attend in-person. However, the Meeting format may need to change as more information on the travel situation is known.

Over the next several weeks, **parts of the program may move to a virtual setting**. We will communicate with all speakers' once arrangements have been finalized. You will receive a final communication with details of your talk, including type, location, and time, over the next few weeks.

What you need to do now:

1. Please **notify all co-authors** of this acceptance.

2. **If your plans have changed** and you will not be able to participate in the Meeting (<u>even if it is virtual</u>), please contact your session chairs and programming@aiche.org as soon as possible so that alternative arrangements can be made.

    If you are concerned about travel but would still be able to participate in a virtual meeting, we ask you to please refrain from cancelling your participation until final arrangements have been announced.

3. **If presenting authors require a preliminary invitation letter,** please contact AIChE Program Development at programming@aiche.org. A more detailed invitation letter will be available for automatic download once the program is finalized in the coming weeks.

Again, congratulations! We thank you for your submission, and look forward to seeing your presentation.

Best regards,
Jennifer S. Curtis
2020 Annual Meeting Program Chair
University of California, Davis
2020Annual@aiche.org

A Comprehensive Hydrodynamic Assessment of an Agitated Fermenter

Abstract

Fluid mixing is a fundamental operation in wide range of the industries as biochemical and chemical industries. The mixing is fundamental for some process such as fermentation, wastewater, crystallization and polymerization. Stirred tanks are used for the homogenization of single or several phases. The gas-liquid system has received considerable interest in the last decades. Both the mechanical agitation and sparging play an important role in the design of this kind of systems.

To produce the required degree of uniformity inside the bioreactor the sparging and the agitation they should be the best possible. In the literature, many types of impellers have been reported for different applications. These studies demonstrate that the traditional Rushton turbine impeller has some advantages over other impellers for the gas-liquid mixing operations, although it has also shown some drawbacks such as the formation of dead regions [1]. This indicates that radial impellers provide poor pumping characteristics, which can be overcame using axial-flow for providing downward flow. However, these impellers showed other disadvantages such as torque instabilities and more power demand [2, 3].

In this study we analyzed the hydrodynamic performance of a new impeller called axial-radial impeller (ARI) in a stirred tank containing a Newtonian fluid, which was designed in our research group [4]. We do a comprehensive hydrodynamic assessment through of global and local parameters. We used the non-intrusive of PIV technique for local parameters (flow patterns, turbulent intensity, vorticity) and a torquemeter together with an electrode oxygen dissolved for global parameters (power consumption and volumetric mass transfer coefficient).

The hydrodynamic performance of the ARI impeller was compared to the performance of the radial-flow Rushton impeller and the axial-flow pitched blade turbine.

We used an experimental setup, which consists basically of a glass vessel of diameter T of 190 mm and liquid height H of 305 mm and an operating volume of 0.008 m^3. The vessel is a cylinder with torispherical bottom and we put four baffles having a width J of 15.8 mm equally spaced with the aim of minimizing vortexing in the free-surface. Also, we put a ring sparger to supply air to the vessel at a distance of 59 mm measured from the bottom of the tank. We used sets of three impellers with a diameter Da of 63 mm coaxially placed along the shaft, namely: Rushton turbines (RT), 6-pitched blade turbines (PBT) and axial-radial impellers (ARI). They were driven with a 373 W (0.5 hp) DC motor (Baldor Reliance CDP330), whose speed was carefully controlled with a KBMD Baldor control and monitored with a tachometer (Delta CTA4). We mounted the first impeller on the shaft at a distance of 31.6 mm (C_1) measured from the sparger and the second impeller at a distance of 63.3 mm (C_2) measured from the first impeller and the third impeller at a distance of 63.3 mm (C_3) measured from the second impeller. With the aim of minimizing air intake to the working

liquid, the distance between the third impeller and the free-surface we placed it to 92 mm (C_4). For a complete gas dispersion and with the aim of avoiding flooding as a function of volumetric gas flow rate from 0.125 to 2 vvm, the minimum rotation speed was set to 1.326 m/s, equivalent to N = 400 rpm.

Inside of the vessel, we poured the working fluid, which was made up with sodium alginate dissolved in distilled water at a concentration of 1 g/L, whose liquid density and dynamic viscosity was ρ= 997 kg·m^{-3} and μ= 6 mPa·s, respectively.

Figure 1a) and Fig. 1b) (first row) shows the results of the power drawn by the impellers and the mass transfer, which were determined using the methodology described elsewhere [5, 6]. The power number (N_{pg}) *vs* flow rate number (Fl_g) are used to present the results of the power consumption and volumetric mass transfer coefficient (K_La) vs volume of air per volume of liquid (vvm) are used to present the results of the mass transfer.

As expected, the power number decreases as the flow number increases; however, for Fl_g higher than 0.05, the power number remains practically constant, which indicates that the turbulent regime has been reached. In the case of the Rushton turbines, the power drops quickly as the flow number increases; however, once the turbulent regime has been reached, the Rushton turbines require less power compared with the two other impellers. As reported elsewhere, this is due to the large cavities formed behind the blades and the higher frequency of bubble breakage [7-9]. It is noticeable that hybrid impellers (ARI) demand higher power. In such impellers, straight blades are attached to pitched blades like winglets. As these impellers rotate, small cavities are formed behind the straight blades and more energy would be required for bubble breakage, which could explain the higher power demanded. On the other hand, the figure 1 (b) shows the volumetric mass transfer coefficient for the impellers investigated as a function of the aeration rate in a *vvm* range from 0.25 to 2 min^{-1}. As expected, K_La increases with increasing the aeration rate, although the mass transfer values are highly dependent on the impeller used. As this figure shows, Rushton turbines exhibit the highest mass transfer capacity, while the lowest one is observed with the PBT at low *vvm*. However, this trend changes for *vvm* values higher than 0.5 min^{-1}, so that ARI impellers show the lowest mass transfer capacity.

Figures 1c), 1d), 1e), 1f), 1g), 1h) show the flow patterns obtained in the X-*Y* plane from the PIV measurements for the Rushton turbine (Fig. 1c) and Fig. 1f), the pitched blade turbine (Fig. 1d) and Fig. 1g), and the axial radial impeller (Fig. 1e) and Fig. 1h) for single-phase (second row) and gassed phase (third row) conditions. For all cases, the Reynolds number is *Re*=33502 and for gassed conditions the gas flow rate is 0.25 vvm. The color scale represents the velocity field magnitude normalized by V$_{tip}$ and the impellers contour is illustrated with continuous lines and the horizontal and vertical dimensions (X and Y, respectively) are normalized using the radius of the tank (T/2).

As can be seen, the Rushton turbine exhibits more homogenous flow patterns in the whole tank and with more regions where the flow is faster for both conditions (single-phase and gassed phase). Besides, the flow pattern in the gas phase changed considerably probably due to the strong interaction between the turbine and gas bubbles dispersed in the flow, which are concentrated between the second and third impellers. For the pitched blade turbine and the
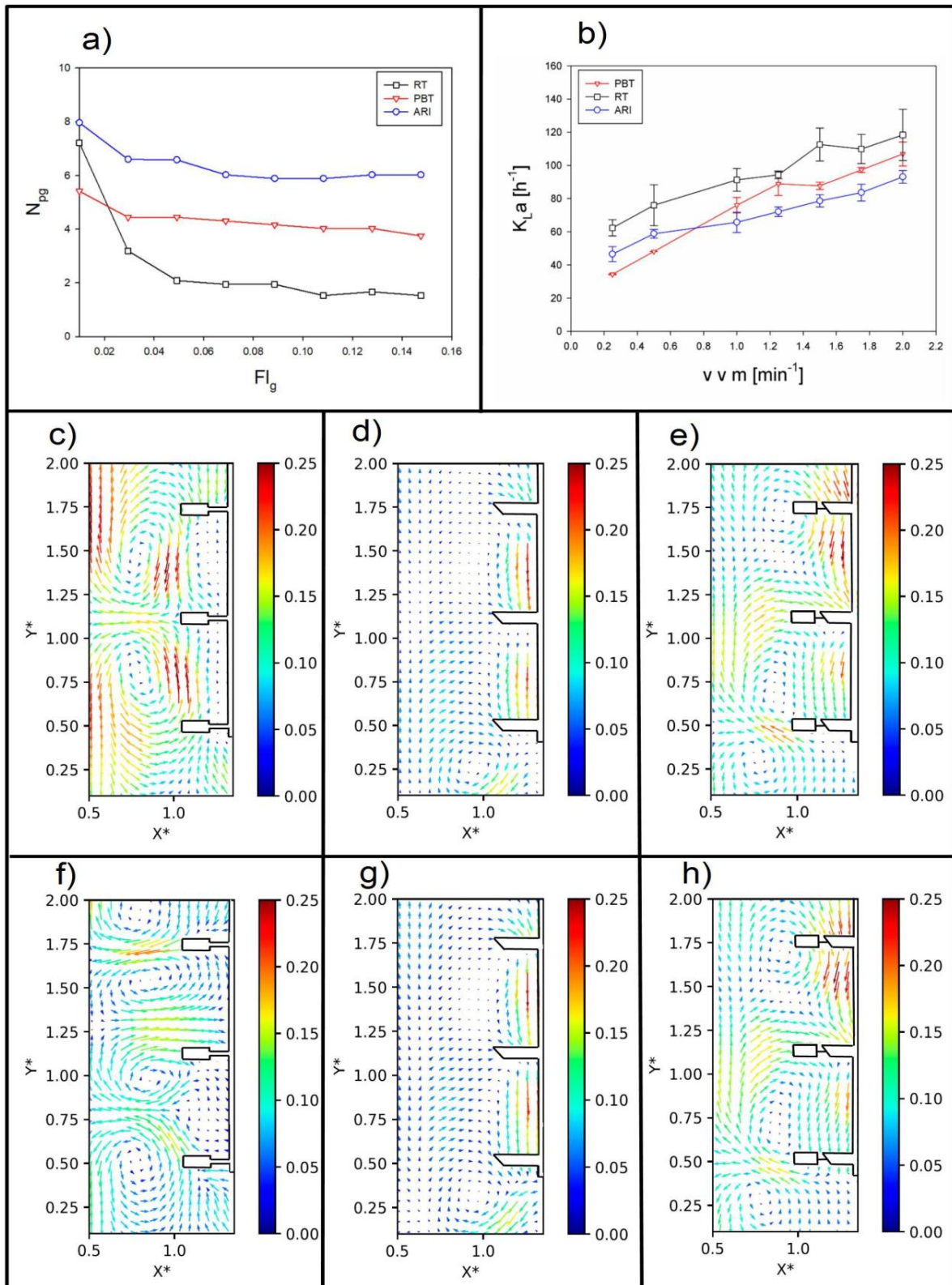
Figure 1- Global and local parameters for RT, PBT and ARI: a) Power consumption; b) Volumetric mass transfer coefficient and typical flow patterns for a X-Y plane for: RT, c) single-phase, f) 0.25 vvm; PBT, d) single-phase, g) 0.25vvm; ARI, e) single-phase, h) 0.25 vvm

impeller blades as for the case Rushton turbine. Nevertheless, we can see that the axial-radial impeller (ARI) creates a more complex flow pattern compared with the one created by the pitched blade turbine, in which more high-velocity regions are observed close to the shaft.

In this study, the hydrodynamic performance of a hybrid impeller was analyzed and compared to a Rushton turbine and a pitched blade turbine. The most relevant conclusions are:

Rushton turbines demand lower power and provide higher mass transfer capacity. Also, more homogeneous flow patterns were observed with these impellers as well as more high-velocity regions. On the other hand, PBT and ARI turbines showed similar hydrodynamics characteristic.

References

1. Nienow, A. W. "Gas-Liquid Mixing Studies-A Comparison of Rushton Turbines with Some Modern Impellers." *Chemical engineering research & design*4 (1996): 417-423.
2. McFarlane, Caroline M., and Alvin W. Nienow. "Studies of high solidity ratio hydrofoil impellers for aerated bioreactors. 1. Review." *Biotechnology progress*6 (1995): 601-607.
3. Nienow, A. W. "Hydrodynamics of stirred bioreactors." (1998): 3-32.
4. Ascanio, Gabriel, Stephane Foucault, and Philippe A. Tanguy. "Performance of a new mixed down pumping impeller." Chemical Engineering & Technology: Industrial Chemistry-Plant Equipment-Process Engineering-Biotechnology 26.8 (2003): 908-911.
5. Ascanio, G., B. Castro, and E. Galindo. "Measurement of power consumption in stirred vessels—a review." *Chemical Engineering Research and Design*9 (2004): 1282-1290.
6. Garcia-Ochoa, Felix, and Emilio Gomez. "Bioreactor scale-up and oxygen transfer rate in microbial processes: an overview." *Biotechnology advances*2 (2009): 153-176.
7. Ozcan-Taskin, N. G., A. W. Nienow, and S. Chatwin. "Les characteristiques de puissance des lntermigs et des turbines Rushton dans les fluides viscoelastiques a viscosite constante." *Agitation Industrielle, J*(1992): 11-10.
8. Kipke, K. D. "Fluid loadings on impellers and tanks in gassed liquids." *Fourth European Conference on Mixing*. 1982.
9. Derksen, Jos, and Harry EA Van den Akker. "Large eddy simulations on the flow driven by a Rushton turbine." *AIChE Journal*2 (1999): 209-22

AIChE
The Global Home of Chemical Engineers

AMERICAN INSTITUTE OF CHEMICAL ENGINEERS

120 WALL STREET, 23 FL.
NEW YORK, NY
10005 USA

Certificate of
Professional Development Hours

The purpose of Continuing Professional Competency (CPC) is to ensure that qualified technical professionals maintain a satisfactory level of competency. Participating in AIChE conferences and meetings may quality as CPC in certain jurisdictions in that:

- *There is a clear purpose and objective relating directly to the practice of engineering.*
- *The content of the meetings and conferences are well organized and documented.*
- *The outline and presentation demonstrate prior planning of the underlying course learning.*
- *The presenters are well qualified on the basis of education and experience to serve as AIChE speakers and discussion leaders.*
- *The record of attendance is verifiable by the possession of this certificate and AIChE registration records.*

THEREFORE

David Israel Posadas Navarro

Is credited, under the above criteria, with 24 professional Development Hours for attending the
2020 Virtual AIChE Annual Meeting

Virtual Meeting
November 16-20, 2020

24 Professional Development Hours

June C. Wispelwey
Executive Director, AIChE

To Whom It May Concern:

The American Institute of Chemical Engineers (AIChE) with more than 60,000 members from over 110 countries is the premiere professional society for chemical engineering. AIChE would like to thank you for attending the 2020 Virtual AIChE Annual Meeting, held virtually. The conference formally ran from November 16-20, 2020 with some technical activities taking place before and after the conference.

This letter confirms that David Israel Posadas Navarro presented the following paper in the 2020 Virtual AIChE Annual Meeting on November 16 – 20, 2020:
"A Comprehensive Hydrodynamic Assessment of an Agitated Fermenter"
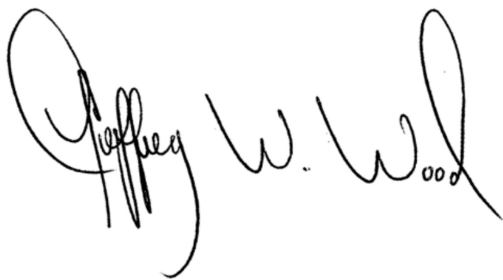
The technical program can be found at the following page:
https://aiche.confex.com/aiche/2020/meetingapp.cgi

The 2020 Virtual AIChE Annual Meeting is accomplished by participation of all who attend the conference. The above participations were beneficial and invaluable to the meeting and the dissemination of knowledge. We are pleased that you have joined us. Should you require additional information, please do not hesitate to contact me.

Thank you very much.

Regards,

Jeffrey W. Wood
Meetings Director
American Institute of Chemical Engineers
120 Wall Street, 23rd Floor
New York, NY 10005
Email: meetings@aiche.org

CHISA 2022 | 21–25 AUGUST 2022
PRAGUE, CZECH REPUBLIC

Organised by:

ČSCHI
ČESKÁ SPOLEČNOST CHEMICKÉHO INŽENÝRSTVÍ
CZECH SOCIETY OF CHEMICAL ENGINEERING

EFCE

AIChE
The Global Home of Chemical Engineers

power consumption and mass transfer of rotor-injector devices in a water physical model of an aluminum degassing ladle to scale

[1]D. I. Posadas, [1]G. Ascanio, [1]E. Bernal, [2]M. A. Ramírez, [2]C. González, [3]A. Blancas

[1]Universidad Nacional Autónoma de México, Instituto de Ciencias Aplicadas y Tecnología, Circuito Exterior S/N, Ciudad Universitaria, Coyoacán, 04510 Ciudad de México, México; tel.+52 55 56-22-86-02, Ext 1316, e-mail: edalimdy@hotmail.com; tel.+52 55 56-22-86-02, Ext 1333, e-mail: gabriel.ascanio@icat.unam.mx; tel.+52 55 56-22-86-02, Ext 1334, e-mail: eduardo.bernal@icat.unam.mx

[2]Universidad Nacional Autónoma de México, Departamento de Ingeniería Metalúrgica, Facultad de Química, Edificio D, Circuito de los Institutos S/N, Ciudad Universitaria, Coyoacán, 04510 Ciudad de México, México; tel.+52 55 56-22-52-46, e-mail: marco.ramirez@unam.mx; tel.+52 55 56-22-52-38, e-mail: carlosgr@unam.mx

[3]Universidad Nacional Autónoma de México, Instituto de Investigaciones Biomédicas, Unidad de Bioprocesos, Circuito Exterior S/N, Ciudad Universitaria, Coyoacán, 04510 Ciudad de México, México; tel.+52 55 56-22-91-86, e-mail: planta@biomedicas.unam.mx

Introduction

One of the most relevant metallurgical operations for aluminum processing is referred to as the process of dehydrogenation of molten aluminum. The presence of hydrogen in a metal alloy can lead defects in the final products. To avoid that problem, the rotor-injector method has been widely accepted to perform the degassing and cleaning processes in the aluminium industry [1,2]. In this sense, the rotor geometry plays an important role in gas removal kinetics. Using the PIV technique, Mancilla et al. [3] studied the hydrodynamics of three rotor designs, including a new rotor-injection device design. The authors reported that the new design exhibits better performance under gassed conditions, showing high turbulent intensities, producing a higher gas breakup rate, and promoting the formation of small bubbles that the rotor can easily distribute over the entire ladle. However, the study mentioned above was mostly qualitative. For this reason, this study aims to perform a quantitative analysis of the rotor's designs studied elsewhere [3] in terms of power consumption and mass transfer capacity.

Methodology

Figure 1 shows the experimental setup and rotors used in the present work. It consists of a cylindrical vessel made of glass. Air was supplied to the tank through the rotor shaft. Three rotors were evaluated in the present study, namely: notched rotor, novel rotor, and standard rotor. The system was powered by a motor attached to a pulley system. The power drawn (P) by the rotors was determined by measuring the torque as described in detail by Ascanio [4]. For that purpose, a rotatory torque sensor was coupled between the motor and the driving shaft. On the other hand, the mass transfer capacity was analyzed in terms of the volumetric mass transfer coefficient (K_La) using the dynamic method reported by Garcia and Gómez [5]. For that purpose, a dissolved oxygen probe was placed in the tank. For all tests, the rotational speed was fixed at 300 rpm in order to avoid air intake into the tank due to the vortex that is formed on the free surface. On the other hand, gas rates were 0.1, 0.4, and 0.7 vvm (volume of gas per volume of liquid per minute), which are common gassing rates in industrial processes.

Results

As figure 2a shows, the novel rotor consumes the highest power followed by the standard rotor, and at last the notched rotor. The fact that the novel rotor consumes more power indicates that this rotor can transfer more energy to the liquid, which translates into a better agitation throughout the tank. The major power consumption by the novel rotor can be due to the design

of its lower blades, which provide greater resistance to rotation. On the other hand, figure 2b shows that the novel rotor exhibits better mass transfer capacity at high gas rates, probably due to the geometry of the blades helping to break up better bubbles, which causes a better distribution of these throughout the tank.
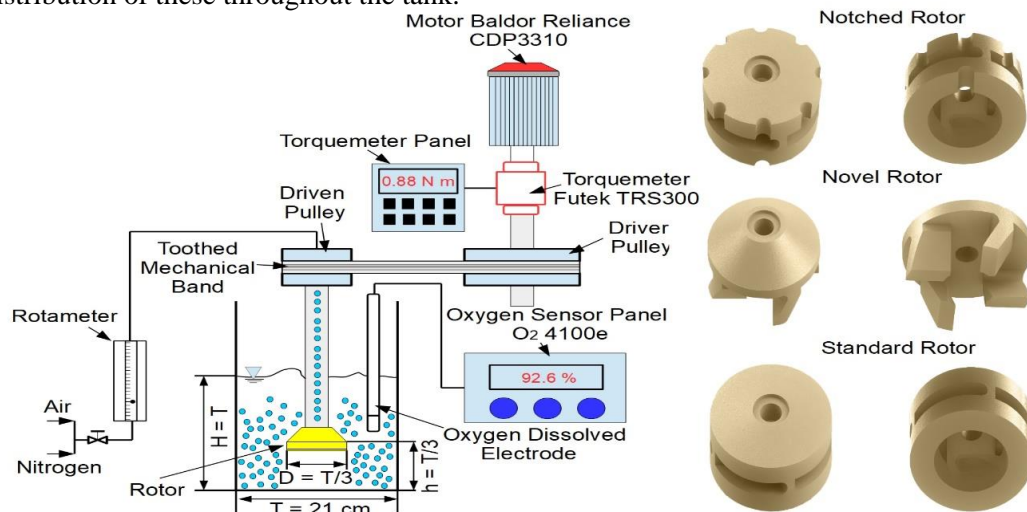
Figure 1. Experimental setup and rotors used in this work
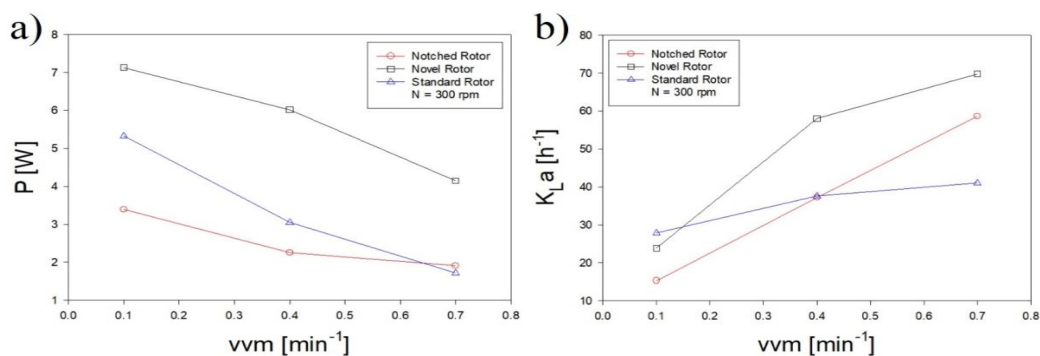
Figure 2. a) Power consumption as a function of vvm; b) Mass transfer capacity as a function of vvm

Conclusions

In this work, the power consumption and mass transfer capacity of three types of rotors was evaluated. Results showed that the new rotor design achieves a better transfer of energy to fluid and high mass transfer capacity. This indicates that this rotor will obtain a more vigorous agitation and increase the kinetics of the degassing process of aluminum, which suggests the novel rotor would be an attractive alternative for the processes of dehydrogenation.

References

[1] G. Mi, S. Qi, X. Liu, J. Niu, *Mater. Sci. Eng. A*. **2009**, *499*, 195–199. https://doi.org/10.1016/j.msea.2008.07.004.

[2] M. Saternus, J. Botor, *Metalurgija*. **2009**, *48*, 175–179.

[3] E. Mancilla, W. Cruz-Méndez, I.E. Garduño, C. González-Rivera, M.A. Ramírez-Argáez, G. Ascanio, *Chem. Eng. Res. Des*. **2017**, *118*, 158–169. https://doi.org/10.1016/j.cherd.2016.11.031.

[4] G. Ascanio, B. Castro, E. Galindo, **2013**, *82*, 1282–1290. https://doi.org/10.1205/cerd.82.9.1282.44164.

[5] F. Garcia-Ochoa, E. Gomez, **2009**, *27*, 153–176. https://doi.org/10.1016/j.biotechadv.2008.10.006.

Estimado **David Israel Posadas Navarro**:

A nombre de la mesa directiva de la **División de Dinámica de Fluidos de la Sociedad Mexicana de Física**, agradezco su amable participación en el **XXVII Congreso de la División de Dinámica de Fluidos**.

Este año nos orgullece haber tenido un mayor número de presentaciones orales y de carteles en la sección correspondiente. Cabe destacar que la audiencia que presenció el congreso a través de las redes sociales se incrementó considerablemente.

Tanto los colegas de la mesa directiva, como un servidor, compartimos la opinión de que gracias a los trabajos presentados se logró un nivel muy notable en términos de la calidad general del evento.

En virtud de lo expuesto, deseamos extenderle la más cordial invitación para contar nuevamente con su apreciable participación en la siguiente edición de nuestro congreso.

Aprovecho la ocasión para enviarle un cordial saludo y desearle un magnífico año 2022.

Atentamente,

Dr. Enrique Guzmán

DDF – SMF
Presidente

Appendix B
Published article

David Posadas-Navarro[1]

Carlos Palacios[2]

Abel Blancas-Cabrera[3]

Mauricio A. Trujillo-Roldán[3]

Martín Salinas-Vázquez[4]

Gabriel Ascanio[5,*]

Flow Patterns of Multiple Axial-Radial Impellers for Potential Use in Aerated Stirred Tanks

The hydrodynamics of a stirred tank equipped with multiple hybrid impellers was experimentally characterized. They were coaxially placed to agitate a viscous Newtonian fluid under gassed conditions. Experiments were performed by using the particle image velocimetry technique, and flow fields were reported in terms of the velocity magnitude, vertical currents, turbulent intensity, and strain rates. For comparison purposes, impellers providing radial flow (Rushton turbines) and axial flow (pitched blade turbines) were also tested. The results showed that hybrid impellers provided a uniform flow distribution throughout the tank at moderate strain rates, which make them an attractive alternative for fermentation processes with shear-sensitive cultures and viscous liquids.

Supporting Information available online

1   Introduction

Gas-liquid systems have been the subject of numerous studies in recent years [1–4]. They are characterized by high mass and heat transfer coefficients, good liquid and gas mixing capacities, longer residence times of gas in the liquid phase, as well as the possibility of handling a wide range of superficial gas velocities. These systems are commonly used in biological applications, such as the culture of bacteria, fungi, and animal cells [5–7]. Stirred tanks are commonly used in such applications to obtain complete homogenization of products from several phases. On the other hand, the use of systems with two or three impellers has shown some advantages over single-impeller systems, such as increasing the gas hold-up and improving the mass transfer capacity [8]. However, having more than three impellers on the shaft results in a noticeable increase of power consumption, and the mixing process is not necessarily improved [9].

Nowadays, several types of impellers are available to be used for different applications. The traditional Rushton turbine (RT) has some advantages over other impellers in gas-liquid mixing operations [10]. Although RTs draw less power when operating in the turbulent regime, the flow is prone to dead zones, as a result of their poor pumping capacity, particularly when using viscous fluids. To overcome such a drawback, axial-flow impellers have been designed and tested. However, the use of such impellers leads to torque instabilities and higher power demand when operated in the down-pumping mode [11]. Axial-flow impellers operating in the up-pumping mode have shown some advantages over those operating in the down-pumping mode, such as less power consumption, fewer torque instabilities when operated in aerated media systems, but poor mass transfer characteristics [12, 13].

To overcome the deficiencies exhibited by the aforementioned impellers, a hybrid turbine known as the axial-radial impeller (ARI) was designed and reported elsewhere [14], which combines tilted blades and straight blades for generating mixed flow. The performance of the axial-radial impeller has been evaluated in coaxial mixers [15–17] with an anchor on shear-thinning fluids and fluids exhibiting yield stress. Its hydrodynamic performance was compared with those of an RT and an A200 impeller as central impellers by means of electrical resistance tomography and computational fluid dynamics. The combina-

[1]David Posadas-Navarro
Programa de Maestría y Doctorado en Ingeniería, Universidad Nacional Autónoma de México, Ciudad Universitaria, 04510, Ciudad de México, México.

[2]Dr. Carlos Palacios
Facultad de Ingeniería, Universidad Nacional Autónoma de México, Circuito Exterior S/N, Ciudad Universitaria, 04510, Ciudad de México, México.

[3]Abel Blancas-Cabrera, Dr. Mauricio A. Trujillo-Roldán
Unidad de Bioprocesos, Instituto de Investigaciones Biomédicas, Universidad Nacional Autónoma de México, Circuito Exterior S/N, Ciudad Universitaria, 04510, Ciudad de México, México.

[4]Dr. Martín Salinas-Vázquez
Instituto de Ingeniería, Universidad Nacional Autónoma de México, Circuito Exterior S/N, Ciudad Universitaria, 04510, Ciudad de México, México.

[5]Dr. Gabriel Ascanio
gabriel.ascanio@icat.unam.mx
Instituto de Ciencias Aplicadas y Tecnología, Universidad Nacional Autónoma de México, Circuito Exterior S/N, Ciudad Universitaria, 04510, Ciudad de México, México.

tion of the anchor with the axial-radial impeller was found to be more efficient than the combination of the anchor with the Rushton impeller or with the A200 axial-flow impeller.

On the other hand, the efficiency of a mixing system is highly influenced by the flow patterns generated by the impellers within the tank [18]. These patterns are influenced by certain parameters to achieve optimal mixing of biological media, such as the velocity magnitude, turbulent intensity, and strain rate. For instance, velocity fluctuations (turbulent intensity) help to improve the mixing process [19]. Some authors have found that there is a close interaction between the morphology, the broth rheology, and the turbulent intensity in submerged fungal fermentations in stirred tank reactors [20–22]. On the other hand, the turbulent intensity can be linked to the strain rate. As impellers rotate, biological media are subjected to deformation gradients, which eventually can lead to sublethal damage or even to cell death or alterations in the metabolic process of the cell [23, 24]. The damage levels depend on the intensity of the shear stress and the particular cellular species [25]. Hence, it is important to determine the distribution of strain rates throughout the tank, which allows one to establish whether a certain biological medium will be subjected to forces that result in an adverse effect. In this sense, the visualization of flow patterns is of utmost importance when characterizing the hydrodynamics of new impeller geometries.

The aim of this paper is to characterize experimentally the hydrodynamic performance of multiple coaxial hybrid turbines, or ARIs, in an aerated tank. Such characterization was done in terms of the flow fields, vertical currents, turbulent intensity, and strain rates, which were obtained from particle image velocimetry (PIV) experiments. To the best of the authors' knowledge, this work is the first experimental study on mixed flow impellers in a gas-liquid system. For comparison purposes, the experiments have been also done with impellers providing radial flow and axial flow by using RTs and pitched blade turbines (PBTs), respectively.

2 Methodology

Experiments were done in a cylindrical vessel with torispherical bottom. Four equally spaced baffles were placed with the aim of minimizing vortexing in the free surface. Fig. 1a shows the impellers tested in this work, which consisted of sets of three impellers mounted coaxially along the shaft to provide radial, axial, and mixed flow. The power drawn by the impellers was determined by measuring the torque as described elsewhere [26]. For that purpose, a rotary torque sensor (Futek TRS300) was coupled between the motor and the impeller shaft. Subsequently, the power consumption was calculated with Eq. (1):

$$P = 2\pi NM \tag{1}$$

where $N^{1)}$ and M are the rotational speed and effective torque, respectively.

On the other hand, for the gas phase, gas was supplied at the center of the tank, below the impellers, through a ring sparger having 16 holes 0.0015 m in diameter. Fig. 1b shows the impellers and the sparger, which was similar to that as reported elsewhere [27]. Tab. 1 summarizes the experimental conditions used for this work.
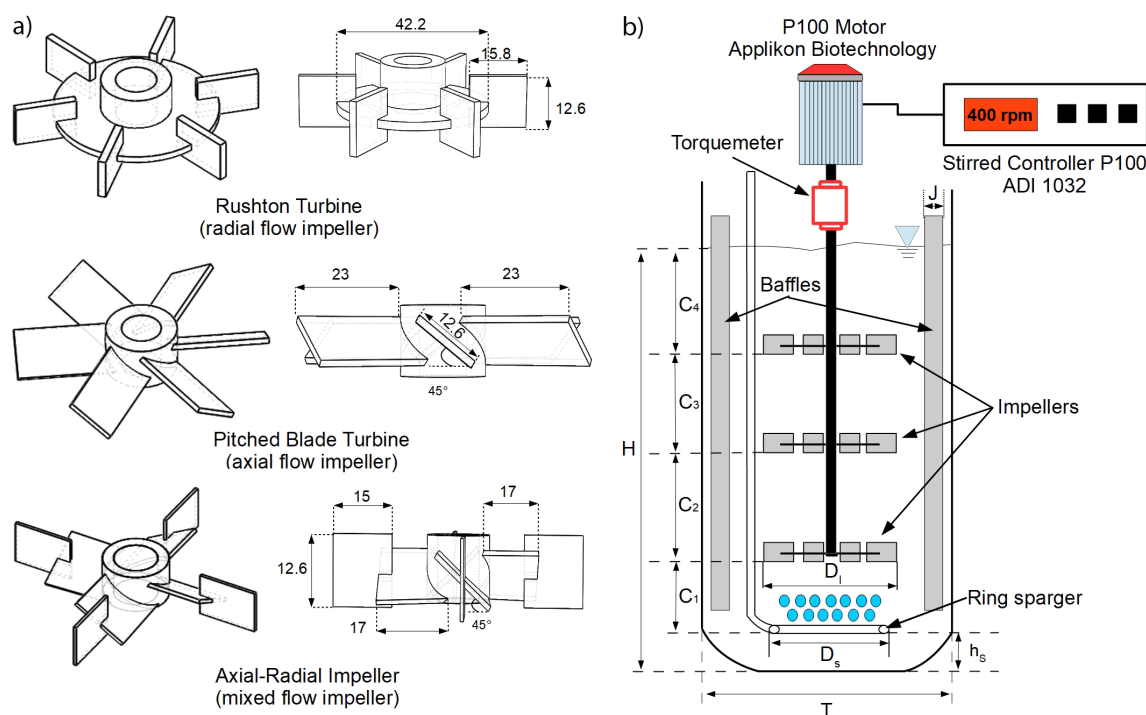
Figure 1. Experimental setup. (a) Impellers used in this study. (b) Arrangement of impellers and sparger in the tank. Dimensions in millimeters.

---

1) List of symbols at the end of the paper.

Table 1. Experimental conditions. V_o, operating volume.

Parameter	Value
T [m]	0.190
H [m]	0.305
h_s [m]	0.059
V_o [m³]	0.008
D_I [m]	0.0633
D_s [m]	0.050
J [m]	0.0158
C_1 [m]	0.0316
C_2 [m]	0.0633
C_3 [m]	0.0633
C_4 [m]	0.092

The tank was filled with the working fluid, which was a viscous solution of sodium alginate dissolved in distilled water at a concentration of $1\,g\,L^{-1}$ to give a Newtonian fluid with dynamic viscosity and liquid density of μ = 5 mPa s and ρ = kg m^{-3}, respectively.

The PIV technique was used to obtain the two-dimensional flow fields. For that purpose, an Nd:YAG double-pulsed laser (532-nm green light, 30 mJ, 100 Hz) and a high-speed Phantom camera (SpeedSense 9040, 1632×1200 pixels resolution) coupled to a Nikon lens of 50 mm f/2.8D were used. The laser was coupled to an optical array to generate a light sheet with a thickness of about 1 mm.

Fig. 2 shows the PIV setup used in this work. The camera was placed perpendicularly with respect to the laser light sheet. The flow was seeded with tracer particles. In the present study, polyamide microspheres (50-µm mean diameter) coated with rhodamine 6G were added. A 300-nm optical filter coupled to the camera lens was used to obtain only the light reflected by the particles; in that way, it was possible to minimize the light reflected by the bubbles and other surfaces. For synchronization purposes, the laser and the camera were connected to a PCI-6601 card (timerbox).

A cross-correlation algorithm was used to obtain the velocity vectors by using an interrogation area of 32×32 pixels with 50 % overlap and a time between pulses of 1500 µs to obtain a spatial resolution of 2.7×2.7 mm (cell size).

Data obtained from the PIV experiments were processed by following the procedure described elsewhere [28]. For better visibility of the flow, the measurements were made at an angle of 0° just in front of one of the baffles. With the aim of obtaining statistically robust results, 400 individual images were obtained with the phase/locking technique and processed. Flow fields obtained from the experiments are reported in terms of the following

parameters: velocity magnitude, turbulent intensity, and strain rate. They were calculated according to Eqs. (2), (3), and (4), respectively.

$$|V| = \sqrt{u^2 + v^2} \tag{2}$$

$$TI = \frac{\sqrt{\overline{u'^2} + \overline{v'^2}}}{V_{tip}} \tag{3}$$

$$|\bar{S}| = \sqrt{S_{ij}S_{ij}} \tag{4}$$

where u, u', v, v', and V_{tip} are the horizontal component velocity, the horizontal velocity fluctuation, the vertical component velocity, the vertical velocity fluctuation, and impeller tip velocity, respectively, and $|\bar{S}|$ and S_{ij} are the modulus of the strain rate tensor and the strain rate tensor, respectively.

Finally, the pumping capacity of the impellers used in the present work was also investigated in terms of the pumping number N_q, which was calculated as Eq. (5):

$$N_q = \frac{Q_v}{ND_I^3} \tag{5}$$

where Q_v is the total volumetric flow rate, N the rotational speed, and D_I the impeller diameter. The detailed description of this method is given elsewhere [29].

For all experiments, the rotational speed N was 6.66 rps (400 rpm), and the air flow rate was fixed at Q = 2 L > min^{-1}, equivalent to 0.25 volume of gas per volume of liquid per minute (vvm). Such conditions were based on the experimental works reported elsewhere for applications in fermentation pro-
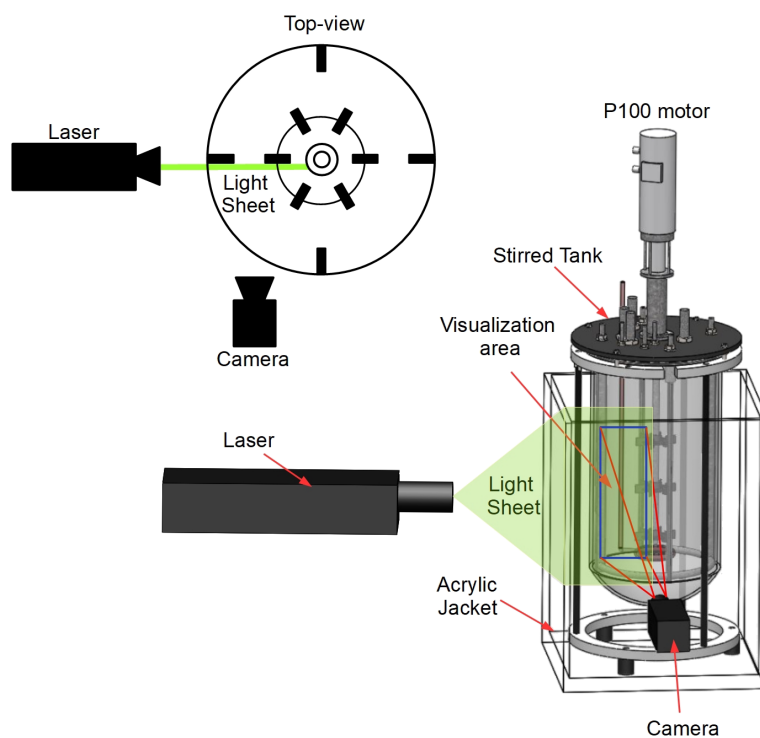
Figure 2. PIV setup.

cesses [30–33]. Under these conditions, the Reynolds number was $Re = 5.2 \times 10^3$, which indicated operation in the turbulent flow regime [34], so that a reasonable estimation of local quantities can be obtained from 2D measurements.

3   Results and Discussion

Flow patterns were obtained from the PIV experiments, and they are reported in terms of the velocity magnitude, vertical currents, turbulent intensity, and strain rates. For all cases, the results are shown with the horizontal and vertical dimensions X and Y, respectively, normalized with the radius of the tank $T/2$, and the contours of the impellers are illustrated with solid lines.

Figure 3. Flow patterns in the *X-Y* plane. (a) ARIs. (b) PBTs. (c) RTs. *X** and *Y** are the dimensionless horizontal and vertical positions, respectively.

3.1   Velocity Magnitude

The flow fields generated by the sets of impellers in the *X-Y* plane are shown in Fig. 3. The color scale shows the velocity magnitude normalized with the impeller tip velocity.

As Fig. 3a shows, several vortical structures were formed between the hybrid impellers and the tank wall, which is a consequence mainly of the flow discharged in the radial direction. Also, a high-velocity region is observed below and above the upper impeller, very likely due to the short distance from the free surface. In the rest of the tank, the working fluid is uniformly displaced at a moderate velocity. Such a flow distribution is indeed a result of the interaction of the flow discharged by these impellers. These findings are in good agreement with the results reported elsewhere [15].

Fig. 3b shows the flow patterns created by the PBTs. Because they are operated in the down-pumping mode, the fluid is discharged mainly downwards in the axial direction. The poor interaction of the flow discharged by each impeller results in high-velocity regions along the shaft between the impellers and quasi-stagnant regions near the tank wall.

Regarding the RTs, four vortical structures are created as result of the interaction between the impellers, and weak flow regions (quasi-static flow) near the impeller shaft are observed (Fig. 3c). The flow pattern created by the lower impeller and middle impeller agree with the findings reported by Hudcova and Rutherford [35, 36], which is known as the merging flow created by two vortices with opposite directions of rotation. On the other hand, the upper impeller poorly interacts with the middle one, very likely due to the short distance from the free surface to the upper impeller.

When comparing the sets of impellers, larger high-velocity regions are created by RTs. However, quasi-stagnant regions exhibiting poor interaction with the rest of the tank are also observed. This phenomenon could be even more noticeable with higher-viscosity fluids. It is well known that radial flow impellers such as RTs are prone to create well-mixed
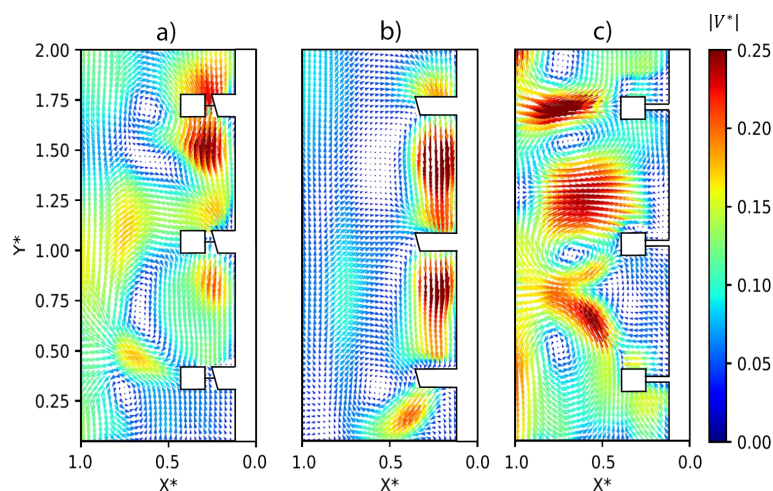
regions (caverns) leading to unhomogenized products [37], which result from a poor interaction with the rest of the vessel. Under these conditions, although lower velocity magnitudes were obtained with mixed flow impellers, a better flow distribution throughout the tank was observed. This suggests that these mixed flow impellers (ARIs) could be an attractive alternative for two-phase flows with more viscous liquid phases.

3.2   Vertical Velocity

One parameter that can be extracted from the flow fields shown in the previous section are the vertical currents induced in the tank. These currents transport the fluid from the bottom to the top of the tank and vice versa. The ideal case occurs when high-velocity downdrafts and updrafts are uniformly distributed throughout the tank to guarantee efficient mixing.

Fig. 4 shows the vertical velocity maps generated by the sets of impellers in the *X-Y* plane. The color scale shows the vertical
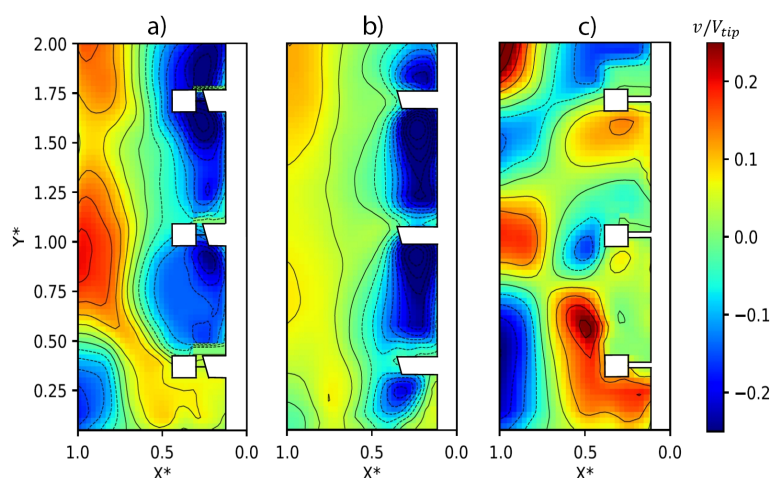
Figure 4. Vertical velocity maps in the *X-Y* plane. (a) ARIs. (b) PBTs. (c) RTs.

velocity normalized by impeller tip velocity. In general, as Figs. 4a and c show, both the ARIs and RTs, respectively, are capable of inducing high downdrafts and updrafts, unlike the PBTs, which just create high downdrafts. The high updrafts formed by the ARIs and RTs can be due to the radial jets that both sets of impellers produce. On the other hand, the vertical currents induced by ARIs are larger in magnitude and extent than those created by the RTs, which suggests a more uniform flow distribution when using mixed flow impellers.

Regarding the PBTs, because they are operated in the down-pumping mode, weak updrafts are observed as well as quasi-stagnant regions close to the tank walls. Under these conditions, the potential use of these impellers in fermentation processes will indeed be a drawback because of the poor interaction of the flow discharged by these impellers with the rest of the tank. Finally, RTs create some local well-mixed regions, which are known as caverns, but also some stagnant zones near the shaft are observed.

To further analyze this behavior, Fig. 5 shows the vertical velocity profiles as a function of the radial distance at several vertical positions corresponding to the locations where the impellers have an immediate interaction with the surrounding fluid. As shown in Fig. 5a, ARIs generate both updrafts and downdrafts. These currents are conveniently distributed in the horizontal direction, which would lead to consider shorter mixing time.

In the case of PBTs (Fig. 5b), weak updrafts are noticed, which could increase the mixing time. Finally, as Fig. 5c shows, RTs create quasi-stagnant regions between the vessel bottom and the lower turbine, which is a consequence mainly of the radial flow discharged by such impellers.

Both vertical velocity maps and profiles reveal that hybrid impellers exhibit a better performance compared to pure axial flow impellers (PBTs) and radial flow impellers (RTs), due to the uniform distribution of the flow throughout the tank.

3.3 Turbulent Intensity

Fig. 6 shows the turbulent intensity (agitation intensity) maps generated by the sets of impellers in the X-Y plane. The color scale shows the turbulent intensity (TI). As Fig. 6 shows, as impellers rotate, the fluid is accelerated when exiting the blades, so that the highest velocity fluctuations are observed near the impeller tips. When comparing the investigated impellers, the highest values were obtained with ARIs. On the other hand, the TI regions are better distributed for the ARIs and PBTs (Fig. 6a and b, respectively) compared with the TI maps of the RTs (Fig. 6c). This occurred because both the ARIs and PBTs were operated in the down-pumping mode, which causes strong intersection of currents of both phases leading to large velocity gradients, which in turn cause an increase in the velocity fluctuations through the tank.

Moreover, an important piece of information that TI maps provides is the capacity of the impellers to transfer energy to the fluid. In this sense, it would be reasonable to think that more energy could be transferred to the fluid when using ARIs, resulting in a more homogenous mixing compared with the other two sets of impellers. However, such a better energy
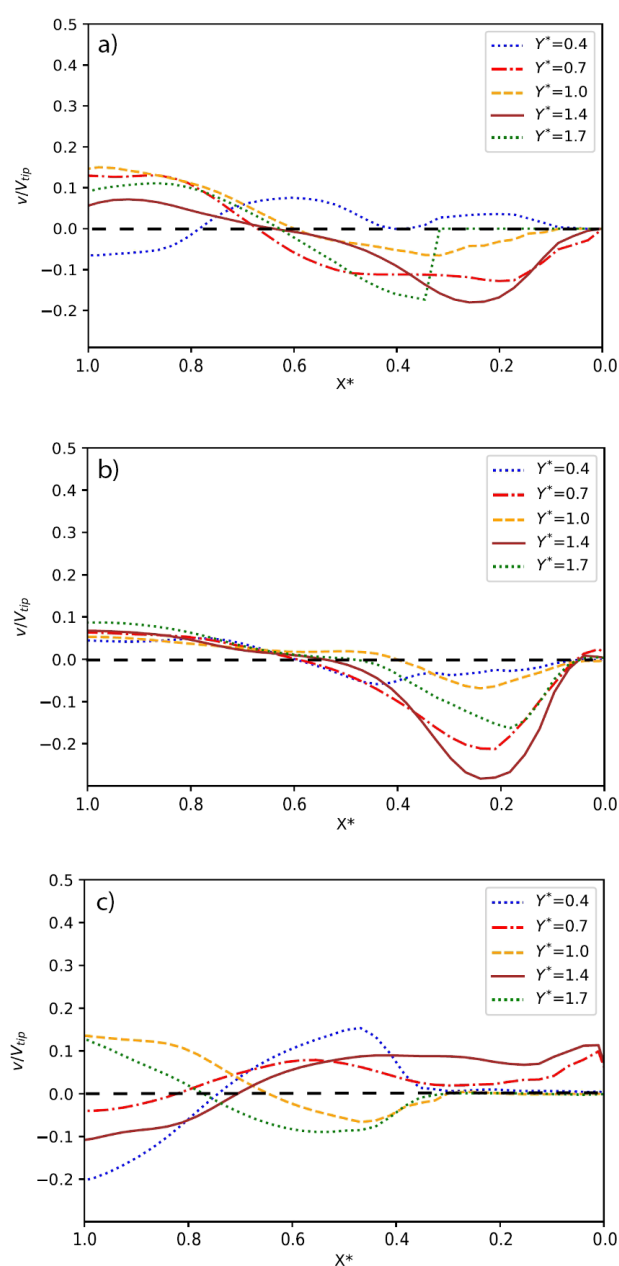
Figure 5. Vertical velocity profiles in the X-Y plane. (a) ARIs. (b) PBTs. (c) RTs.

transfer capacity will result in higher power demand when using mixed flow impellers.

On the other hand, high TI leads to high energy dissipation, which can be linked to high strain rates resulting in fragmentation of and damage to cells. Therefore, the TI is of utmost importance for the mixing of biological media [38–40]. The TI is mainly a function of the rotational speed and the impeller geometry. In this sense, it is difficult to determine whether an impeller will be suitable or not for certain biological media, because no explicit information about TI ranges causing cell damage has been reported in the literature. However, from a qualitative standpoint, some suggestions can be made. In the

present case, the RTs exhibit the lowest agitation intensity throughout the tank according to their TI contours. Therefore, this set of impellers could be suitable for biological media requiring low AI [41, 42]. On the contrary, both ARIs and the PBTs can be an alternative for biological media that tolerate high AI [43].

3.4 Strain Rate

Fig. 7 shows the strain rate maps generated by the sets of impellers in the *X-Y* plane. The color scale shows the strain rates normalized by $2V_{tip}/T$. As expected, the highest strain rates for all the impellers investigated were generated around the blades. Moreover, the highest values correspond to RTs followed by ARIs, and PBTs, which are strongly related to the velocity gradients created by each set of impellers as well as the velocity magnitude of their vortices. On the other hand, it is well known that bubbles are readily broken when subjected to high strain rates [44, 45], which in this case will be reached more easily when agitating with RTs. As bubbles are broken, their size is reduced, so that the contact surface of the bulk gas increases resulting in an improved mass transfer capacity.

Thus, the strain rate can be considered to be a key parameter when selecting impellers for a particular biological medium. Impellers generating high strain rates could be a drawback when working with shear-sensitive biological media [46, 47]. In this case, the three sets of impellers operate in a shear rate ranging from 0 to $35\,s^{-1}$ (0–2.5 in dimensionless form). For instance, some cultures can decrease their cell performance if they exceed strain rates greater than $30\,s^{-1}$ [48], so that RTs may not be the best option, because they exceed such a limit in large regions. An alternative in this case could be both ARIs and PBTs, considering that strain rates of the order of $35\,s^{-1}$ appear only in the vicinity of their blades.

On the other hand, the maximum cell concentration for some cultures is obtained at shear rates from 20 to $30\,s^{-1}$ [49, 50]. In this case, ARIs would be an attractive alternative, since they operate mainly at strain rates ranging from 20 to $30\,s^{-1}$ (1.5–2.2 in dimensionless form), unlike RTs or PBTs, which operate mainly above or below such a range, respectively.

Finally, Tab. 2 shows the specific power P/V_o and the pumping number attained by the of sets impellers at the same Reynolds number. Although the maximum power drawn corresponds to the ARIs, they provide the maximum pumping capacity. It is worth noting that, although PBTs and RTs consume less power, they provide less pumping capacity in terms of the pumping number, probably because they discharge the flow in one direction only.
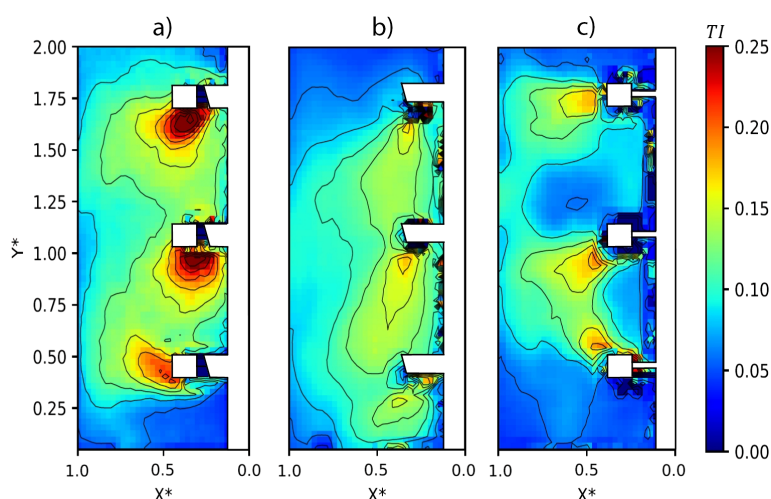
Figure 6. TI maps in the *X-Y* plane. (a) ARIs. (b) PBTs. (c) RTs.
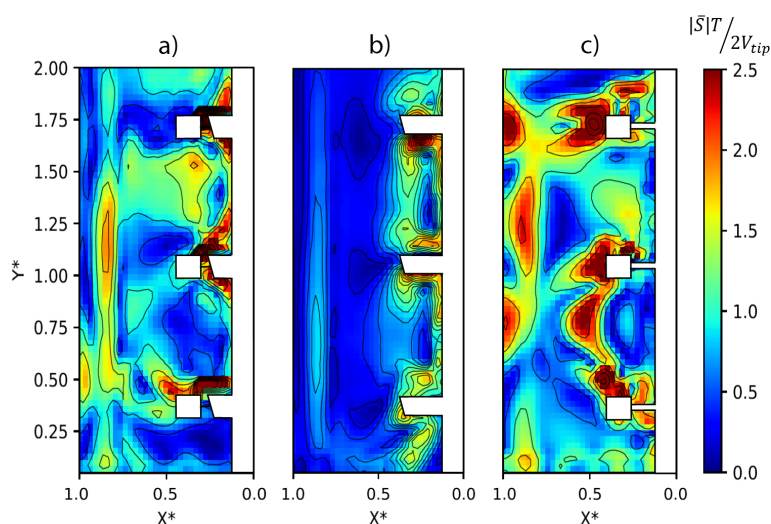
Figure 7. Strain rate maps in the *X-Y* plane. (a) ARIs. (b) PBTs. (c) RTs.

Table 2. Specific power and pumping number for ARIs, PBTs, and RTs at $N = 400$ rpm and 0.25 vvm.

Impeller	Re [–]	P/V_o [–]	N_q [–]
ARIs	5276	0.242	0.99
PBTs	5276	0.172	0.91
RTs	5276	0.193	0.88

4 Conclusion

A hydrodynamic study was performed with the aim of evaluating an array of multiple hybrid impellers in a gas-liquid system. For comparison purposes, flow fields were obtained by the PIV technique, and two different sets of impellers providing radial or axial flow were evaluated. Results for the combination of

tilted and straight blades showed that, although the hybrid impellers draw more power, they eliminate quasi-static flow zones that are created by the other two sets of impellers, resulting in better pumping, better agitation intensity through the tank, and moderate strain rates, which are beneficial for mixing some biological media having shear-sensitive cultures. On the other hand, the performance of the hybrid impellers can be further improved by redesigning the hybrid impeller so that it can be operated in a wide range of applications, mainly in fermentation processes.

Supporting Information

Supporting Information for this article can be found under DOI: https://doi.org/10.1002/ceat.202100521.

Acknowledgment

Symbols used

C_1	[m]	distance between sparger and lower impeller
C_2	[m]	distance between lower impeller and middle impeller
C_3	[m]	distance between middle impeller and upper impeller
C_4	[m]	distance between upper impeller and the free surface
D_I	[m]	impeller diameter
D_s	[m]	sparger diameter
H	[m]	liquid height
h_s	[m]	distance of the sparger from the tank bottom
J	[m]	baffle width
M	[N m]	effective torque
N	[rps]	rotational speed
N_q	[–]	pumping number
P	[W]	power consumption by the impellers
P/V	[W m^{-3}]	specific power
Q	[L min^{-1}]	gas flow rate
Q_v	[m^{3}s^{-1}]	total volumetric flow rate
Re	[–]	Reynolds number
$|\bar{s}|$	[s^{-1}]	modulus of strain rate tensor
S_{ij}	[s^{-1}]	strain rate tensor
T	[m]	tank diameter
TI	[–]	turbulent intensity
u	[m s^{-1}]	horizontal component velocity
u'	[m s^{-1}]	fluid velocity fluctuation in the horizontal direction
v	[m s^{-1}]	vertical component velocity
v'	[m s^{-1}]	fluid velocity fluctuation in the vertical direction
V_o	[m^3]	operating volume
V_{tip}	[m s^{-1}]	impeller tip velocity
$|V|$	[m s^{-1}]	velocity magnitude
$|V^*|$	[–]	normalized velocity magnitude
vvm	[min^{-1}]	volume of gas per volume of liquid per minute
X^*	[–]	dimensionless horizontal position
Y^*	[–]	dimensionless vertical position

Greek letters

μ	[mPa s]	dynamic viscosity
ρ	[kg m^{-3}]	fluid density

Abbreviations

ARI	axial-radial impeller
PBT	pitched blade turbine
PIV	particle image velocimetry
RT	Rushton turbine

References

[1] Y. Liu, J. Guo, W. Li, W. Li, J. Zhang, *Chem. Eng. J.* **2021**, *411*, 128580. DOI: https://doi.org/10.1016/j.cej.2021.128580

[2] G. Forte, F. Alberini, M. Simmons, H. E. Stitt, *J. Intell. Manuf.* **2021**, *32*, 633–647. DOI: https://doi.org/10.1007/s10845-020-01611-z

[3] F. Yang, H. Sun, C. Zhang, *Chem. Eng. Technol.* **2020**, *43 (7)*, 1297–1307. DOI: https://doi.org/10.1002/ceat.201900651

[4] X. Guan, X. Li, N. Yang, M. Liu, *Chem. Eng. J.* **2020**, *386*, 121554. DOI: https://doi.org/10.1016/j.cej.2019.04.134

[5] D. J. Karst, E. Serra, T. K. Villiger, M. Soos, M. Morbidelli, *Biochem. Eng. J.* **2016**, *110*, 17–26. DOI: https://doi.org/10.1016/j.bej.2016.02.003

[6] S. S. de Jesus, J. Moreira Neto, R. Maciel Filho, *Biochem. Eng. J.* **2017**, *118*, 70–81. DOI: https://doi.org/10.1016/j.bej.2016.11.019

[7] A. Kazemzadeh, C. Elias, M. Tamer, F. Ein-Mozaffari, *Bioprocess Biosyst. Eng.* **2018**, *41*, 679–695. DOI: https://doi.org/10.1007/s00449-018-1902-7

[8] S. T. You, A. A. A. Raman, R. S. S. R. E. Shah, M. I. M. Nor, *Rev. Chem. Eng.* **2014**, *30*, 323–336. DOI: https://doi.org/10.1515/revce-2013-0028

[9] Z. Davis, *M.Sc. Thesis*, Utah State University, Logan, UT **2009**.

[10] W. Nienow, *Chem. Eng. Res. Des.* **1996**, *74 (4)*, 417–423.

[11] C. M. Mcfarlane, A. W. Nienow, *Biotechnology* **1995**, *11*, 601–607. DOI: https://doi.org/10.1021/bp00036a001

[12] D. Hari-Prajitno, V. P. Mishra, K. Takenaka, W. Bujalski, A. W. Nienow, J. McKemmie, *Can. J. Chem. Eng.* **1998**, *76*, 1056–1068. DOI: https://doi.org/10.1002/cjce.5450760612

[13] J. Aubin, P. Mavros, D. F. Fletcher, J. Bertrand, C. Xuereb, *Chem. Eng. Res. Des.* **2001**, *79 (8)*, 845–856. DOI: https://doi.org/10.1205/02638760152721046

[14] G. Ascanio, S. Foucault, P. A. Tanguy, *Chem. Eng. Technol.* **2003**, *26*, 908–911. DOI: https://doi.org/10.1002/ceat.200301652

[15] L. Pakzad, F. Ein-Mozaffari, S. R. Upreti, A. Lohi, *Chem. Eng. J.* **2013**, *215–216*, 279–296. DOI: https://doi.org/10.1016/j.cej.2012.10.060

[16] L. Pakzad, F. Ein-Mozaffari, S. R. Upreti, A. Lohi, *Chem. Eng. Res. Des.* **2013**, *91*, 1715–1724. DOI: https://doi.org/10.1016/j.cherd.2013.02.027

[17] L. Pakzad, F. Ein-Mozaffari, S. R. Upreti, A. Lohi, *Chem. Eng. J.* **2013**, *215–216*, 279–296. DOI: https://doi.org/10.1016/j.cej.2012.10.060

[18] R. Chhabra, J. Richardson, *Non-Newtonian Flow in the Process Industries*, 1st ed., Butterworth-Heinemann, Oxford **1999**.

[19] J. Ottino, *The Kinematics of Mixing: Stretching, Chaos, and Transport*, 1st ed., Cambridge University Press, Cambridge **1989**.

[20] Y. Q. Cui, W. J. Okkerse, R. G. J. M. Van Der Lans, K. C. A. M. Luyben, *Biotechnol. Bioeng.* **1998**, *60*, 216–229. DOI: https://doi.org/10.1002/(SICI)1097-0290(19981020)60:2<216::AID-BIT9>3.0.CO;2-Q

[21] P. Ayazi Shamlou, H. Y. Makagiansar, A. P. Ison, M. D. Lilly, C. R. Thomas, *Chem. Eng. Sci.* **1994**, *49*, 2621–2631. DOI: https://doi.org/10.1016/0009-2509(94)E0079-6

[22] A. W. Nienow, *Chem. Ing. Tech.* **2021**, *93*, 17–30. DOI: https://doi.org/10.1002/cite.202000176

[23] A. Prokop, R. K. Bajpai, *Adv. Appl. Microbiol.* **1992**, *37*, 165–232. DOI: https://doi.org/10.1016/S0065-2164(08)70255-7

[24] J. A. Sánchez Pérez, E. M. Rodríguez Porcel, J. L. Casas López, J. M. Fernández Sevilla, Y. Chisti, *Chem. Eng. J.* **2006**, *124 (1–3)*, 1–5. DOI: https://doi.org/10.1016/j.cej.2006.07.002

[25] M. Rodríguez-Monroy, E. Galindo, *Microb. Technol.* **1999**, *24*, 687–693. DOI: https://doi.org/10.1016/S0141-0229(99)00002-2

[26] G. Ascanio, B. Castro, E. Galindo, *Chem. Eng. Res. Des.* **2013**, *82*, 1282–1290. DOI: https://doi.org/10.1205/cerd.82.9.1282.44164

[27] E. L. Paul, V. A. Atiemo-Obeng, S. M. Kresta, *Handbook of Industrial Mixing: Science and Practice*, John Wiley & Sons, Hoboken, NJ **2004**.

[28] www.dantecdynamics.com/solutions-applications/solutions/fluid-mechanics/particle-image-velocimetry-piv/ (Accessed on March 10, 2021)

[29] A. Hidalgo-Millán, E. Soto, R. Zenit, G. Ascanio, *Can. J. Chem. Eng.* **2011**, *89*, 1051–1058. DOI: https://doi.org/10.1002/cjce.20604

[30] A. Abdella, F. Segato, M. R. Wilkins, *Biotechnol. Rep.* **2020**, *26*, e00457. DOI: https://doi.org/10.1016/j.btre.2020.e00457

[31] L. Shu, M. Yang, H. Zhao, T. Li, L. Yang, X. Zou, Y. Li, *J. Cleaner Prod.* **2019**, *230*, 1074–1084. DOI: https://doi.org/10.1016/j.jclepro.2019.05.083

[32] R. Czinkóczky, Á. Németh, *Biochem. Eng. J.* **2020**, *163*, 107719. DOI: https://doi.org/10.1016/j.bej.2020.107719

[33] A. L. Valdez, O. D. Delgado, J. I. Fariña, *Carbohydr. Polym.* **2021**, *260*, 117505. DOI: https://doi.org/10.1016/j.carbpol.2020.117505

[34] M. Xie, J. Xia, Z. Zhou, J. Chu, Y. Zhuang, S. Zhang, *Ind. Eng. Chem. Res.* **2014**, *53*, 5941–5953. DOI: https://doi.org/10.1021/ie400831s

[35] V. Hudcova, V. Machon, A. W. Nienow, *Biotechnol. Bioeng.* **1989**, *34*, 617–628. DOI: https://doi.org/10.1002/bit.260340506

[36] K. Rutherford, K. C. Lee, S. M. S. Mahmoudi, M. Yianneskis, *AIChE J.* **1996**, *42*, 332–346. DOI: https://doi.org/10.1002/aic.690420204

[37] Y. Hirata, A. W. Nienow, I. P. T. Moore, *J. Chem. Eng. Jpn.* **1994**, *27*, 235–237. DOI: https://doi.org/10.1252/jcej.27.235

[38] A. Amanullah, P. Jüsten, A. Davies, G. C. Paul, A. W. Nienow, C. R. Thomas, *Biochem. Eng. J.* **2000**, *5*, 109–114. DOI: https://doi.org/10.1016/S1369-703X(99)00059-5

[39] A. Mitard, J. Riba, *Biotechnol Bioeng.* **1998**, *32*, 835–840. DOI: https://doi.org/10.1002/bit.260320617

[40] M. An, S. Yang, H. Wu, G. Luo, M. Li, *Environ. Sci. Pollut. Res.* **2007**, *27*, 26473–26483. DOI: https://doi.org/10.1007/s11356-020-08700-9

[41] S. Kelly, L. H. Grimm, J. Hengstler, E. Schultheis, R. Krull, D. C. Hempel, *Bioprocess Biosyst. Eng.* **2004**, *26*, 315–323. DOI: https://doi.org/10.1007/s00449-004-0368-y

[42] W. Hu, C. Berdugo, J. J. Chalmers, *Cytotechnology* **2011**, *63*, 445–460. DOI: https://doi.org/10.1007/s10616-011-9368-3

[43] P. Jüsten, G. C. Paul, A. W. Nienow, C. R. Thomas, *Biotechnol. Bioeng.* **1996**, *52*, 672–684. DOI: https://doi.org/10.1002/(SICI)1097-0290(19961220)52:6<672::AID-BIT5>3.0.CO;2-L

[44] J. Min, Y. Bao, L. Chen, Z. Gao, J. M. Smith, *Ind. Eng. Chem. Res.* **2008**, *47*, 7112–7117. DOI: https://doi.org/10.1021/ie800490j

[45] W. Kracht, J. A. Finch, *Int. J. Miner. Process.* **2009**, *92*, 153–161. DOI: https://doi.org/10.1016/j.minpro.2009.03.011

[46] R. Verma, L. Mehan, R. Kumar, A. Kumar, A. Srivastava, *Biochem. Eng. J.* **2019**, *151*, 107312. DOI: https://doi.org/10.1016/j.bej.2019.107312

[47] A. W. Nienow, in *Encyclopedia of Industrial Biotechnology* (Ed: M. C. Flickinger), John Wiley & Sons, Hoboken, NJ **2010**, 1–12. DOI: https://doi.org/10.1002/9780470054581.eib636

[48] A. Wecker, U. Onken, *Biotechnol. Lett.* **1991**, *13*, 155–160. DOI: https://doi.org/10.1007/BF01025810

[49] J. J. Zhong, K. Fujiyama, T. Seki, T. Yoshida, *Biotechnol. Bioeng.* **1994**, *44*, 649–654. DOI: https://doi.org/10.1002/bit.260440512

[50] S. Raposo, M. E. Lima-Costa, *Biotechnol. Lett.* **2006**, *28*, 431–438. DOI: https://doi.org/10.1007/s10529-005-6181-0

Appendix C
Submitted article*

This is an automated message.

Manuscript Number: HYDROM-D-22-00286

Power Characteristics and Mass Transfer of Rotor-Injectors in a Water Physical Model of an Aluminum Degassing Ladle

Dear Prof. Ascanio,

The above referenced manuscript will be handled by Editor in Chief Dr Gamini Senanayake .

To track the status of your manuscript, please log into Editorial Manager at https://www.editorialmanager.com/hydrom/.

Thank you for submitting your work to this journal.

Kind regards,

Hydrometallurgy

Hydrometallurgy

Power Characteristics and Mass Transfer of Rotor-Injectors in a Water Physical Model of an Aluminum Degassing Ladle
--Manuscript Draft--

Manuscript Number:	HYDROM-D-22-00286
Article Type:	Research Paper
Keywords:	Aluminum; Mass transfer; Power consumption; Rotor-injector; Water physical model
Corresponding Author:	Gabriel Ascanio MEXICO
First Author:	Gabriel Ascanio
Order of Authors:	Gabriel Ascanio
	David Israel Posadas-Navarro
	Carlos González Rivera
	Marco Aurelio Ramírez-Argáez
Abstract:	Abstract A comparative experimental study of a physical model of a stirred ladle for a rotor-injector aluminum degassing system in the turbulent regime has been carried out. The work aims to better understand the degassing operation in molten aluminum through a quantitative analysis by evaluating the power consumption and mass transfer capacity in a water physical model employing the typical methods used in mechanically stirred tanks. Three rotor injector devices were compared, including two conventional designs and one new rotor design. The rotors were evaluated as a function of the rotational speed and gas flow rates. The conventional rotors exhibited similar performance, while the new design consumed more power when operating at high gassing flow rates and rotational speeds resulting in a higher breakup rate of bubbles and promoting a better formation of tiny bubbles, which are better distributed over the entire ladle. This behavior avoids bubbles rising freely to the free surface; so that the gas hold-up increases leading to an improved mass transfer capacity when using this rotor. The results reported in this work agreed with previously reported works in the literature. Highlights Power drawn and mass transfer were evaluated for the first time in rotors-injectors. A typical approach as used in stirred vessels allowed evaluating the devices. Vortices created below the devices strongly affect the power consumption. Results of power consumption and mass transfer have been linked to each other.
Suggested Reviewers:	Taewook Kang twkang@sogang.ac.kr Prof. Kang has recently published a paper dealing with the determination of the mass transfer coefficient in gas-liquid reactors.

Cover Letter

May 18, 2022

Prof. Gamini Senanayake

Editor-in-Chief Hydrometallurgy

Murdoch University

Murdoch, Australia

Dear Prof. Senanayake,

Please find attached the file containing the paper entitled "Power Characteristics and Mass Transfer of Rotor-Injectors in a Water Physical Model of an Aluminum Degassing Ladle" by D.I. Posadas-Navarro, C. González-Rivera, M.A. Ramírez-Argáez and G. Ascanio, to be considered for publication in Hydrometallurgy. This manuscript deals with an experimental study of a physical model of a stirred ladle for a rotor-injector aluminum degassing system in the turbulent regime. Results of the present study are used for the removal of impurities, which is one of the topics covered in the journal. The present paper has been prepared according to the guidelines.

Sincerely

Dr. Gabriel Ascanio

Corresponding author

gabriel.ascanio@icat.unam.mx

Highlights

- The power consumption of three rotor injectors was evaluated quantitatively.

- The mass transfer capacity of three rotor injectors was evaluated quantitatively.

- Results of power consumption and mass transfer capacity are linked to each other.

- Power consumption of the rotors is a function of the vortex created below of them.

- Power consumption and mass transfer were evaluated for the first time in rotors.

Power Characteristics and Mass Transfer of Rotor-Injectors in a Water Physical Model of an Aluminum Degassing Ladle

David Israel Posadas-Navarro[a], Carlos González-Rivera[b],
Marco Aurelio Ramírez-Argáez[b], Gabriel Ascanio[a,*]

[a]Instituto de Ciencias Aplicadas y Tecnología, Universidad Nacional Autónoma de México, Circuito Exterior S/N, Ciudad Universitaria, 04510, Ciudad de México, México.

[b]Universidad Nacional Autónoma de México, Departamento de Ingeniería Metalúrgica, Facultad de Química, Edificio D, Circuito de los Institutos S/N, Ciudad Universitaria, Coyoacán, 04510 Ciudad de México, México.

Corresponding Author
*E-mail: gabriel.ascanio@icat.unam.mx

Highlights

- Power drawn and mass transfer were evaluated for the first time in rotors-injectors.

- A typical approach as used in stirred vessels allowed evaluating the devices.

- Vortices created below the devices strongly affect the power consumption.

- Results of power consumption and mass transfer have been linked to each other.

Abstract: A comparative experimental study of a physical model of a stirred ladle for a rotor-injector aluminum degassing system in the turbulent regime has been carried out. The work aims to better understand the degassing operation in molten aluminum through a quantitative analysis by evaluating the power consumption and mass transfer capacity in a water physical model employing the typical methods used in mechanically stirred tanks. Three rotor injector devices were compared, including two conventional designs and one new rotor design. The rotors were evaluated as a function of the rotational speed and gas flow rates. The conventional rotors exhibited similar performance, while the new design consumed more power when operating at high gassing flow rates and rotational speeds resulting in a higher breakup rate of bubbles and promoting a better formation of tiny bubbles, which are better distributed over the entire ladle. This behavior avoids bubbles rising freely to the free surface; so that the gas hold-up increases leading to an improved mass transfer capacity when using this rotor. The results reported in this work agreed with previously reported works in the literature.

1

Keywords
Aluminum; Mass transfer; Power consumption; Rotor-injector; Water physical model

NOMENCLATURE

C_l: oxygen concentration as a function of time, (%)
C^*: saturation oxygen concentration in the liquid phase, (%)
D: vessel's inner diameter, m
d: rotor diameter, m
Fl_g: flow number, $(-)$
H: liquid height, m
H_T: total height, m
h: height from the bottom of the tank to the rotor, m
$K_L a$: volumetric oxygen mass transfer coefficient, $1/h$
M_e: effective torque, $N \cdot m$
M_d: torque with fluid, $N \cdot m$
M_f: torque with the empty tank, $N \cdot m$
N: rotational speed, $1/s$
N_p: power number, $(-)$
N_{pg}: gassed power number, $(-)$
P: ungassed power, W
P_g: gassed power, W
Q: volumetric gas flow rate, l/min
R_e: Reynolds number, $(-)$
t: time, s
V_o: operating volume, m^3

Greek Letters
μ: dynamic viscosity, $Pa \cdot s$
ρ: fluid density, kg/m^3

Acronyms
vvm: volume of gas per volume of liquid per minute, $1/min$

2

1 Introduction

Aluminum is the most important non-ferrous metal in production processes in the world, and one of its primary uses is in the manufacture of monoblocks and pistons, in addition to essential parts in automotive engines (Anugu et al. (2021), Zhang et al. (2017)). For this reason, the aluminum must not have defects, such as impurities due to the presence of oxides or non-metallic elements, no pores or holes. These impurities influence in a negative way the physical and mechanical properties of the final product (Sigworth (1987), Zhang et al. (2011)). The harmful gas with high solubility in liquid aluminum is hydrogen and when it solidifies the hydrogen solubility dramatically decreases and then the excess of hydrogen is segregate to the interdendritic liquid and eventually a pore of hydrogen nucleates (Engh et al. (2021), Opie and Grant (1950), Sigworth (2000), Shapovalov and Kutsinskii (1989)). Due to the above, the aluminum quality depends on effectively removing hydrogen, which is a process that is carried out when aluminum is in the liquid state. For that purpose, the rotor-injector systems have been widely used (Johansen et al. (1998), Mi et al. (2009), Ni et al. (2003), Saternus and Botor (2009)). In such systems, the gas is injected through the impeller shaft while the rotor velocity promotes a large gas-liquid contact area and more residence time, improving mixing and increasing the gas removal kinetics. In this process, the rotor geometry, gas flow rate, and rotational speed (Camacho-Martínez et al. (2010), Nilmani et al. (1992), Zhang et al. (2002)), play an essential role in terms of final quality of the casting because a fast degassing kinetics depends on them.

Studies have recently been carried out on the hydrodynamic process of hydrogen degassing utilizing the particle image velocimetry technique (Mancilla et al. (2017), Mancilla et al. (2019)). In these works, the authors found that the flow patterns depend strongly on the type of rotor used in these works. As a consequence of the above, the turbulent intensity and energy dissipation rates maps showed significant differences under gassing and ungassed conditions. These hydrodynamic states dominate the kinetic and efficiency of the degassing processes. Therefore, having high turbulent intensities and high energy dissipation rates guarantees a higher gas breakup rate and promotes the formation of small bubbles that distribute over the entire ladle, which leads to an improved process.

On the other hand, the hydrogen removal rate associated with the different designs of rotors can be assessed through by the different designs of rotors can be assessed through of the mass transfer capacity, which can be studied in water physical models assuming that this kinetic is similar to the dehydrogenation of aluminum. From an experimental standpoint, the simplest and most common method for assessing the mass transfer capacity is based on dissolved hydrogen's mass balance, assuming that degassing is controlled by the mass transfer at the liquid side of the interface. Therefore, the overall volumetric mass transfer coefficient $K_L a$ can be obtained from such an approach being a combination of the mass transfer coefficient, K_L, and the interfacial area concentration, a, between dispersed gas bubbles and the molten metal (Bein et al. (2021), Whang et al. (2022)). This same method has been used in advanced metallurgical processes such as bioleaching (Barrera-Cortés et al. (2006), Boon and Heijnen (1998), Jin et al. (2010)). However, very few works dealing with numerical analysis focused on predicting the mass

transfer capacity in degassing processes have been reported in the literature (Dutta et al. (2010)). In particular, Abreu-López et al. (2018) performed a numerical study through Computational Fluid Dynamics (CFD) to predict the mass transfer capacity of four designs of rotors. The model developed allowed determining the gas hold-up and the mass transfer capacity, among other hydrodynamic parameters.

On the other hand, the momentum transfer from the rotor to the liquid is essential in degassing aluminum by promoting a better break-up of bubbles, consequently, better removal of gas trapped in the liquid phase. The classical parameter providing this information is the power consumption. On the other hand, the determination of the power consumed by rotating rotors is important not only for the calculation of the system's energy requirements but also for scaling-up processes. Some authors reported that this parameter could be obtained qualitatively using turbulent intensity maps (Posadas-Navarro et al. (2022), Mancilla et al. (2019)), which depend strongly on the velocity fluctuations inside the vessel.

To our knowledge, no works reporting the mass transfer capacity and power consumption of rotor-injector systems for degassing purposes have been found in the literature. The main objective of this paper is to characterize the performance of three different rotor-injector geometries experimentally in terms of power consumption and mass transfer capacity. For that purpose, torque and dissolved oxygen measurements were made using a rotatory torquemeter and a dissolved oxygen electrode. Results are also related to the hydrodynamic features previously reported elsewhere.

2   Materials and methods

Figure 1 shows the experimental setup used in this work. It consists of a cylindrical vessel made of glass with an inner diameter (D) of 210 mm and 480 mm height (H_T), which was used to model the process of aluminum degassing to scale. Although baffles are commonly used in stirred vessels to minimize vortexing, no baffles were considered in the present study since commercial batch processes do not consider them. The vessel was filled with tap water up to 210 mm (H), resulting in an operating volume of (V_o) 0.0072 m^3. Three different rotor-injector devices were investigated, depicted in figure 1b. The first rotor is a standard device commonly used in industry for degassing purposes consisting of a disc and lateral nozzles. The second one is also a commercial design, a rotor having nozzles and notches and the last rotor is a new design whose geometry is fully described elsewhere (Hernández-Hernández et al. (2015), Hernández-Hernández et al. (2016)). It is worth mentioning that the rotor-injector and the vessel were related with the following relationships: $d = D/3$ and $h = H/3$ being d the rotor-injector diameter and h the height measured from the bottom of the tank to the rotor-injector. Rotor-injectors were driven with a 1/4 hp CD motor Baldor Reliance having a maximum speed of 1775 rpm, coupled to a pulley-belt array with an amplification ratio of 3.45. Rotors' angular velocity was measured using a Delta CTA4 tachometer ranging from 100 to 300 rpm. Under these conditions, the flow inside the ladle was turbulent (Xie et al. (2014)). To

4

perform two-phase experiments, air was used as the gas phase supplied through the rotor shaft, a widely used method in the industry. Air was supplied at a flow rate ranging from 0.1 to 0.7 vvm. It is important to point out that vvm is a common unit used in other applications such as gas-liquid mixing to define the amount the air supplied. It stands for volume of gas per volume of liquid per minute. The airflow rate was measured with a rotameter type SHLLJ. Table 1 summarizes the experimental conditions used in the present work.

Table 1. Experimental conditions used in the present work.

Parameter	Ranges Investigated
Gas flow rates	0.1 vvm, 0.4 vvm, 0.7 vvm
Reynolds number	8.1×10^3, 1.6×10^4, 2.4×10^4
Rotational speed	100 rpm, 200 rpm, 300 rpm

The mass transfer capacity of the rotors was analyzed in terms of the volumetric mass transfer coefficient using the dynamic method reported by Garcia-Ochoa and Gomez (2009). The working fluid in the tank was deoxygenated by supplying nitrogen until reaching the oxygen saturation in the tank was equal to zero. Then, air was supplied to the tank through the agitation shaft, and the oxygen saturation was monitored by means of a polarography dissolved oxygen sensor (InPro6800) over time until reaching ninety-five percent of oxygen saturation (see figure 1a). The mathematical model describing such a process is:

$$C_l = \left(1 - e^{-k_L a \cdot t}\right) \cdot C^*$$
(1)

where C_l is the oxygen concentration in percentage of saturation, which increases over time t, C^* is the saturation oxygen concentration in the liquid phase, which is expressed as percentage of saturation and, $k_L a$ is the volumetric mass transfer coefficient. This equation describes the oxygen concentration over time from restarting aeration, therefore $k_L a$ is determined from the slope of the plot $ln\left[1 - \frac{C_l}{C^*}\right]$ vs t as is depicted in figure 2.

5
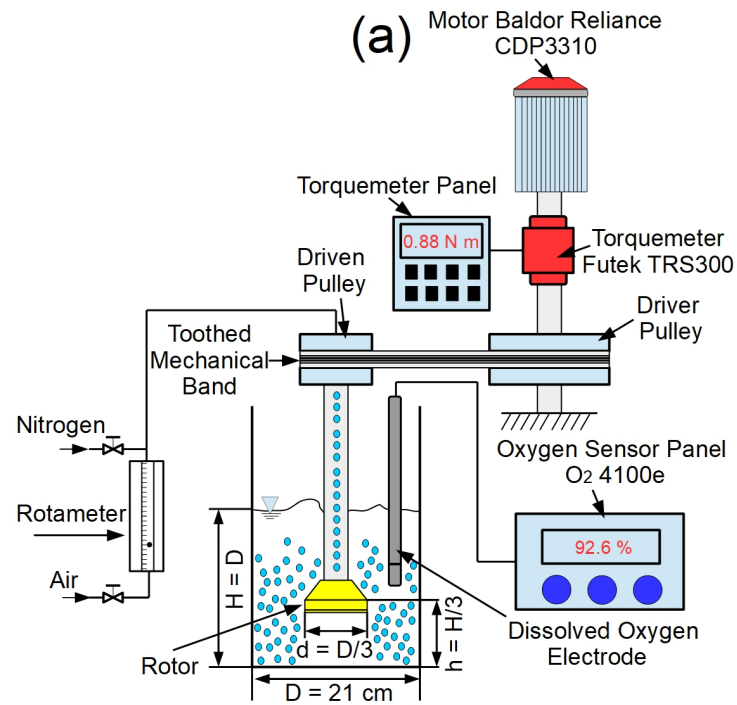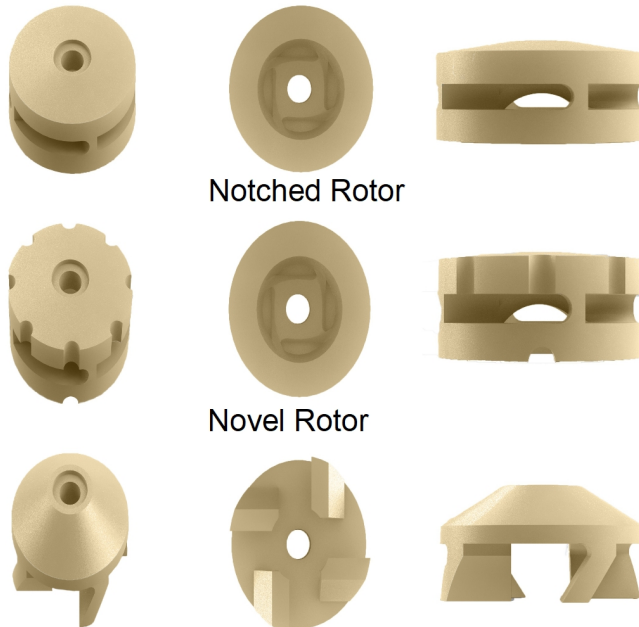
Figure 1. (a) Experimental setup, and (b) rotors-injectors used in the present work.

6
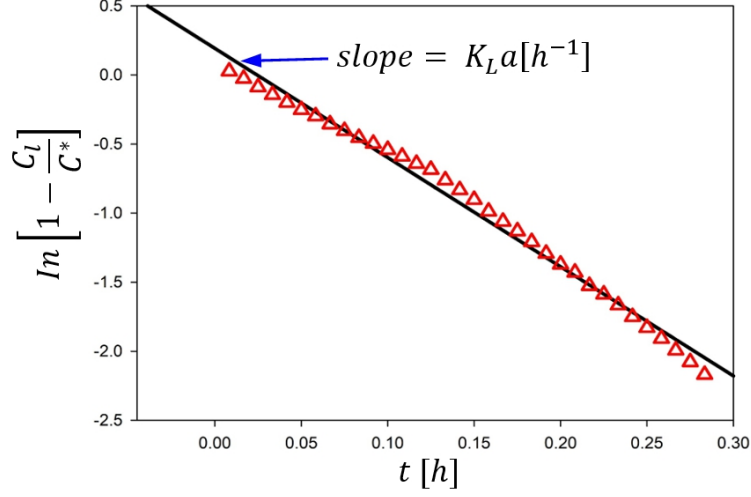
Figure 2. Schematic description of measuring the volumetric mass transfer coefficient by the classical dynamic technique.

The power drawn by the rotors was determined by measuring the torque as described elsewhere (Ascanio et al. (2004)). For that purpose, a rotary torque sensor (Futek TRS300) was coupled between the DC motor and the pulley-belt array, allowing the continuous measurement of the torque as a function of the rotation speed (see figure 1a). To measure the effective torque (M_e), the residual torque due to friction (M_f) was first measured with the empty tank. Then, the torque with the working fluid (M_d) contained in the vessel was measured. Finally, the effective torque was obtained using the following expression:

$$M_e = M_d - M_f \qquad (2)$$

and the power drawn by the impellers under gassed (P_g) and ungassed (P) conditions were calculated with the same expression:

$$P_g = P = 2\pi N M_e \qquad (3)$$

The mixing system should be characterized in terms of dimensionless numbers for scaling purpose. In the present case, the power characteristics are reported with the gassed power number (N_{pg}) and power number (N_p) as a function of the flow number (Fl_g) under gassed conditions and as a function of the Reynolds number (R_e) under ungassed conditions as follows, respectively:

$$N_{pg} = \frac{P_g}{\rho N^3 d^5} \qquad (4)$$

$$N_p = \frac{P}{\rho N^3 d^5} \qquad (5)$$

7

$$Fl_g = \frac{Q}{Nd^3} \tag{6}$$

$$R_e = \frac{\rho Nd^2}{\mu} \tag{7}$$

where Q, N, d, μ, and ρ are the volumetric gas flow rate, the rotational speed, rotors' diameter, the fluid dynamic viscosity, and fluid density, respectively.

3   Results and discussion

Analyzing power consumption and mass transfer capacity in an aluminum degassing ladle is fundamental to cost and process efficiency. An analogous process of the rotor-injector can be found in aerated stirred tanks systems. In these systems, the geometry of the impeller determines the degree of interaction between the fluid and the bubbles as well as the number of bubbles that are distributed into the ladle. In the present work, the power consumption and the mass transfer are obtained in the same way as in stirred tanks for comparison purposes between three types of rotors. In the following section, a description of the aforementioned parameters is presented for three different rotor-injector devices.

3.1   Power consumption

As aforementioned in the agitation processes of gas-liquid systems, the energy requirements needed to achieve a good dispersion play a vital role in the performance of these processes. In such cases, the power consumption is determined by the energy transferred by the impeller to the fluid. In general, the power consumption is highly dependent on the rotational speed. Figure 3 shows the power number as a function of the Reynolds number under ungassed conditions for the three rotors-injectors used in this work. As expected, the power number decreases with the increase in the Reynolds number. On the other hand, the power drawn by the three rotors is quite similar at high Reynolds numbers, very likely due to their similar dimensions. These results agree with the turbulent intensity maps reported by Mancilla et al. (2017), which are similar under ungassed conditions for the same rotors. However, on average, the highest power demand corresponds to the novel rotor, followed by the standard rotor; and the notched rotor. The major power drawn by the novel rotor can be attributed very likely to the design of its lower blades, which provide higher resistance to rotation.

8
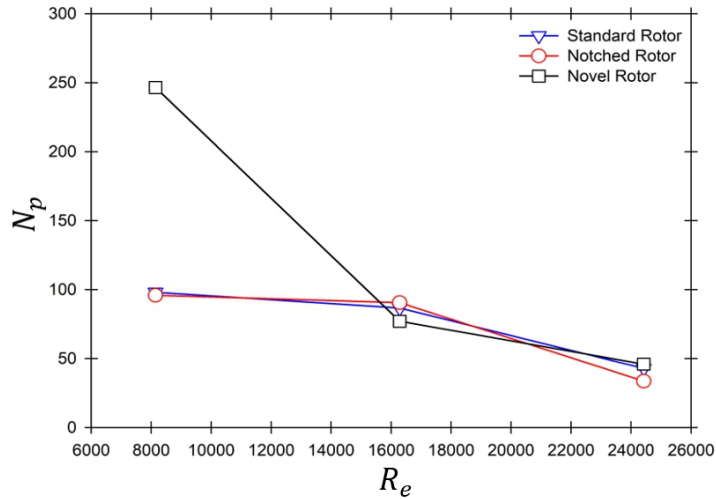
Figure 3. Power number as a function of Reynolds number for the three rotors used under ungassed conditions.

Analyzing the power consumption of rotor-injector systems under ungassed conditions is insufficient due to that the aluminum degassing process is a perfect example of a gas-liquid system. Therefore, an analysis of the power consumption under gassed conditions will provide relevant information about these processes. Figure 4 shows the power number of the three rotors-injectors used in the present work as a function of the flow number and the Reynolds numbers. As can be seen, the power number decreases as both the flow, and the Reynolds number increase. On the other hand, because less power is demanded under gassed conditions, rotors will be capable of dispersing the gas and avoiding flooding, which is vital to the process. It is worth mentioning that the gassing rates investigated in this work are quite similar to the industrial conditions, so the three geometries could be used in a real process.

On the other hand, the high-power consumption corresponds to the novel rotor when rotating at high rpm. Under these conditions, the novel rotor will generate higher turbulent intensity and transfer more energy to the continuous phase compared to the other two devices. These results agree with the findings reported elsewhere Mancilla et al. (2017). In mixing processes with unbaffled vessels, the power consumption under gassed conditions seems to be a function of the size of the vortex created by the impellers due to the deformation of the free surface (Scargiali et al. (2013), Scargiali et al. (2017)). With rotor-injector systems, the variation of the gassed power consumption also seems to be a function of the size of the vortex created below the rotor due to the gas exiting from the shaft.

As the rotational speed increases a vortex is generated just below and above the rotors. This behavior is in good agreement with the findings reported elsewhere (Abreu-López

9

et al. (2018), Hernández-Hernández et al. (2016)). As Figure 5 shows the new rotor creates larger vortices than the other two rotors, which could be a consequence of its high pumping characteristics and high power demand.
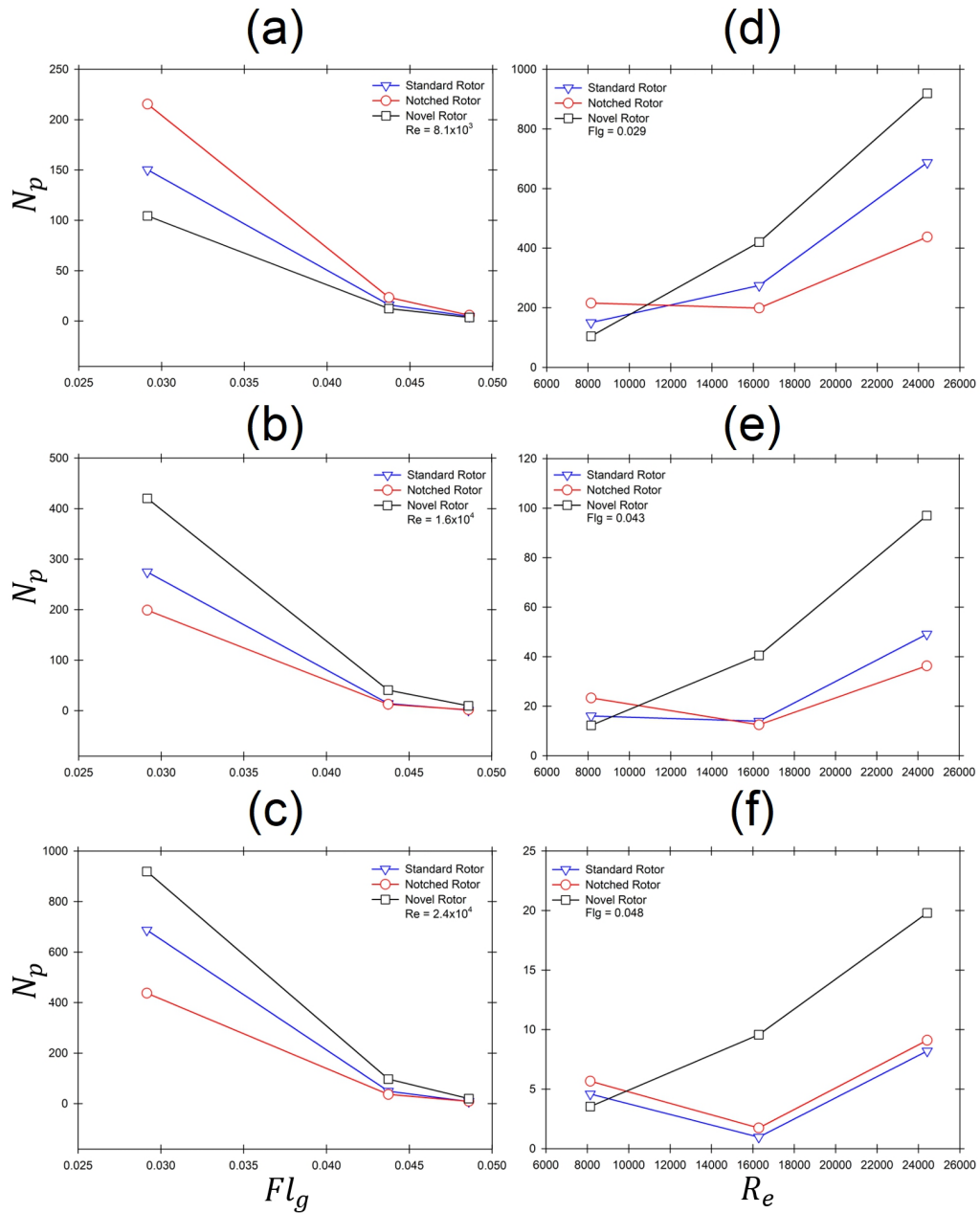
Figure 4. Power number of the rotors used in this work as a function of flow number and Reynolds number. (a) 100 rpm, (b) 200 rpm, (c) 300 rpm, (d) 0.1 vvm, (e) 0.4 vvm, (f) 0.7 vvm.

10
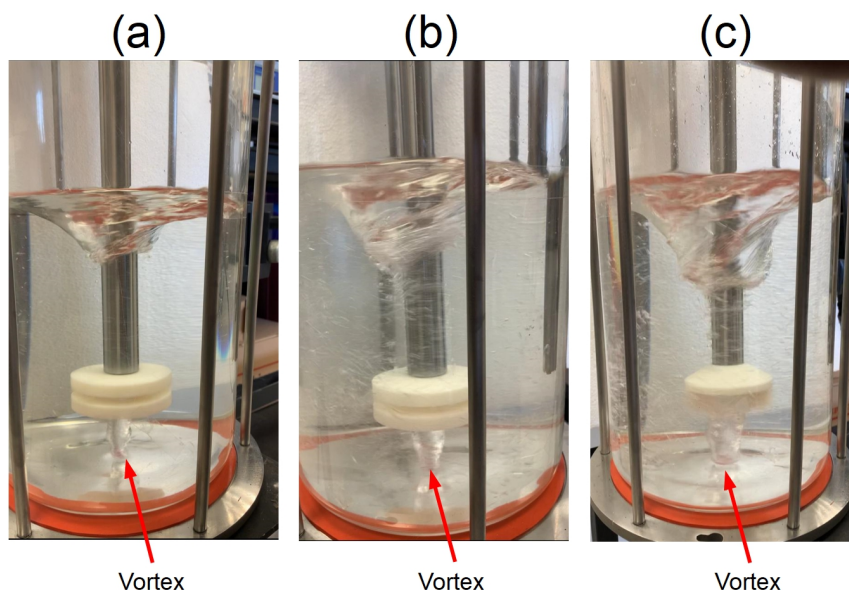
Figure 5. Photographs of the three different rotors at 300 rpm and 1 LPM. (a) standard rotor, (b) notched rotor, (c) novel rotor.

3.2 Mass transfer capacity

The analysis of the mass transfer capacity of the devices investigated will provide information on the performance of such devices in the removal of hydrogen from aluminum when supplying nitrogen or argon to the liquid phase. Figure 6 shows the volumetric mass transfer coefficient of the rotors as a function of the gas flow rate at two rotational speeds. In general, higher mass transfer coefficients are generated with the novel rotor than with the other two devices, particularly at high flow rates. This behavior can be linked to the power consumption data. The novel rotor requires more power, which leads to a better agitation of the liquid phase and better breaking of large bubbles at a faster rate, resulting in a larger contact surface and better distribution of small bubbles throughout the vessel. These results agree with those reported previously (Mancilla et al. (2017), Abreu-López et al. (2018)).

Finally, figure 7 shows the mass transfer capacity of the devices evaluated in this work in terms of the $K_L a$ as a function of the rotational speed at three different gas flow rates. As it is observed, the best mass transfer capacity is obtained with the novel rotor, particularly at high gas flow rates. On the other hand, it is clear that the volumetric mass transfer coefficient increases as both the rotational speed and the gas flow rate increases. At a fixed air flow rate, the frequency of bubble breaking increases with the rotational speed; so that more and smaller bubbles are better distributed throughout the vessel, resulting in a better mass transfer capacity. This behavior is even more noticeable when increasing the amount of air supplied. The better performance of this new device under

11

gassed conditions can be explained in terms of the flow fields combined with the excellent pumping characteristics. As the device rotates, the flow is discharged uniformly in the radial and axial directions, promoting the good dispersion of small bubbles in the vessel, resulting in a more efficient degassing process. On the other hand, according to the local analysis reported by Mancilla et al. (2017), the standard rotor and notched rotor showed a decreasing trend in the velocity magnitudes under gassed conditions, which explains their low mass transfer capacity.
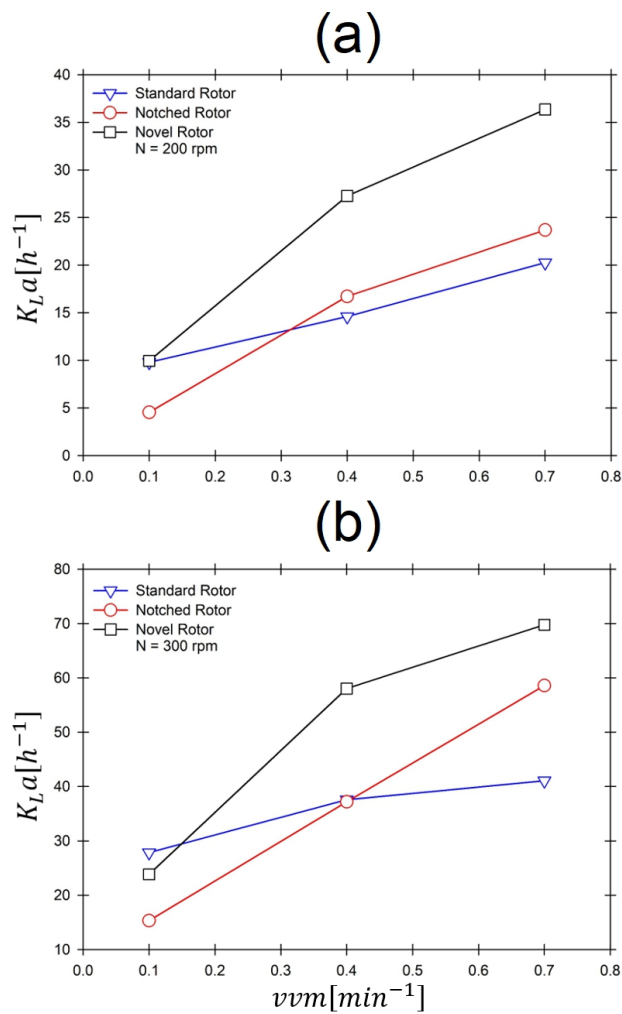

Figure 6. Volumetric mass transfer coefficient as a function of the gas flow rate for the three rotor-injector. (a) 200 rpm, (b) 300 rpm.
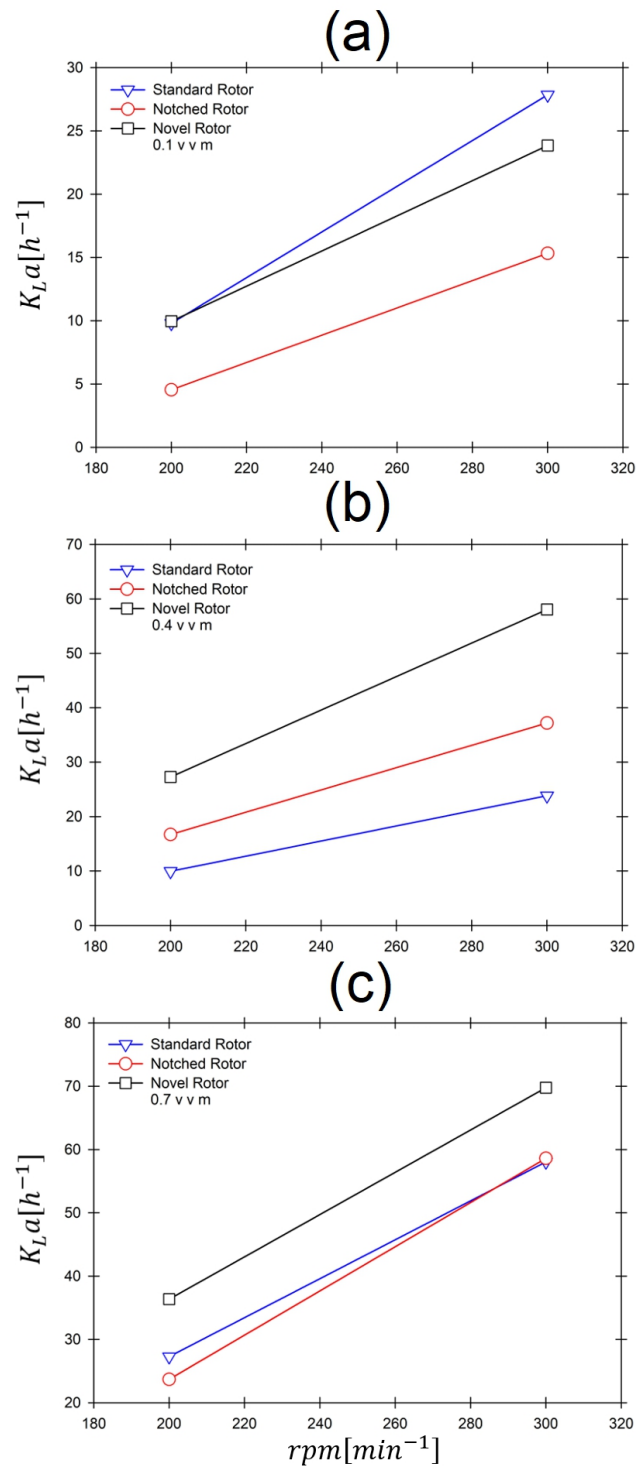
12

Figure 7. Volumetric mass transfer coefficient as a function of the rotation speed for the three rotor-injector. (a) 0.1 *vvm*, (b) 0.4 *vvm*, (c) 0.7 *vvm*.

13

4　Conclusions

The goal of this study was to compare in a way quantitative three rotor-injector by determining the power consumption and mass transfer capacity in a water physical model. A novel rotor was analyzed and compared against two commercial designs used in industrial operations. It was observed that vortices created above and below the rotors are strongly related to the power drawn, which affects the capacity of the break-up and distribution of bubbles inside the ladle resulting in a better mass transfer capacity. In mass transfer capacity terms, the devices investigated under the same operating conditions can thus be ranked as follows: 1) novel rotor (4 blades); 2) notched rotor, and 3) standard rotor. Although the power drawn by the novel rotor was higher by 28% and 53% compared to the standard and notched rotors, respectively, the mass transfer coefficient was increased about 30% and 26.8% compared with the standard and notched rotors, respectively. On the other hand, the results obtained from this work agree well with the data reported in the literature.

References

Abreu-López, D., Dutta, A., Camacho-Martínez, J. L., Trápaga-Martínez, G., and Ramírez-Argáez, M. A. (2018). Mass transfer study of a batch aluminum degassing ladle with multiple designs of rotating impellers. *JOM*, 70(12):2958–2967.

Anugu, A. R., Reddy, N. V. T., and Venkateswarlu, D. (2021). Theoritical modelling and finite element analysis of automobile piston. *Materials Today: Proceedings*, 45:1799–1803.

Ascanio, G., Castro, B., and Galindo, E. (2004). Measurement of power consumption in stirred vesselsa review. *Chemical Engineering Research and Design*, 82(9):1282–1290.

Barrera-Cortés, J., Manilla-Pérez, E., and Poggi-Varaldo, H. M. (2006). Oxygen transfer to slurries treated in a rotating drum operated at atmospheric pressure. *Bioprocess and biosystems engineering*, 29(5):391–398.

Bein, E., Zucker, I., Drewes, J. E., and Huebner, U. (2021). Ozone membrane contactors for water and wastewater treatment: A critical review on materials selection, mass transfer and process design. *Chemical Engineering Journal*, 413:127393.

Boon, M. and Heijnen, J. (1998). Gas–liquid mass transfer phenomena in bio-oxidation experiments of sulphide minerals: a critical review of literature data. *Hydrometallurgy*, 48(2):187–204.

Camacho-Martínez, J. L., Ramírez-Argáez, M. A., Zenit-Camacho, R., Juárez-Hernández, A., Barceinas-Sánchez, J. O., and Trápaga-Martínez, G. (2010). Physical modelling of an aluminium degassing operation with rotating impellersa comparative hydrodynamic analysis. *Materials and Manufacturing Processes*, 25(7):581–591.

14

Dutta, A., Ekatpure, R. P., Heynderickx, G. J., De Broqueville, A., and Marin, G. B. (2010). Rotating fluidized bed with a static geometry: Guidelines for design and operating conditions. *Chemical Engineering Science*, 65(5):1678–1693.

Engh, T. A., Sigworth, G. K., and Kvithyld, A. (2021). *Principles of Metal Refining and Recycling*. Oxford University Press.

Garcia-Ochoa, F. and Gomez, E. (2009). Bioreactor scale-up and oxygen transfer rate in microbial processes: an overview. *Biotechnology advances*, 27(2):153–176.

Hernández-Hernández, M., Camacho-Martínez, J., González-Rivera, C., and Ramírez-Argáez, M. (2016). Impeller design assisted by physical modeling and pilot plant trials. *Journal of Materials Processing Technology*, 236:1–8.

Hernández-Hernández, M., Cruz-Mendez, W., González-Rivera, C., and Ramírez-Argáez, M. (2015). Effect of process variables on kinetics and gas consumption in rotor-degassing assisted by physical and mathematical modeling. *Materials and Manufacturing Processes*, 30(2):216–221.

Jin, J., Liu, G.-L., Shi, S.-Y., and Cong, W. (2010). Studies on the performance of a rotating drum bioreactor for bioleaching processesoxygen transfer, solids distribution and power consumption. *Hydrometallurgy*, 103(1-4):30–34.

Johansen, S., Graadahl, S., Tetlie, P., Rasch, B., and Myrbostad, E. (1998). Can rotor based refining units be developed and optimized based on water model experiments. *Light Metals-Warrendale*, pages 805–810.

Mancilla, E., Cruz-Méndez, W., Garduño, I. E., González-Rivera, C., Ramírez-Argáez, M. A., and Ascanio, G. (2017). Comparison of the hydrodynamic performance of rotor-injector devices in a water physical model of an aluminum degassing ladle. *Chemical Engineering Research and Design*, 118:158–169.

Mancilla, E., Cruz-Méndez, W., Ramírez-Argáez, M. A., González-Rivera, C., and Ascanio, G. (2019). Experimental measurements of bubble size distributions in a water model and its influence on the aluminum kinetics degassing. *The Canadian Journal of Chemical Engineering*, 97:1729–1740.

Mi, G., Qi, S., Liu, X., and Niu, J. (2009). Research on water simulation experiment of the rotating impeller degassing process. *Materials Science and Engineering: A*, 499(1-2):195–199.

Ni, H., Sun, B., Jiang, H., and Ding, W. (2003). Effects of rotating impeller degassing on microstructure and mechanical properties of the a356 scraps. *Materials Science and Engineering: A*, 352(1-2):294–299.

Nilmani, M., Thay, P., and Simensen, C. (1992). A comparative study of impeller performance. *Light Metals*, pages 939–946.

Opie, W. and Grant, N. (1950). Hydrogen solubility in aluminum and some aluminum alloys. *JOM*, 2(10):1237–1241.

15

Posadas-Navarro, D., Palacios, C., Blancas-Cabrera, A., Trujillo-Roldán, M. A., Salinas-Vázquez, M., and Ascanio, G. (2022). Flow patterns of multiple axial-radial impellers for potential use in aerated stirred tanks. *Chemical Engineering & Technology*, 45(5):860–867.

Saternus, M. and Botor, J. (2009). Physical model of aluminium refining process in urc-7000. *Metalurgija*, 48(3):175–179.

Scargiali, F., Busciglio, A., Grisafi, F., Tamburini, A., Micale, G., and Brucato, A. (2013). Power consumption in uncovered unbaffled stirred tanks: Influence of the viscosity and flow regime. *Industrial & Engineering Chemistry Research*, 52(42):14998–15005.

Scargiali, F., Tamburini, A., Caputo, G., and Micale, G. (2017). On the assessment of power consumption and critical impeller speed in vortexing unbaffled stirred tanks. *Chemical Engineering Research and Design*, 123:99–110.

Shapovalov, V. I. and Kutsinskii, V. G. (1989). Solubility of hydrogen in liquid molybdenum. *Russian metallurgy. Metally*, 4(3):185–187.

Sigworth, G. (1987). A scientific basis for degassing aluminum. *AFS transactions*, 95:73–78.

Sigworth, G. K. (2000). Gas fluxing of molten aluminum. *Light Metals*, pages 773–778.

Whang, K., Shin, Y., Baek, W., Jo, Y., Hwang, J. H., Min, J., Kim, D., and Kang, T. (2022). Direct and precise determination of volumetric mass transfer coefficient of carbon monoxide for miniaturized gas-liquid reactors via sensitive probing of raman transitions. *Chemical Engineering Journal*, 429:132260.

Xie, M., Xia, J., Zhou, Z., Chu, J., Zhuang, Y., and Zhang, S. (2014). Flow pattern, mixing, gas hold-up and mass transfer coefficient of triple-impeller configurations in stirred tank bioreactors. *Industrial & Engineering Chemistry Research*, 53(14):5941–5953.

Zhang, L., Lv, X., Torgerson, A. T., and Long, M. (2011). Removal of impurity elements from molten aluminum: A review. *Mineral Processing & Extractive Metallurgy Review*, 32(3):150–228.

Zhang, L., Taniguchi, S., and Matsumoto, K. (2002). Water model study on inclusion removal from liquid steel by bubble flotation under turbulent conditions. *Ironmaking & Steelmaking*, 29(5):326–336.

Zhang, X.-l., Chi, X.-m., Zeng, B.-d., Sun, H., Chen, J.-y., and Wang, X.-f. (2017). Numerical simulation study on monoblock casting process of ultra-slender structural components and experimental validation. *China Foundry*, 14(5):449–455.

16

Conflict of interest

Title: Power Characteristics and Mass Transfer of Rotor-Injectors in a Water Physical

Model of an Aluminum Degassing Ladle

Authors: D.I. Posadas-Navarro, C. González-Rivera, M.A. Ramírez-Argáez and G. Ascanio

Date: May 19, 2022

The Authors **declare** that there is **no conflict of interests to declare**.

Bibliography

Bibliography

Abdella, A., Segato, F., and Wilkins, M. R. (2020). Optimization of process parameters and fermentation strategy for xylanase production in a stirred tank reactor using a mutant Aspergillus nidulans strain. *Biotechnology Reports*, 26(March):e00457.

Afshar Ghotli, R., Shafeeyan, M. S., Abbasi, M. R., Abdul Raman, A. A., and Ibrahim, S. (2020). Macromixing study for various designs of impellers in a stirred vessel. *Chemical Engineering and Processing - Process Intensification*, 148(September):107794.

Amer, M., Feng, Y., and Ramsey, J. D. (2019). Using CFD simulations and statistical analysis to correlate oxygen mass transfer coefficient to both geometrical parameters and operating conditions in a stirred-tank bioreactor. *Biotechnology Progress*, 35(3).

Arjunwadkar, S., Saravanan, K., Pandit, A., and Kulkarni, P. (1998). Optimizing the impeller combination for maximum hold-up with minimum power consumption. *Biochemical Engineering Journal*, 1(1):25–30.

Armenante, P. M. and Chang, G.-M. (1998). Power consumption in agitated vessels provided with multiple-disk turbines. *Industrial & engineering chemistry research*, 37(1):284–291.

Armenante, P. M., Huang, Y.-T., and Li, T. (1992). Determination of the minimum agitation speed to attain the just dispersed state in solid-liquid and liquid-liquid reactors provided with multiple impellers. *Chemical engineering science*, 47(9-11):2865–2870.

Ascanio, G., Castro, B., and Galindo, E. (2013). Measurement of Power Consumption in Stirred Vessels—A Review. 82(September 2004):1282–1290.

Ascanio, G., Foucault, S., and Tanguy, P. A. (2003). Performance of a new mixed down pumping impeller. *Chemical Engineering and Technology*, 26(8):908–911.

Aubin, J., Le Sauze, N., Bertrand, J., Fletcher, D. F., and Xuereb, C. (2004). Piv measurements of flow in an aerated tank stirred by a down-and an up-pumping axial flow impeller. *Experimental thermal and fluid science*, 28(5):447–456.

Aubin, J., Mavros, P., Fletcher, D. F., Bertrand, J., and Xuereb, C. (2001). Effect of axial agitator configuration (up-pumping, down-pumping, reverse rotation) on flow patterns generated in stirred vessels. *Chemical Engineering Research and Design*, 79(8):845–856.

Ayala, J. S., de Moura, H. L., Amaral, R. d. L., Oliveira Júnior, F. d. A., Nunhez, J. R., and de Castilho, G. J. (2022). Two-dimensional shear rate field and flow structures of a pseudoplastic fluid in a stirred tank using particle image velocimetry. *Chemical Engineering Science*, 248:117198.

Ayazi Shamlou, P., Makagiansar, H. Y., Ison, A. P., Lilly, M. D., and Thomas, C. R. (1994). Turbulent breakage of filamentous microorganisms in submerged culture in mechanically stirred bioreactors. *Chemical Engineering Science*, 49(16):2621–2631.

Bałdyga, J. and Bourne, J. R. (1999). *Turbulent mixing and chemical reactions*. Wiley.

Besbes, S., El Hajem, M., Ben Aissia, H., Champagne, J. Y., and Jay, J. (2015). PIV measurements and Eulerian-Lagrangian simulations of the unsteady gas-liquid flow in a needle sparger rectangular bubble column. *Chemical Engineering Science*, 126:560–572.

Bouaifi, M. and Roustan, M. (2001). Power consumption, mixing time and homogenisation energy in dual-impeller agitated gas–liquid reactors. *Chemical Engineering and Processing: Process Intensification*, 40(2):87–95.

Brauer, H. (1979). Power Consumption in Aerated Stirred Tank Reactor Systems. *Advances in Biochemical Engineering*, 13:87–119.

Buffo, M. M., Corrêa, L. J., Esperança, M. N., Cruz, A. J., Farinas, C. S., and Badino, A. C. (2016). Influence of dual-impeller type and configuration on oxygen transfer, power consumption, and shear rate in a stirred tank bioreactor. *Biochemical Engineering Journal*, 114.

Chapple, D., Kresta, S., Wall, A., and Afacan, A. (2002). The effect of impeller and tank geometry on power number for a pitched blade turbine. *Chemical Engineering Research and Design*, 80(4):364–372.

Cheng, D., Wang, S., Yang, C., and Mao, Z. S. (2017). Numerical Simulation of Turbulent Flow and Mixing in Gas-Liquid-Liquid Stirred Tanks. *Industrial and Engineering Chemistry Research*, 56(45):13050–13063.

Chhabra, R. P. and Richardson, J. F. (1999). *Non-Newtonian flow in the process industries: fundamentals and engineering applications*. Butterworth-Heinemann.

Cortada-Garcia, M., Weheliye, W. H., Dore, V., Mazzei, L., and Angeli, P. (2018). Computational fluid dynamic studies of mixers for highly viscous shear thinning fluids and PIV validation. *Chemical Engineering Science*, 179:133–149.

Cui, Y., Okkerse, W., Van der Lans, R., and Luyben, K. C. A. (1998a). Modeling and measurements of fungal growth and morphology in submerged fermentations. *Biotechnology and bioengineering*, 60(2):216–229.

Cui, Y. Q., Okkerse, W. J., Van Der Lans, R. G., and Luyben, K. C. A. (1998b). Modeling and measurements of fungal growth and morphology in submerged fermentations. *Biotechnology and Bioengineering*, 60(2):216–229.

Czinkóczky, R. and Németh, Á. (2020). Techno-economic assessment of Bacillus fermentation to produce surfactin and lichenysin. *Biochemical Engineering Journal*, 163.

Davis, R. Z. (2009). *Design and scale-up of production scale stirred tank fermentors*. Utah State University.

Delnoij, E., Westerweel, J., Deen, N. G., Kuipers, J. A., and Van Swaaij, W. P. (1999). Ensemble correlation PIV applied to bubble plumes rising in a bubble column. *Chemical Engineering Science*, 54(21):5159–5171.

Derksen, J. and Van Den Akker, H. E. (1999). Large eddy simulations on the flow driven by a Rushton turbine. *AIChE Journal*, 45(2):209–221.

Dickin, F. and Wang, M. (1996). Electrical resistance tomography for process applications. *Measurement Science and Technology*, 7(3):247–260.

Fitschen, J., Hofmann, S., Wutz, J., Kameke, A. V., Hoffmann, M., Wucherpfennig, T., and Schlüter, M. (2021). Novel evaluation method to determine the local mixing time distribution in stirred tank reactors. *Chemical Engineering Science: X*, 10:100098.

Forte, G., Alberini, F., Simmons, M., and Stitt, H. E. (2021a). Use of acoustic emission in combination with machine learning: monitoring of gas–liquid mixing in stirred tanks. *Journal of Intelligent Manufacturing*, 32(2):633–647.

Forte, G., Alberini, F., Simmons, M., and Stitt, H. E. (2021b). Use of acoustic emission in combination with machine learning: monitoring of gas–liquid mixing in stirred tanks. *Journal of Intelligent Manufacturing*, 32(2):633–647.

Galletti, C., Brunazzi, E., Pintus, S., Paglianti, A., and Yianneskis, M. (2004). A study of Reynolds stresses, triple products and turbulence states in a radially stirred tank

with 3-D laser anemometry. *Chemical Engineering Research and Design*, 82(9 SPEC. ISS.):1214–1228.

Ganguly, S. K., Majumder, C. B., and Ray, A. (2021). The Effect of Impeller-Sparger Geometry on the Gas Holdup in an Oxygen-Water System Using an Agitated and Sparged Tank Contactor. *Industrial and Engineering Chemistry Research*, 60(28):10445–10453.

García-Ochoa, F. and Gómez, E. (1998). Mass transfer coefficient in stirred tank reactors for xanthan gum solutions. *Biochemical Engineering Journal*, 1(1):1–10.

Garcia-Ochoa, F. and Gomez, E. (2009). Bioreactor scale-up and oxygen transfer rate in microbial processes: An overview. *Biotechnology Advances*, 27(2):153–176.

Gogate, P. and Pandit, M. (1999). Scale effect on gas hold-up characteristics in multiple-impeller fermenter. In *AIChE Spring Meeting, Houston, TX*.

Guan, X., Li, X., Yang, N., and Liu, M. (2020). Cfd simulation of gas-liquid flow in stirred tanks: Effect of drag models. *Chemical Engineering Journal*, 386:121554.

Hari-Prajitno, D., Mishra, V. P., Takenaka, K., Bujalski, W., Nienow, A. W., and Mckemmie, J. (1998). Gas—liquid mixing studies with multiple up-and down-pumping hydrofoil impellers: Power characteristics and mixing time. *The Canadian Journal of Chemical Engineering*, 76(6):1056–1068.

Hashemi, N., Ein-Mozaffari, F., Upreti, S. R., and Hwang, D. K. (2016a). Analysis of power consumption and gas holdup distribution for an aerated reactor equipped with a coaxial mixer: Novel correlations for the gas flow number and gassed power. *Chemical Engineering Science*, 151:25–35.

Hashemi, N., Ein-Mozaffari, F., Upreti, S. R., and Hwang, D. K. (2016b). Experimental investigation of the bubble behavior in an aerated coaxial mixing vessel through electrical resistance tomography (ert). *Chemical Engineering Journal*, 289:402–412.

Hashemi, N., Ein-Mozaffari, F., Upreti, S. R., and Hwang, D. K. (2018). Hydrodynamic characteristics of an aerated coaxial mixing vessel equipped with a pitched blade turbine and an anchor. *Journal of Chemical Technology & Biotechnology*, 93(2):392–405.

Hidalgo-Millán, A., Zenit, R., Palacios, C., Yatomi, R., Horiguchi, H., Tanguy, P., and Ascanio, G. (2012). On the hydrodynamics characterization of the straight maxblend® impeller with newtonian fluids. *Chemical Engineering Research and Design*, 90(9):1117–1128.

Hirata, Y., Nienow, A. W., and Moore, I. P. (1994). Estimation of Cavern Sizes in a Shear-thinning Plastic Fluid Agitated by a Rushton Turbine Based on LDA Measurements.

Hudcova, V., Machon, V., and Nienow, A. W. (1989). Gas–liquid dispersion with dual Rushton impellers. *Biotechnology and Bioengineering*, 34(5):617–628.

Issa, H. M. (2016). Power consumption, mixing time, and oxygen mass transfer in a gas-liquid contactor stirred with a dual impeller for different spacing. *Journal of Engineering*, 2016.

Jamshidzadeh, M., Kazemzadeh, A., Ein-Mozaffari, F., and Lohi, A. (2020a). Analysis of power consumption for gas dispersion in non-newtonian fluids with a coaxial mixer: New correlations for reynolds and power numbers. *Chemical Engineering Journal*, 401:126002.

Jamshidzadeh, M., Kazemzadeh, A., Ein-Mozaffari, F., and Lohi, A. (2020b). Intensification of gas dispersion in pseudoplastic fluids with coaxial mixers. *Chemical Engineering and Processing-Process Intensification*, 155:108058.

Jegatheeswaran, S. and Ein-Mozaffari, F. (2020). Investigation of the detrimental effect of the rotational speed on gas holdup in non-newtonian fluids with scaba-anchor coaxial mixer: A paradigm shift in gas-liquid mixing. *Chemical Engineering Journal*, 383:123118.

Karthikeyan, A., Joseph, A., Subramanian, R., and Nair, B. G. (2022). Fermenter design. In *Industrial Microbiology and Biotechnology*, pages 129–167. Springer.

Khalili, F., Nasr, M. J., Kazemzadeh, A., and Ein-Mozaffari, F. (2017). Hydrodynamic performance of the asi impeller in an aerated bioreactor containing the biopolymer solution through tomography and cfd. *Chemical Engineering Research and Design*, 125:190–203.

Kipke, K. (1982). Fluid loadings on impellers and tanks in gassed liquids. In *Fourth European Conference on Mixing*, pages 355–370.

Kracht, W. and Finch, J. A. (2009). Bubble break-up and the role of frother and salt. *International Journal of Mineral Processing*, 92(3-4):153–161.

Kulkarni, A. V., Roy, S. S., and Joshi, J. B. (2007). Pressure and flow distribution in pipe and ring spargers: Experimental measurements and CFD simulation. *Chemical Engineering Journal*, 133(1-3):173–186.

Kumaresan, T. and Joshi, J. B. (2006). Effect of impeller design on the flow pattern and mixing in stirred tanks. *Chemical engineering journal*, 115(3):173–193.

Lamberto, D. J., Alvarez, M. M., and Muzzio, F. J. (1999). Experimental and computational investigation of the laminar flow structure in a stirred tank. *Chemical Engineering Science*, 54(7):919–942.

Li, D. and Chen, W. (2022). Effects of impeller types on gas-liquid mixing and oxygen mass transfer in aerated stirred reactors. *Process Safety and Environmental Protection*, 158:360–373.

Li, X., Yu, G., Yang, C., and Mao, Z.-S. (2009). Experimental study on surface aerators stirred by triple impellers. *Industrial & engineering chemistry research*, 48(18):8752–8756.

Li, Z., Bao, Y., and Gao, Z. (2011). Piv experiments and large eddy simulations of single-loop flow fields in rushton turbine stirred tanks. *Chemical Engineering Science*, 66(6):1219–1231.

Liu, B., Zheng, Y., Cheng, R., Xu, Z., Wang, M., and Jin, Z. (2018). Experimental study on gas–liquid dispersion and mass transfer in shear-thinning system with coaxial mixer. *Chinese Journal of Chemical Engineering*, 26(9):1785–1791.

Liu, Y., Guo, J., Li, W., Li, W., and Zhang, J. (2021). Investigation of gas-liquid mass transfer and power consumption characteristics in jet-flow high shear mixers. *Chemical Engineering Journal*, 411:128580.

Maluta, F., Montante, G., and Paglianti, A. (2020). Analysis of immiscible liquid-liquid mixing in stirred tanks by Electrical Resistance Tomography. *Chemical Engineering Science*, 227:115898.

Mancilla, E., Yatomi, R., Zenit, R., and Ascanio, G. (2016). Hydrodynamic characterization of three axial impellers under gassed and ungassed conditions. *Journal of Chemical Engineering of Japan*, 49(10):894–903.

Mann, R., Dickin, F. J., Wang, M., Dyakowski, T., Williams, R. A., Edwards, R. B., Forrest, A. E., and Holden, P. J. (1997). Application of electrical resistance tomography to interrogate mixing processes at plant scale. *Chemical Engineering Science*, 52(13):2087–2097.

Mavros, P. (2001). Flow Visualization in Stirred Vessels. *Chemical Engineering Research and Design*, 79(2):113–127.

McFarlane, C. M. and Nienow, A. W. (1995). Studies of high solidity ratio hydrofoil impellers for aerated bioreactors. 1. review. *Biotechnology progress*, 11(6):601–607.

Min, J., Bao, Y., Chen, L., Gao, Z., and Smith, J. M. (2008). Numerical simulation of gas dispersion in an aerated stirred reactor with multiple impellers. *Industrial and Engineering Chemistry Research*, 47(18):7112–7117.

Moucha, T., Linek, V., and Prokopova, E. (2003). Gas hold-up, mixing time and gas–liquid volumetric mass transfer coefficient of various multiple-impeller configurations: Rushton turbine, pitched blade and techmix impeller and their combinations. *Chemical Engineering Science*, 58(9):1839–1846.

Murgan, I., Bunea, F., and Ciocan, G. D. (2017). Experimental PIV and LIF characterization of a bubble column flow. *Flow Measurement and Instrumentation*, 54(July 2016):224–235.

Nagata, S. (1975). Heat transfer in agitated vessel. *mixing: Principles and applications*, pages 100–02.

Nauman, E. B. (2008). *Chemical reactor design, optimization, and scaleup.* John Wiley & Sons.

Nienow, A. (1996). Gas-liquid mixing studies-a comparison of rushton turbines with some modern impellers. *Chemical engineering research & design*, 74(4):417–423.

Nienow, A. and Lilly, M. (1979). Power drawn by multiple impellers in sparged agitated vessels. *Biotechnology and Bioengineering*, 21(12):2341–2345.

Nienow, A. W. (2010). Impeller Selection for Animal Cell Culture. *Encyclopedia of Industrial Biotechnology*, (4):1–12.

Nienow, A. W. (2021a). The impact of fluid dynamic stress in stirred bioreactors–the scale of the biological entity: a personal view. *Chemie Ingenieur Technik*, 93(1-2):17–30.

Nienow, A. W. (2021b). The Impact of Fluid Dynamic Stress in Stirred Bioreactors – The Scale of the Biological Entity: A Personal View. *Chemie-Ingenieur-Technik*, 93(1-2):17–30.

Nocentini, M., Fajner, D., Pasquali, G., and Magelli, F. (1993). Gas-liquid mass transfer and holdup in vessels stirred with multiple rushton turbines: water and water-glycerol solutions. *Industrial & engineering chemistry research*, 32(1):19–26.

Ottino, J. M. and Ottino, J. (1989). *The kinematics of mixing: stretching, chaos, and transport*, volume 3. Cambridge university press.

Ozcan-Taskin, N., Nienow, A., and Chatwin, S. (1992). Les characteristiques de puissance des lntermigs et des turbines rushton dans les fluides viscoelastiques a viscosite constante. *Agitation Industrielle, J*, 11(10).

Pakzad, L., Ein-Mozaffari, F., Upreti, S. R., and Lohi, A. (2013a). Evaluation of the mixing of non-newtonian biopolymer solutions in the reactors equipped with the coaxial mixers through tomography and cfd. *Chemical engineering journal*, 215:279–296.

Pakzad, L., Ein-Mozaffari, F., Upreti, S. R., and Lohi, A. (2013b). Evaluation of the mixing of non-Newtonian biopolymer solutions in the reactors equipped with the coaxial mixers through tomography and CFD. *Chemical Engineering Journal*, 215-216:279–296.

Pakzad, L., Ein-Mozaffari, F., Upreti, S. R., and Lohi, A. (2013c). A novel and energy-efficient coaxial mixer for agitation of non-newtonian fluids possessing yield stress. *Chemical Engineering Science*, 101:642–654.

Paul, E. L., Atiemo-Obeng, V. A., and Kresta, S. M. (2003). *Handbook of industrial mixing: science and practice*, volume 1. John Wiley & Sons.

Pérez, J. S., Porcel, E. R., López, J. C., Sevilla, J. F., and Chisti, Y. (2006). Shear rate in stirred tank and bubble column bioreactors. *Chemical Engineering Journal*, 124(1-3):1–5.

Pinheiro, P. A., Loh, W. W., Wang, M., Mann, R., and Waterfall, R. C. (1999). Three-dimensional electrical resistance tomography in a stirred mixing vessel. *Chemical Engineering Communications*, 175(October 2014):25–38.

Placek, J. and Tavlarides, L. L. (1985). Turbulent flow in stirred tanks. Part I: Turbulent flow in the turbine impeller region. *AIChE Journal*, 31(7):1113–1120.

Prokop, A. and Bajpai, R. K. (1992a). The sensitivity of biocatalysts to hydrodynamic shear stress. *Advances in applied microbiology*, 37:165–232.

Prokop, A. and Bajpai, R. K. (1992b). The Sensitivity of Biocatalysts to Hydrodynamic Shear Stress. *Advances in Applied Microbiology*, 37(C):165–232.

Puthli, M. S., Rathod, V. K., and Pandit, A. B. (2005a). Gas–liquid mass transfer studies with triple impeller system on a laboratory scale bioreactor. *Biochemical engineering journal*, 23(1):25–30.

Puthli, M. S., Rathod, V. K., and Pandit, A. B. (2005b). Gas–liquid mass transfer studies with triple impeller system on a laboratory scale bioreactor. *Biochemical engineering journal*, 23(1):25–30.

Ramírez-Cruz, J., Salinas-Vázquez, M., Ascanio, G., Vicente-Rodríguez, W., and Lagarza-Córtes, C. (2020). Mixing dynamics in an uncovered unbaffled stirred tank using Large-Eddy Simulations and a passive scalar transport equation. *Chemical Engineering Science*, 222.

Rodríguez-Monroy, M. and Galindo, E. (1999). Broth rheology, growth and metabolite production of Beta vulgaris suspension culture: A comparative study between cultures grown in shake flasks and in a stirred tank. *Enzyme and Microbial Technology*, 24(10):687–693.

Rutherford, K., Lee, K. C., Mahmoudi, S. M. S., and Yianneskis, M. (1996). Hydrodynamic characteristics of dual impeller stirred reactors. *AIChE Journal*, 42(2):332–346.

Sánchez Pérez, J. A., Rodríguez Porcel, E. M., Casas López, J. L., Fernández Sevilla, J. M., and Chisti, Y. (2006). Shear rate in stirred tank and bubble column bioreactors. *Chemical Engineering Journal*, 124(1-3):1–5.

Sardeing, R., Aubin, J., and Xuereb, C. (2004). Gas–liquid mass transfer: A comparison of down-and up–pumping axial flow impellers with radial impellers. *Chemical Engineering Research and Design*, 82(12):1589–1596.

Sardeshpande, M. V., Gupta, S., and Ranade, V. V. (2017). Electrical resistance tomography for gas holdup in a gas-liquid stirred tank reactor. *Chemical Engineering Science*, 170:476–490.

Scott, D. M. and McCann, H. (2018). *Process imaging for automatic control*. CRC Press.

Shamlou, P. A., Makagiansar, H., Ison, A., Lilly, M., and Thomas, C. (1994). Turbulent breakage of filamentous microorganisms in submerged culture in mechanically stirred bioreactors. *Chemical engineering science*, 49(16):2621–2631.

Sharifi, M. and Young, B. (2013). Electrical resistance tomography (ert) applications to chemical engineering. *Chemical Engineering Research and Design*, 91(9):1625–1645.

Shu, L., Yang, M., Zhao, H., Li, T., Yang, L., Zou, X., and Li, Y. (2019). Process optimization in a stirred tank bioreactor based on CFD-Taguchi method: A case study. *Journal of Cleaner Production*, 230:1074–1084.

Uhl, V. (1966). *Mixing VI: Theory And Practice.* Elsevier.

Valdez, A. L., Delgado, O. D., and Fariña, J. I. (2021). Cost-effective optimized scleroglu-can production by Sclerotium rolfsii ATCC 201126 at bioreactor scale. A quantity-quality assessment. *Carbohydrate Polymers*, 260.

Verma, R., Mehan, L., Kumar, R., Kumar, A., and Srivastava, A. (2019). Computational fluid dynamic analysis of hydrodynamic shear stress generated by different impeller combinations in stirred bioreactor. *Biochemical Engineering Journal*, 151:107312.

Wan, X., Takahata, Y., and Takahashi, K. (2016). Power Consumption, Gas Holdup, and Mass-Transfer Coef fi cient of Triple-Impeller Con fi gurations in a Stirred Vessel with Vertical Tubular Coils. 94(FEBRUARY):349–354.

Xie, M., Xia, J., Zhou, Z., Chu, J., Zhuang, Y., and Zhang, S. (2014a). Flow pattern, mixing, gas hold-up and mass transfer coefficient of triple-impeller configurations in stirred tank bioreactors. *Industrial and Engineering Chemistry Research*, 53(14):5941–5953.

Xie, M., Xia, J., Zhou, Z., Chu, J., Zhuang, Y., and Zhang, S. (2014b). Flow pattern, mixing, gas hold-up and mass transfer coefficient of triple-impeller configurations in stirred tank bioreactors. *Industrial and Engineering Chemistry Research*, 53(14):5941–5953.

Xinhong, L., Yuyun, B., Zhipeng, L., Zhengming, G., and Smith, J. M. (2008). Particle image velocimetry study of turbulence characteristics in a vessel agitated by a dual rushton impeller. *Chinese Journal of Chemical Engineering*, 16(5):700–708.

Yang, F., Sun, H., and Zhang, C. (2020). Gas-liquid mixing in a grid-disc impeller stirred tank. *Chemical Engineering & Technology*, 43(7):1297–1307.

Yi, M., Jia-zhen, P., Guo-rui, N., Jian, M., and Zheng-ming, G. (2006). Mixing in stirred tanks with multiple impellers. *J. East China University of Science and Tehcnology*, (3):357–360.

You, S. T., Raman, A. A. A., Shah, R. S. S. R. E., and Nor, M. I. M. (2014). Multiple-impeller stirred vessel studies. *Reviews in Chemical Engineering*, 30(3):323–336.

Zhu, Z., Qin, B., Li, S., Liu, Y., Li, X., Cui, P., Wang, Y., and Gao, J. (2021). Multi-dimensional analysis of turbulence models for immiscible liquid-liquid mixing in stirred tank based on numerical simulation. *Separation Science and Technology (Philadelphia)*, 56(2):411–424.